Cross-tropopause tracer transport in midlatitude convection

Gretchen L. Mullendore

A dissertation submitted in partial fulfillment
of the requirements for the degree of

Doctor of Philosophy

University of Washington

2003

Program Authorized to Offer Degree: Atmospheric Sciences

University of Washington

Graduate School

This is to certify that I have examined this copy of a doctoral dissertation by

Gretchen L. Mullendore

and have found that it is complete and satisfactory in all respects,
and that any and all revisions required by the final
examining committee have been made.

Co-Chairs of Supervisory Committee:

_____

James R. Holton

_____

Dale R. Durran

Reading Committee:

_____

Dale R. Durran

_____

James R. Holton

_____

Joan Alexander

Date: _____

In presenting this dissertation in partial fulfillment of the requirements for the Doctoral degree at the University of Washington, I agree that the Library shall make its copies freely available for inspection. I further agree that extensive copying of this dissertation is allowable only for scholarly purposes, consistent with "fair use" as prescribed in the U.S. Copyright Law. Requests for copying or reproduction of this dissertation may be referred to Bell and Howell Information and Learning, 300 North Zeeb Road, Ann Arbor, MI 48106-1346, to whom the author has granted "the right to reproduce and sell (a) copies of the manuscript in microform and/or (b) printed copies of the manuscript made from microform."

Signature_____

Date_____

University of Washington

Abstract

Cross-tropopause tracer transport in midlatitude convection

by Gretchen L. Mullendore

Co-Chairs of Supervisory Committee:

Professor James R. Holton
Department of Atmospheric Sciences

Professor Dale R. Durran
Department of Atmospheric Sciences

Simulations performed by a 3D cloud-resolving model are used to study the transport of tropospheric tracers into the lowermost stratosphere via midlatitude convection. Direct transport by convection is believed to be the most likely mechanism by which short-lived chemical species can be transported from the boundary layer to the stratosphere. In the few works that have included analysis of cross-tropopause transport due to deep midlatitude convection, the tropopause is defined by a single altitude or pressure level, but the tropopause location is unclear in the highly perturbed environment directly above an active storm. thus, to determine the irreversibility of cross-tropopause transport, ten-hour simulations are carried out to cover the growth and decay cycles of the storm. After the decay of convection, isentropes relax to quasi-flat surfaces, allowing more confident tropopause location. At 1 km above the tropopause, the concentration of the tracer originating in the layer between 1 and 4 km has a maximum of 23% of its original concentration; the concentration of the tracer originating below 1 km has maximum of 26% of its original concentration. Increasing the altitude of the level of neutral buoyancy in model soundings and adding upper level wind shear are both found to produce more transport into the stratosphere. Supercell storms produce more transport when compared with multicell storms.

TABLE OF CONTENTS

LIST OF FIGURES

LIST OF TABLES

ACKNOWLEDGMENTS

I would like to thank Jim Holton and Dale Durran for their support and friendship. It has been an honor to work with two such amazing scientists and wonderful advisors. I have gained not only scientific knowledge, but also guidance in how to become a great scientist. I also extend my thanks to Joan Alexander who was a welcome friendly face while she was working at the University of Washington and an encouraging word from afar after she left. Thanks to Lyatt Jaegle for valuable insight into the world of chemistry.

Financial support for this research was provided by the National Science Foundation, grant ATM-0225441.

A big thank you to all of my peers and colleagues who have been willing to chat with me on subjects ranging from transport of gases to the initiation of lightning to annular modes. Finally, thank you to my family and to Greg. I could not have made it without you.

Chapter 1

INTRODUCTION

The chemical budgets of the upper troposphere and lower stratosphere are strongly influenced by transport of various constituents between the troposphere and stratosphere. Small injections of water vapor can have large radiative and chemical effects in the stratosphere. Many anthropogenic emissions, released into the planetary boundary layer, have little climatic impact until transported into the upper troposphere and stratosphere where the effects can be extensive (e.g. ozone depletion). Deep convection rapidly transports surface emissions and water vapor to the upper troposphere and possibly the stratosphere, playing an important, but poorly understood, role in tracer transport.

1.1 Known mechanisms of stratospheric-tropospheric exchange

In midlatitudes, air can be transported from the troposphere to the stratosphere by a number of pathways. Tropospheric air can cross the tropopause adiabatically via transport along isentropes, or diabatically, via convection and mixing.

Large scale stratospheric-tropospheric exchange is fairly well understood. Above approximately the 380 K isentrope, the average potential temperature of the tropical tropopause, the Brewer-Dobson circulation dominates (Holton et al., 1995). Tropospheric air enters this part of the stratosphere, also known as the overworld, in the tropics. The mechanism by which tropical air is lifted into the overworld is still under investigation, but it is generally accepted that mesoscale processes, especially convection, are important components of upward transport of lower-tropospheric chemical tracers into the tropical tropopause layer (12 to 16 km) just beneath the 380 K surface. From there they are transported into the overworld via the Brewer-Dobson circulation. Once in the stratosphere, air moves upward

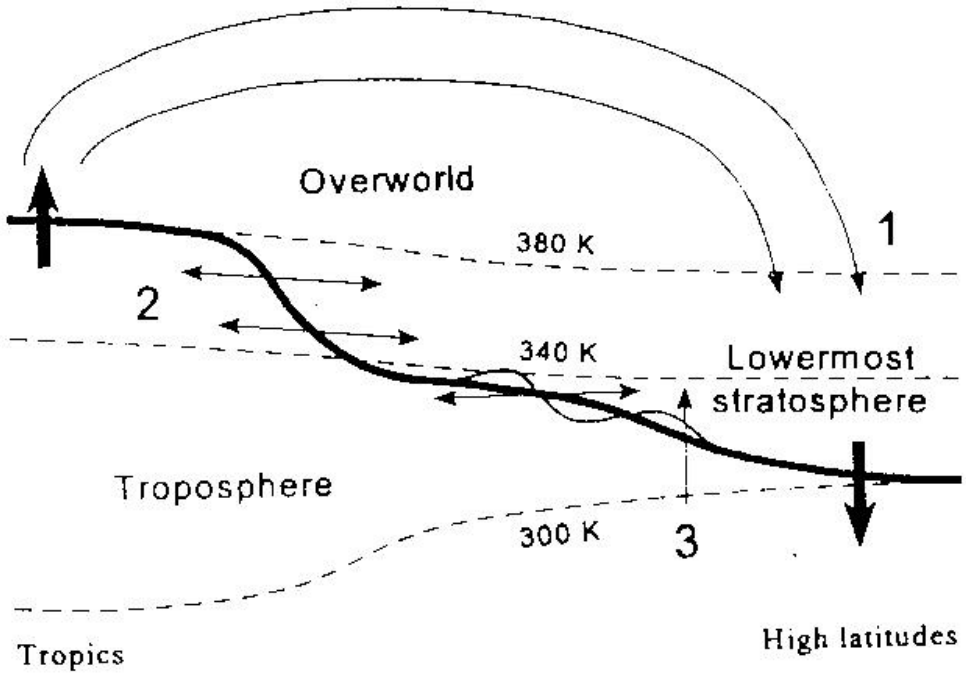

Figure 1.1: Schematic of the atmosphere, with the thick line denoting the average tropopause. Thick arrows show stratospheric-tropospheric exchange through the Brewer-Dobson circulation, and the labeled arrows show pathways by which air may enter the lowermost stratosphere. See text for pathway descriptions. (from Hintsa et al. (1998))

and poleward, before descending back into the troposphere in the extratropics.

In the extratropics, the dynamical tropopause is at lower altitudes, and is usually defined as a constant surface of potential vorticity (PV). The layer of the stratosphere below the overworld and above the extratropical tropopause is called the lowermost stratosphere. Air can reach the lowermost stratosphere by three alternative paths (Figure 1.1): (1) Diabatic descent from the overworld, (2) isentropic transport from the lower latitude troposphere, and (3) upward diabatic transport from the midlatitude troposphere. Hintsa et al. (1998) studied lower-stratospheric air and used ratios of observed gases (H_2O, CO_2, N_2O, O_3) to determine the air origin. Tropospheric air mixed directly into the lowermost stratosphere was found to be ubiquitous in the study. Strong convection was not observed in the air parcel back trajectories, so the authors concluded that path 2 dominated.

1.1.1 Synoptic scale transport

Many authors have demonstrated the importance of tropopause folding events in transport from the stratosphere to the troposphere (see review by Holton et al., 1995, and references therein). Tropopause folds occur near the jet stream when a layer of air moves downward and equatorward as a result of planetary wave-breaking. The episodic transfer of ozone from the stratosphere in folds strongly influences the chemical budgets and the radiative balance of the upper troposphere. However, even the contribution of tropopause folding to the tropospheric ozone budget remains highly uncertain since the amount of stratospheric air irreversably transported into the troposphere following a folding event is unclear and very little is known about the processes that lead to irreversible mixing. It is thought that tropopause folds undergo mixing due to small-scale turbulent processes, shear-induced instability, and gravity wave breaking, all of which are difficult to estimate.

Tropopause folding events also mix some tropospheric air into the stratosphere in the accompanying tropospheric ridges, but, generally, studies have concentrated on net mass flux across the tropopause which obscures the information relevant for diagnosing the two-way tracer transport, which depends on the positive and negative flux components. Upward (troposphere to stratosphere) terms are often neglected due to their small magnitudes relative to downward fluxes and the difficultly in extracting these small magnitudes from observational data. Also, upward transport occurring in folding events transports air that is upper-tropospheric; boundary layer air has more significant concentrations of many important tracers, e.g. CO and water vapor.

Water vapor measurements in midlatitudes also reveal troposphere to stratosphere exchange (Ovarlez et al., 1999). While the primary mechanism seems to be isentropic exchange, many authors have acknowledged that convective transport can not be ruled out. Convection can potentially move boundary layer air rapidly into the stratosphere.

1.1.2 Transport through deep convection

Deep convection is a particularly effective method for mixing boundary layer air into the upper troposphere. Convection can transport air from the boundary layer to the strato-

sphere on the order of an hour, while synoptic features such as extratropical cyclones would require days to accomplish the same mixing (Sigmond et al., 2000) and diffusive processes would require months (Dickerson, 1987).

In contrast to the synoptic scale mechanisms of cross-tropospheric exchange, the role of deep convection remains unclear. It is conceivable that evidence for transport from the troposphere to lowermost stratosphere due to convection does not appear in the many cross-troposphere transport studies because it would be a very localized event (in both time and space).

Convection is an especially important source of transport because it vents the boundary layer. Boundary layer venting increases both the lifetime and spatial reach of chemical tracers. Because of low wind velocities, boundary layer emissions tend to stay concentrated near the source region. But once vented, a local problem can become regional. If the tropopause is penetrated, the problem can become global (Dickerson, 1987).

1.2 Previous studies

Several experiments and simulations have demonstrated that thunderstorms may control the redistribution of trace gases in the troposphere (e.g. Wang and Chang (1993), Hauf et al. (1995)), but very few have specifically dealt with the issue of cross-tropopause exchange. In the few works that have included analysis of cross-tropopause transport due to deep convection (e.g. Stenchikov et al. (1996), Skamarock et al. (2000)), the tropopause is defined by a single altitude or pressure level, which is unsatisfactory for a storm-perturbed tropopause.

1.2.1 Observational

Hauf et al. (1995) observed undiluted air in the anvil outflow from a midlatitude convective storm, 120 km from the main updraft. The topic of tropospheric to stratospheric exchange was not specifically addressed in this study, but the observation of a protected core, or undiluted boundary layer air, in the outflow sparked interest because the potential for boundary air to reach the tropopause without dilution might enhance potential for significant mixing

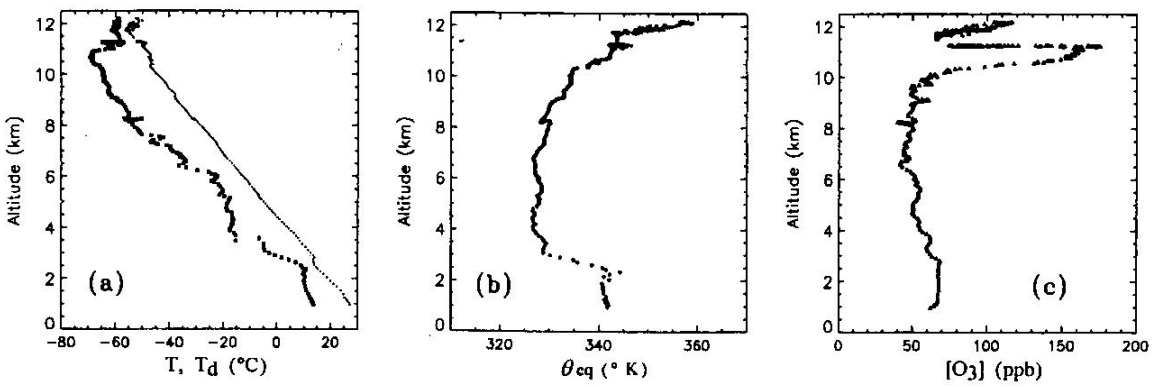

Figure 1.2: Vertical profiles of (a) temperature and dewpoint temperature, (b) equivalent potential temperature, and (c) ozone concentration retrieved from the measurements taken during the ascent of the research flight. (from Poulida et al. (1996))

between boundary layer and stratospheric air.

Poulida et al. (1996) reported findings from measurements taken of a June 1989 squall line and mesoscale convective complex (MCC) over North Dakota. This paper challenged the existing view that the only part of the thunderstorm to enter the stratosphere is the overshooting top with the anvil forming well under the tropopause. Using temperature lapse rate, ozone concentrations and potential vorticity values, the authors estimated a prestorm tropopause level of 10.6 km to 11 km. The storm had a level of neutral buoyancy of 11.5 km with observed updraft velocities of 30 m/s. Aircraft flights through this storm encountered low ozone/high carbon monoxide air above air that had ozone concentrations indicative of stratospheric air (figure 1.2, panel c), suggesting that tropospheric air had been injected into the stratosphere. While there is little doubt that this air is indeed of tropospheric origin, the eventual fate of the tropospheric lens is uncertain, a fact acknowledged by the authors. Figure 1.2 also shows the equivalent potential temperature (panel b), which is less stable in the area of the tropopause lens. The flight measurements were taken within 2.5 hours of the first signs of convection seen by satellite while convection was still active, and thus with insufficient time for the storm-perturbed tropopause to relax. The findings of Poulida

et al. (1996) also suggest there is water vapor injection at midlatitudes, but the extent is unclear due to the very localized nature of the observations.

Strom et al. (1999) reported in situ measurements performed in two cumulonimbus anvils over western Europe during the Stratosphere-Troposphere Experiment by Aircraft Measurements (STREAM) in July 1994. Taking measurements such as ozone and carbon monoxide, this study observed that much of the air in the anvil was rapidly transported from the boundary layer and experienced little dilution. This study used potential vorticity surfaces, calculated from ECMWF meteorological fields, to define the tropopause region and concluded that some boundary layer air was transported into the lowermost stratosphere.

Fischer et al. (2003) obtained aircraft observations of boundary layer air injected into, and above, the tropopause region in southern Europe. They attributed the observed injected air to deep convection. The air is diagnosed as stratospheric both because of the high PV values and high ozone concentrations ($[O_3] > 200$ ppbv). Using various boundary layer tracers, they determined that the injected air consisted of between 28-51% boundary layer air. They also conducted 10-day forward trajectory studies of this air mass and, based on PV values, concluded the air would re-enter the troposphere but then return to, and remain in, the stratosphere. It should be noted that this was a tropopause-fold event.

There is some evidence that midlatitude convection adds to the downward transport of ozone from the stratosphere (Poulida et al., 1996). The amount of downward mixing when compared with tropopause folding events, however, is small. On the other hand, since convection transports air from near-surface to high altitudes, convection may be the most significant source of transport of low-level tracers into the stratosphere. If even a small fraction of the mass of the cloud anvil remains in the stratosphere, then convective transport is an important transport mechanism.

1.2.2 Numerical

Studying the transport of tracers in convection is difficult because so many parameters affect storm evolution, including physical parameterizations, numerical schemes and related computational parameters, and initial and boundary conditions (Park and Droegemeier,

2000).

Wang and Chang (1993) used a three-dimensional model to simulate the evolution of chemical species during the life cycle of a severe storm. Due to computational constraints, this study had a small domain and was only run to 1.5 hours. Cross-tropopause exchange was not addressed.

Stenchikov et al. (1996) used a two-dimensional model to simulate a deep midlatitude convective event. This storm was observed to have an anvil well above the pre-storm tropopause level and the companion observational paper (Poulida et al., 1996) claimed that there was significant mass exchange across the tropopause. Indeed, the simulated storm injected boundary layer tracers above the pre-storm tropopause level and brought ozone down from the stratosphere.

The authors extrapolated the findings from the single storm and estimated the cross-tropopause exchange due to all mesoscale convective systems. They concluded that the downward transport of ozone was small in comparison with the global flux, but that the upward flux of water vapor and other boundary layer tracers could be locally significant. However, because the tropopause itself was pushed upwards by the strong updrafts, permanent mixing into the lower stratosphere was unclear. This study also had relatively low resolution in the upper troposphere/ lower stratosphere. The authors acknowledged that "long-term net transport remains highly uncertain."

Wang and Prinn (1998) used a two-dimensional model to investigate the role of wind shear in tropical convective mass transport. The authors found that the strength of the vertical wind shear in the vicinity of the tropopause plays a significant role in controlling the developent of deep convective clouds, and hence on the deep transport of boundary layer tracers. Moderate shear was most favorable for transport in the stratosphere. Strong shear enhanced the turbulent mixing, but limited the depth of the convective turrets, resulting in less transport to the stratosphere. This model used a single altitude tropopause definition.

Skamarock et al. (2000) simulated a midlatitude storm in a 3D model. The authors found transport across the tropopause, but again this was only a single altitude layer. Their study was mostly concerned with transport to the upper-troposphere.

Wang (2003) simulated a deep supercell storm observed during the Cooperative Con-

vective Precipitation Experiment (CCOPE) in Montana during August, 1981. The study showed a water vapor plume above the main cloud anvil and attributed the plume to gravity wave breaking at cloud top which caused mixing of water vapor from the overshooting dome with stratospheric air. Wang (2003) used a Θ_e surface to define the tropopause location because the surface roughly coincided with the cloud top. The simulation was only carried out to 150 minutes, making the long-term water vapor plume evolution uncertain, as acknowledged by the author.

1.3 Motivation

It has remained unclear whether significant irreversible troposphere-to-stratosphere exchange (TSE) actually occurs in midlatitudes. Even if TSE is occurring it is doubtful that lower-stratospheric air, under the influence of the Brewer-Dobson downward circulation, would mix into the overworld. The thermodynamic stability of the stratosphere strongly inhibits the mixing of the transported trace gases into the middle stratosphere. It is unlikely that the effect of midlatitude TSE would be global.

But the possibility of midlatitude TSE still deserves careful analysis. Even small amounts of near surface air penetrating into the lower stratosphere can have important effects on the local stratospheric chemistry, possibly affecting the entire latitude band. Water vapor injection by convection could be an even more important effect.

This study is the first to use three-dimensional modeling to study not only the amount injected above a dynamic tropopause, as opposed to a flat surface, but also the long term evolution of the injected air parcels.

Note that tropical TSE by convective systems is perhaps a more important area of research as tracer injection is much larger and tracers are transported into the overworld, where global effects are undeniable. Midlatitude TSE by convection seemed a more logical starting place, however. Midlatitude storms have higher convective available potential energy (CAPE) than tropical storms. Storms with higher CAPE are easier to simulate accurately with idealized cloud resolving models because a single thermal initiated by a warm bubble can well simulate the storm trigger. Lower CAPE storms, such as is common in the

tropics, need mesoscale features such as convergence lines to drive the convection. Also, the relevant tropopause height in the tropics is even harder to define than in the extratropics.

1.4 Overview

In this study, we will characterize TSE of passive tracers due to isolated midlatitude convection. We varied storm parameters in a number of ways in order to study which environmental factors most affect the tracer transport. It is already known that vertical variations in the thermodynamic quantities and lower tropospheric horizontal wind affect the scale of updrafts and downdrafts, as well as the growth speeds of convective cells (e.g. Weisman and Klemp (1982)) and therefore affect the vertical fluxes of chemical species. We therefore concentrated on variables that affect transport but have minimal effect of the gross storm characteristics.

In chapter 2 we introduce the model used and discuss some of the model initialization issues. We also detail the technique used to calculate back trajectories.

In chapter 3, we present the results from five model runs. An idealized supercell storm is used to describe the main features of tracer transport throughout the depth of the model. To investigate the effects of variation of storm parameters, we compare the supercell storm with an idealized multicell storm (variation of storm classification) and with an idealized supercell storm with a high tropopause (variation of the distance between level of neutral buoyancy and tropopause). We then introduce a model run based on a remarkably deep convective event observed in the 2000 Severe Thunderstorm Electrification and Precipitation Study (STEPS) campaign. Lastly, we compare the high tropopause supercell case, which had no upper level shear, with a high tropopause storm that was initialized with the shear from the STEPS storm (variation of upper level shear).

In chapter 4, we summarize the results of the model cases. The results are also discussed in the context of two boundary layer tracers, carbon monoxide and radon. Some discussion of convective transport parameterizations for large-scale models is included.

Chapter 2

MODEL DEVELOPMENT AND ANALYSIS TOOLS

2.1 Numerical Model

The model used is a three-dimensional, cloud-resolving mesoscale model based on that of Piani et al. (2000). The version used here includes passive tracer advection and incorporates grid nesting. Previous model versions used a leapfrog scheme for scalar advection; a satisfactory scheme for advection of smooth variables, but a scheme which tends to cause serious overshoots and undershoots in the vicinity of strong gradients. The addition of a flux-limited advection scheme (LeVeque, 1996) for scalar advection was a crucial improvement allowing for the more realistic advection of sharp gradients in the tracer fields. The grid nesting and simulation resolution is discussed further in section 3.3.1.

2.1.1 Basic Equations

The basic model equations (below) remain unchanged from those described in Durran and Klemp (1983).

$$\frac{du}{dt} + c_p\Theta_M\frac{\partial\pi}{\partial x} = D_u$$

$$\frac{dv}{dt} + c_p\Theta_M\frac{\partial\pi}{\partial y} = D_v$$

$$\frac{dw}{dt} + c_p\Theta_M\frac{\partial\pi}{\partial z} = g\frac{\Theta_M - \overline{\Theta_M}}{\overline{\Theta_M}} + D_w$$

$$\frac{d\pi}{dt} + w\overline{\Pi_z} = -\frac{R}{c_v}(\overline{\Pi} + \pi)(\frac{\partial u}{\partial x} + \frac{\partial v}{\partial y} + \frac{\partial w}{\partial z}) + \frac{R}{c_v}\frac{(\overline{\Pi} + \pi)}{\Theta_v}\frac{d\Theta_v}{dt}$$

$$\frac{d\Theta}{dt} = M_\Theta + D_\Theta$$

$$\frac{d\chi}{dt} = D_\chi$$

where:

$$\frac{d}{dt} = u\frac{\partial}{\partial x} + v\frac{\partial}{\partial y} + w\frac{\partial}{\partial z}$$

$$(\overline{\Pi} + \pi) = (\frac{p}{p_0})^{\frac{R}{c_p}}$$

$$\Theta_v = \Theta(1 + 0.61 q_v),\ \Theta_M = \Theta_v(1 - q_L - q_I)$$

In the above equations, u, v, and w are the westerly, southerly and vertical components of the wind, respectively, p is the pressure, Θ is total potential temperature, χ is the mass mixing ratio for a passive tracer, q_v is the mass mixing ratio for water vapor, q_L is the mass mixing ratio for the liquid water, q_I is the mass mixing ratio for the frozen water, $p_0 =$ 1000 hPa, and c_p is the specific heat of dry air at a constant pressure. Overbars denote the horizontally homogeneous reference states. Θ_v gives the virtual potential temperature, the temperature a dry parcel of air would have if its pressure and density were equal to that of a given sample of moist air without liquid condensate. Θ_M is the temperature a dry parcel of air would have if its pressure and density were equal to that of a given sample of cloudy air. D_α represents the joint effects of subgrid-scale mixing and computational smoothing on the variable α. M_α represents the effects of cloud microphysics on the variable α. Note that the prognostic equation for the water categories is identical to the prognostic θ equation.

2.1.2 Ice microphysics

The cloud microphysics parameterization is based on the work by Tao and Simpson (1993). The parameterization scheme uses six water categories: water vapor(q_v), cloud water(q_c), rain(q_r), cloud ice(q_i), snow(q_s) and hail(q_h). The liquid and ice particles are assumed to be spherical. Rain, snow and hail have exponential size distributions given by

$$N(D) = N_0 \exp(-\lambda D)$$

where D is the drop diameter, $N(D)$ is the number of drops per unit volume with diameters between D and $D + \delta D$ in a unit volume of air, N_0 is the intercept parameter ($N(D = 0)$), and λ is the slope of the particle size distribution. λ is given by

$$\lambda = (\pi \rho_\alpha N_0 / \rho q_\alpha)^{0.25}$$

where ρ_α is the density of the hydrometeor, and q_α is the mixing ratio of the hydrometeor. Values for N_0 and ρ_α, respectively are 0.08 cm^{-4} and 1.0 g/cm^3 for rain, 1.0 cm^{-4} and 0.1 g/cm^3 for snow and 0.0004 cm^{-4} and 0.9 g/cm^3 for hail; these values are typical for midlatitude storms (Tao and Simpson, 1993). Cloud ice has a single diameter of 0.002 cm and a density of 0.9 g/cm^3. Cloud ice and cloud water have zero fall speed. For more details on the equations used by the microphysical parameterization, see Appendix A.

2.1.3 Dry air influx

A major obstacle to running the model out to longer time periods was the continual generation of new convective cells. This occurs as the storm outflow, the cold pool, advances into the unperturbed model domain. Because the model variables are homogeneous in the horizontal at time of initialization and the model boundaries have a zero gradient condition, the unperturbed regions contain the same convective available potential energy to promote new cell growth as the first cell that formed. Eventually, these new cells reach the domain boundaries, setting off numerical instabilities.

In order to avoid this predicament, we added an area of dry air in the initial domain that is advected toward the storm (see Figure 2.1). Drying the boundary layer reduces the available potential energy thus suppressing the growth of new cells. The boundary between the two air masses is a straight-line transistion zone, approximately 30 km wide, in which the water vapor mixing ratio decreases linearly through the depth of the dry zone. The dry zone has a finite depth (1.9 km for idealized cases, 5 km for STEPS case) and everywhere within that depth, the water vapor mixing ratio is decreased uniformly by a set percentage (50% for the idealized cases, 75% for the STEPS case). The convective center reaches the dry air mass approximately 1.5 hours after model initialization.

Figure 2.2 compares the total mass transported into the stratosphere in a supercell storm that encounters the dry air mass with a supercell storm where no dry air mass exists. The mass transport is calculated by summing the mass in the stratosphere of the outer domain. The comparison can only be run out to 2 hours because the storm without the dry air mass becomes numerically unstable when convection reaches the boundary of the inner domain,

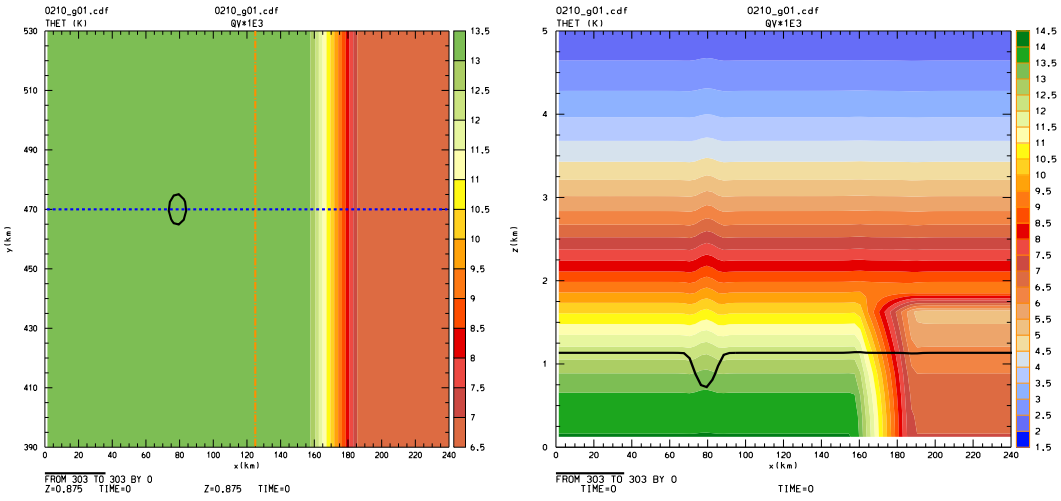

Figure 2.1: Water vapor mixing ratio (colored contours) from the idealized supercell case after the warm bubble has been initialized and the location of the 303 K isentropic surface (solid black line). The depression in the theta surface shows the location of the initial updraft. The blue dashed line shows the location of the cross-section. The orange dash-dot line shows the location of the leading edge of the dry air influx one hour later. Because the model domain moves at the speed of the storm, the storm appears stationary and the dry air influx appears to move westward.

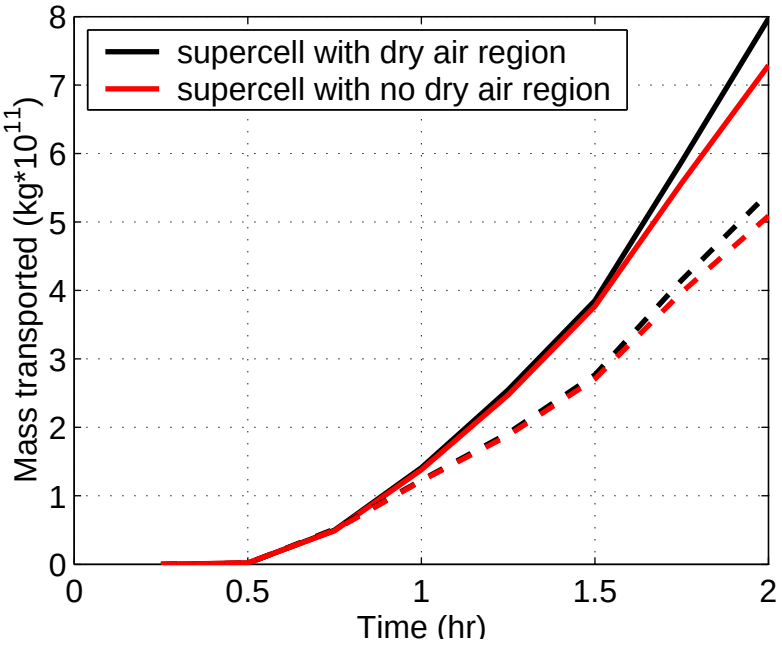

Figure 2.2: Total amount of tracer transported into the stratosphere. Black lines show total transport for a supercell storm that encounters a dry air mass at 1.5 hours; red lines show total transport for a supercell storm where no dry air mass exists. The solid lines show transport of the boundary layer tracer (surface to 1.375 km); the dashed lines show transport for an elevated layer tracer (1.375 km to 4.375 km).

which occurs at approximately 2 hours. The dry air mass is reached at approximately 1.5 hours. At 2 hours, the increase in mass transport due to the dry air mass boundary is 9% for the boundary layer tracer (solid lines) and 6% for the elevated tracer (dashed lines). Contamination of transport totals due to circulations caused by the vertical temperature (Θ_v) gradient at the dry air boundary might be avoided in future model versions by enforcing a zero Θ_v gradient at the boundary (i.e. by specifying a warmer dry air mass).

2.1.4 Geostrophy

These runs are done using an f-plane approximation (f=8.75e-5 s^{-1}), but the initial state is not in thermal wind balance; temperature is horizontally uniform while velocity has vertical shear. Enforcing geostrophic balance in the lowest model layers would have required a time evolving background flow with a very complicated temperature field and obscured our understanding of the effects of CAPE on the storm development and transport while not necessarily adding any "truth" to the initial conditions. Also, the length of our model runs (10 hours) is much shorter than the geostrophic adjustment time-scale (+25 hours in a test simulation).

Since the objectives of this study depend strongly on the knowledge of the tropopause location, we wanted to make sure that the absence of geostrophic balance at initialization would not strongly affect our results. Specifically we wanted to check that a slanted tropopause, which would occur for an environment in thermal wind balance, would not have a significant effect on the location of the tropopause. As the tropopause is defined as a gradient in Θ in this study, changes in heat transport could affect the tropopause location.

To investigate the additional heat transport that would result from thermal wind balance, we first calculated the slope of the isentropes aloft for both the idealized supercell case and the STEPS case. The models were initialized with geostrophy enforced but without a warm bubble to initiate convection, and the slope of the isentropes was recorded at tropopause level. We then analyzed the horizontal heat transport at two hours in a simulation that included convection but not thermal wind balance. We calculated the additional horizontal heat transport that would be contributed by a tilted tropopause by multiply-

ing the tropopause level horizontal winds by the Θ gradients recorded from the geostrophy initialization. For the supercell storm, additional horizontal heat transport due to a tilted tropopause was 5 orders of magnitude smaller than the heat transport in the flat tropopause case. The same magntitude difference was found for the STEPS storm. A tilted tropopause would cause problems with tracer initialization while contributing little to the storm heat transport or tropopause location.

2.1.5 Initial bubble

Convection in all cases is initiated by a warm bubble. For all cases, the initial bubble has a horizontal radius of 10 km and a vertical radius of 1.4 km. The bubble was centered 1.4 km above the ground. The bubble perturbation temperatures for the idealized cases and the STEPS storm are 2 K and 4 K, respectively. The temperature profile of the bubble was sinusoidal with its maximum at the center. In order to avoid the shock wave that would be created by an instantaneous temperature increase, the bubble temperature is increased, from zero to its maximum temperature in increments of $-0.5A*d(\cos(\pi t)/T_{ramp})/dt$, where A is the maximum temperature and T_{ramp} is the total ramp-up time, over the first 5 minutes of model time.

Even with the relatively gradual introduction of the bubble, we were still concerned that the unrealistic initial updraft would contaminate the total transport results. Figure 2.3 shows the total boundary layer tracer transported into the stratosphere in both the supercell and multicell regimes (see Results chapter for details). The bubble has reached full strength by time 0 on this graph. The signature of the initial bubble is gone by 0.8 hours when the slope of the supercell total transport line exceeds the slope of the multicell total transport line. Initially, the supercell transports less material because the updraft is more eroded in the higher shear environment. But, by 0.8 hours, the difference in character of updrafts in the different regimes is evident, and the supercell transports more material because the updraft is stronger and less eroded. We argue that a conservative estimate for storm spin up time is one hour. In this first hour, less than 20% of the total mass transport into the stratosphere occurs and, in most cases, the amount is smaller: multicell

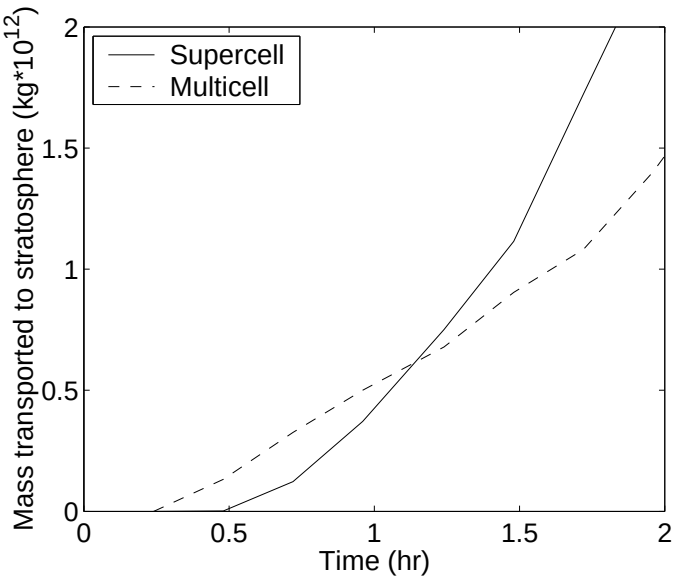

Figure 2.3: Total amount of boundary layer tracer transported into the stratosphere in the supercell (solid line) and multicell (dash line) regimes. The tropopause is defined by its pre-storm $d\Theta/dz$ value.

19%, supercell 6%, STEPS 11%. It should also be noted that the bubble size is comparable across all cases, hence the absolute magnitude transported in the initial bubble is comparable across all cases, making the comparisons of total transport between models robust.

2.1.6 Sensitivity tests

Mixing strength

Turbulent mixing is parameterized by a first order closure formulation which depends on the ratio of the magnitudes of stratification to shear (Durran and Klemp, 1983). The subgrid scale mixing terms are proportional to both the shear deformation and mixing coefficient and "turn on" for Richardson number less than one for these model runs. Here the Richardson number is defined as Ri = N/β, where N is the buoyancy frequency and β represents the shear deformation. The mixing coefficient, K_m, is proportional to the grid spacing of the

resolution of the most resolved grid, the shear deformation, and the Richardson number.

$$K_m = (0.21)^2 \Delta x \Delta z \beta^{1/2} \max\left(1 - \mathrm{Ri}, 0\right)^{1/2} \tag{2.1}$$

For more details on the equations used to calculate the subgrid-scale mixing, see Appendix B.

To assess the sensitivity of the cross-tropopause mixing to the mixing parameterization, we decreased the mixing coefficient by 1/4 for one test case; i.e. K_m was made proportional to $(\Delta z)^2$ instead of $\Delta z \Delta x$. Note that the mixing coefficient for the control case makes the largest turbulent eddies proportional to the size of the grid box in the finest grid, $\Delta z \Delta x$, where Δz = 250m and Δx = 1000m. For simulations where the grid resolution is more anisotropic, using the small grid spacing, usually vertical, is more appropriate. After three hours into the storm, the finest grid is no longer run and the runs have a resolution of Δz = 250m and Δx = 3000m. It could be argued that a $(\Delta z)^2$ would be a better turbulence bound after three hours.

For numerical stability the mixing coefficient has an upper bound

$$K_m = \frac{\Delta z^2}{8 \Delta t}$$

which equals 2604 m^2/s (Δt = 3, Δz = 250) for the highest resolution grids in the test case and 10416 m^2/s in the regular model runs.

Figure 2.4 shows a comparison of various model parameters in the two different mixing regimes. The solid line shows model results for the test case where the mixing coefficient was reduced by 1/4 by using $(\Delta z)^2$ instead of $\Delta x \Delta z$ in equation 2.1; the dashed line shows the control run. The maximum vertical velocity is similar for both cases (top panel) although the amount of mixing is stronger in the control case (middle panel). The bottom panel shows the total boundary layer tracer mass transported into the stratosphere. The case with reduced K_m had consistently more transport. At four hours, the amount of boundary layer material transported to the stratosphere in the case with reduced K_m was 11% higher than in the control case. Although, a higher mixing coefficient (control case) increases the mixing at cloud top which increases the amount of material transport across the tropopause, stronger mixing in the updraft dilutes both the tracer concentrations and updraft strength,

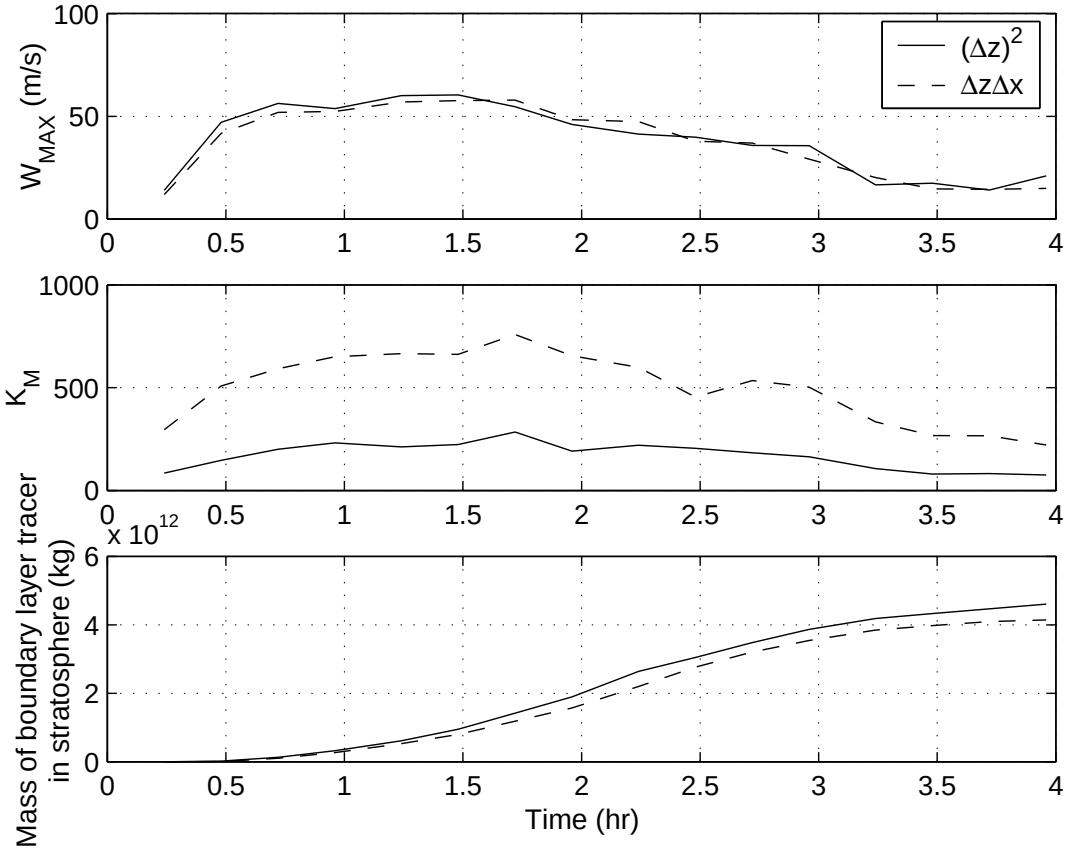

Figure 2.4: Comparison of maximum vertical velocity (top panel), maximum mixing coefficient (middle panel), and total boundary layer mass transported to stratosphere (bottom panel) for two different mixing regimes. The solid line shows results for a model run where the mixing coefficient was proportional to $(\Delta z)^2$; the dashed line, proportional to $\Delta z \Delta x$.

thereby reducing the total transport of lower tropospheric tracers to the tropopause level. The results of the control case are presented in this work and respresent a lower bound, with respect to mixing coefficients, for transport into the stratosphere. We also found that mixing was negligible after three hours of simulation time, making the issue of reduced grid resolution after three hours a moot point.

2.1.7 Model Validation

Although this model has been validated previously, we wanted to confirm that the newest modules (e.g. flux-limited advection, tracer transport, ice microphysics) produced reasonable results. The storm observed on July 10th, 1996 during the Stratospheric-Tropospheric Experiment: Radiation, Aerosols, and Ozone (STERAO) campaign and was simulated using the thermodynamic and chemical tracer profiles described in Skamarock et al. (2000) (henceforth SKA00). Good agreement was found between our model and the observations for reflectivity and tracer transport. Good agreement was also found between our model and the published results from the SKA00 model. It should be noted that the model used in SKA00 was based on the same original model (Durran and Klemp, 1983) as the model used in our study. Figure 2.5 shows the reflectivity in a horizontal cross-section through the storm at 4.5 km mean sea level (MSL) (3.0 km above ground level (AGL)) and 10.5 km MSL (9.0 km AGL). Both the reflectivity from the CHILL radar and the SKA00 model-derived reflectivity are shown. Figure 2.6 shows the model-derived reflectivity for our model. Model-derived reflectivity is calculated from the mixing ratios of rain, snow and hail following Braun and Jr (1994). The spatial area shown is identical in both figures.

At low levels, the maximum reflectivity and spatial patterns in our model compare well with both the observations and the SKA00 model. There is discrepancy with the observations in the number of convective centers, but this is in part due to the simulations being initialized with three convective centers at t=0 to simulate the convective line structure. The observed storm outflow is more southward than both simulations at later times (at both low and high levels), but neither model incorporates mesoscale wind shifts needed to capture this feature. In comparing the two models at low levels, our model contains more

convective elements at later times, but neither model has a clearly better solution when compared with observations.

At 9 km AGL, the models compare well with each other, but both have less spatial coverage than in the observations. Cloud-resolving models are known to underestimate the anvil extent (C. Schumacher, personal communication, 2003).

Figures 2.7 and 2.8 show vertical cross-sections of reflectivity for two different times in the SKA00 model, CHILL radar observations, and our model. The maximum reflectivity compares well in each figure, but the bright band structure in the later CHILL snapshot is not reproduced. The spatial structures in the model simulations compare very well with each other, but neither model captures the depth of the storm at early times. Comparing non-averaged cross-sections is difficult as it is unlikely that one would catch all features in isolated cross-sections at specific times.

Finally, we wanted to compare the tracer transport, in this case the transport of CO, in both models. The SKA00 model uses a modified Van Leer type scheme (see Wicker and Wilhelmson (1995)) for advection. Figure 2.9 shows the time-integrated flux divergence for CO at 1, 2, and 3 hours. This quantity was calculated as in SKA00 using the below equation.

$$\int_0^t \int_\Omega \frac{\partial}{\partial z}(\overline{\rho} w \chi) \partial\Omega \partial t$$

where χ is the tracer concentration, ρ is the density, and Ω is the horizontal area.

Both models show a net gain in CO above approximately 6.5 km. The models differ in that our model shows much stronger divergence and convergence values below 5 km AGL at 3 hours. These higher magnitudes are likely due to the fact that our model contained more cells at later times than the SKA00 model; the locations of the maximums are the same in each figure. More detailed analysis of tracer divergence patterns can be found in the results section.

2.2 Stabilization of soundings

The original soundings for both the idealized cases and the STEPS case were dynamically unstable at t=0 due to areas of vertical shear. In these unstable zones (below 5 km), the

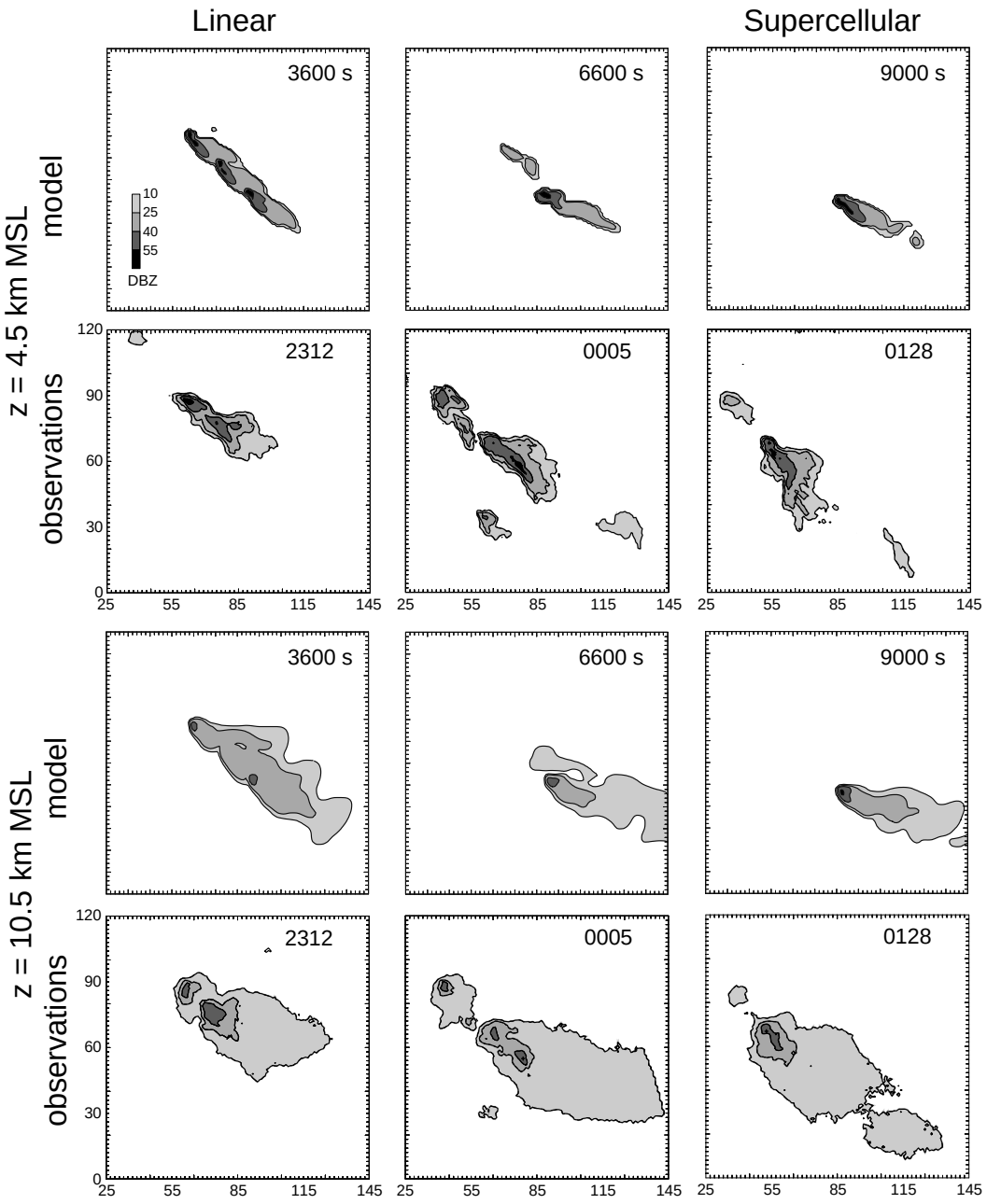

Figure 2.5: Horizontal cross sections of radar reflectivity from the CHILL radar and derived from the simulation by Skamarock et al. (2000). Numbers in upper left corner of the model plots are simulation time. Numbers in upper left corner of the observation plots are UTC measurement times. The horizontal and vertical axes are distance east and north from CHILL radar (kilometers), respectively. Figure 6 from Skamarock et al. (2000).

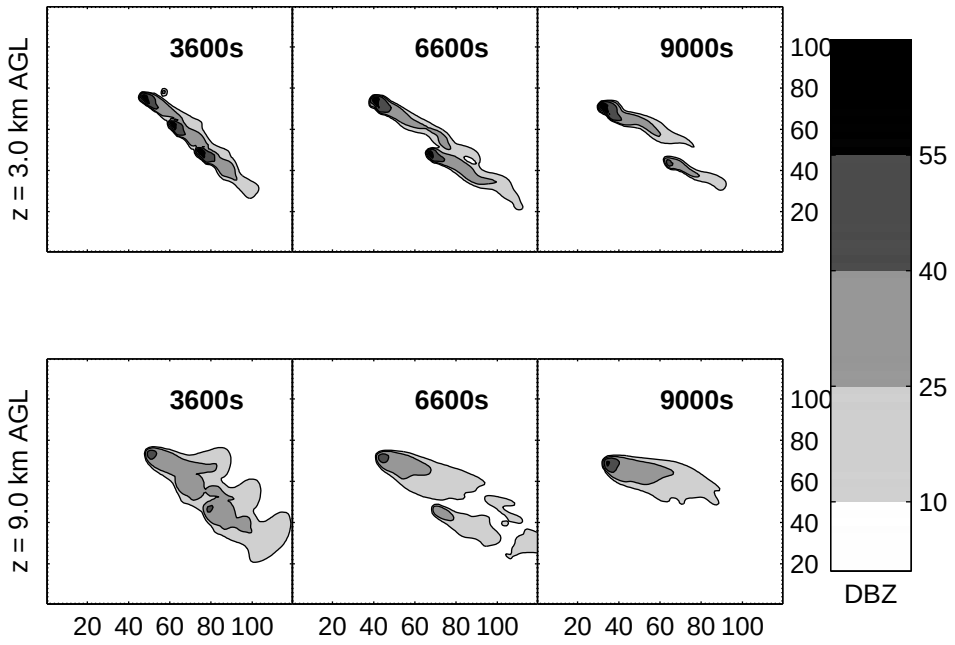

Figure 2.6: Same as for Figure 2.5, but radar reflectivity derived from the model used in this study.

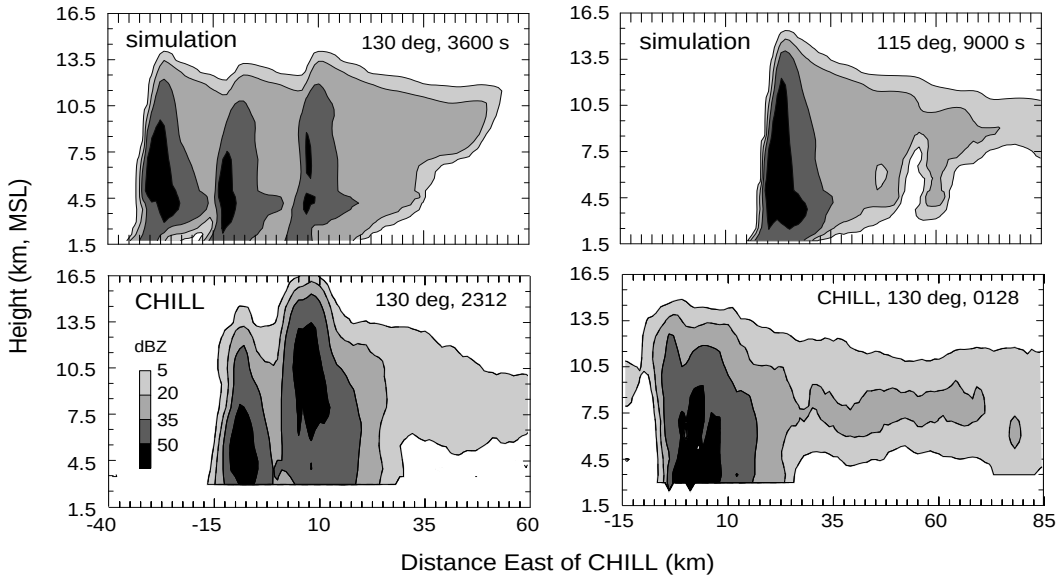

Figure 2.7: Vertical cross sections from CHILL and reflectivity dervied from the Skamarock et al. (2000) simulation. Figure 7 from Skamarock et al. (2000).

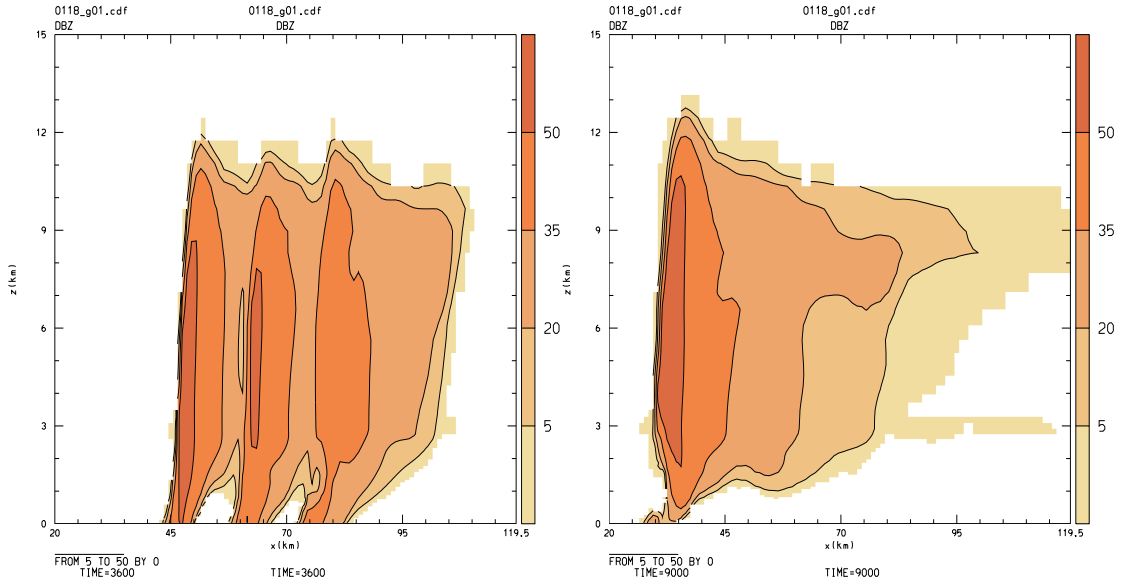

Figure 2.8: Same as for Figure 2.7, but radar reflectivity derived from the model used in this study.

Richardson number was low enough to trigger subgridscale mixing. Previous studies have successfully used these soundings unchanged because the mixing is small enough to change the storm development only slightly. In the case of tracer transport, however, the mixing layers diffuse the tracer source layers, which can affect the tracer concentrations transported to the stratosphere.

In order to avoid this problem, we allowed the initial soundings to mix up on their own in a model environment where convection was not initiated. Once the model has stabilized the environment through mixing, a new sounding is created from the model environment. This way we could remain in the same storm regime, since the model was mixing to this state on its own (as opposed to arbitrary manipulation of the shear profiles by hand.)

This stabilization process has minimal effect on the storm regime. After mixing, the supercell case has a CAPE of 2477 m^2/s^2 compared with a CAPE of 2367 m^2/s^2 before mixing. CAPE was calculated by averaging the thermodynamic values in the lowest two model levels and then lifting a parcel with those properties through the model environment.

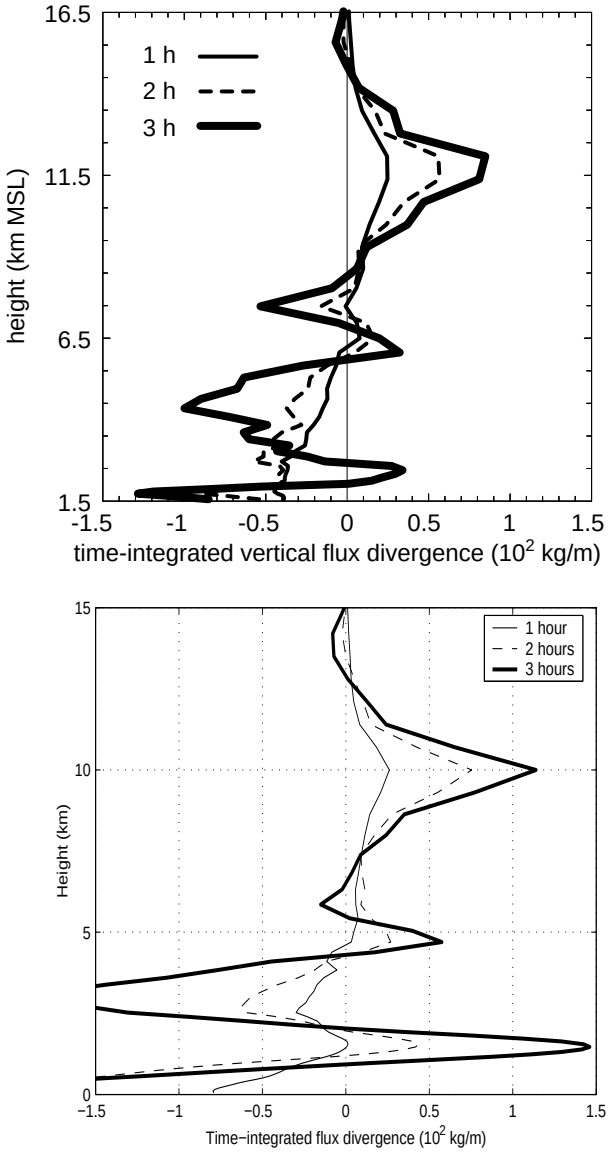

Figure 2.9: Time-integrated flux divergence for CO at 1, 2, and 3 hours. Figure 12 from Skamarock et al. (2000) (top panel). Same calculated from the model used in this study (bottom panel).

2.3 Trajectory analysis

In order to investigate histories of individual parcels of air, back trajectories were calculated using a 3rd order Runge-Kutta scheme (Durran, 1999). Sensitivity testing showed that a time step of 72s was sufficient to accurately follow the trajectories through the main updraft. At each trajectory location, velocities and scalars are calculated using cubic interpolation. It should be noted that the back trajectories are calculated using wind velocities only, subgrid-scale mixing is not accounted for.

Chapter 3

MODEL RESULTS

3.1 Tracer Initialization

The major goal of this work is to quantify the mass transport from the lower troposphere to the upper troposphere and lower stratosphere produced by extratropical convective storms. For this purpose it is convenient, following the work of Scala et al. (1990) and Lu et al. (2000), to define a set of five passive tracers initially confined to horizontally homogeneous layers. Wang and Chang (1993) included chemistry in their modeling study, but found that dynamical processes accounted for nearly 100% of in-cloud variation for insoluble gases that had chemical lifetimes longer than the storm timescale of hours (e.g. ozone), demonstrating that chemistry could be neglected for such gases.

These tracers are given an initial mixing ratio of unity in order to more easily interpret their transport in terms of mass transport. The model tracers are initially confined in layers from 0.125 to 1.375km, 1.375 to 4.375km, 4.375 to 7.375km, 7.375 km to tropopause, and tropopause to top of domain (figure 3.1). For ease of discussion we shall label the tracer layers as TR5(surface) to TR1(stratosphere). In each layer, the tracer concentration transitions from 0 kg/kg to 1 kg/kg over one vertical grid step, 250 m. Each tracer layer encompasses a minimum of 5 vertical grid steps.

3.2 Tropopause definition

The tropopause has variously been defined by changes in the temperature lapse rate, the buoyancy frequency ($N^2 \equiv g\frac{dln\Theta}{dz}$), the ozone profile, and/or the potential vorticity (PV). It is unclear which, if any, of these definitions is a satisfactory proxy for the tropopause level in a storm environment, where the anvil has pushed and deformed the air around the original tropopause level. Instead of guessing which definition would be best, these simulations were

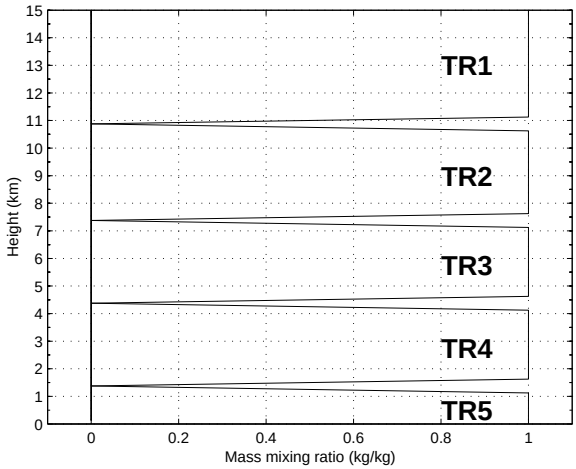

Figure 3.1: Profiles showing the mixing ratios for the passive tracers. TR5 serves as a proxy for a tracer with boundary layer source. TR1 serves as a proxy for a tracer with stratospheric source.

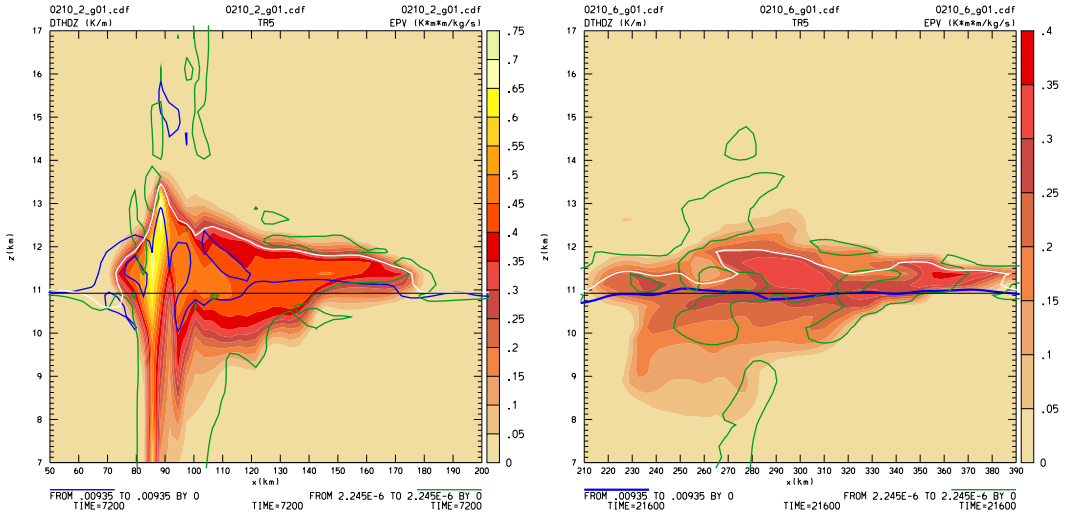

Figure 3.2: Boundary layer tracer plume at 2 hours (left panel) and 6 hours (right panel). The colored contours show the concentration of TR5, the boundary layer tracer. Contour interval is 0.05 kg/kg. The lines overlain on the colored contours show the tropopause according to various tropopause definitions. The black line shows the constant z surface, the blue line shows the constant $d\Theta/dz$ surface, the green line shows the constant PV surface, and the white line shows the constant ozone (TR1) surface.

run out long enough that the tracer plume reached a relatively unperturbed tropopause area.

Figure 3.2 demonstrates the variations in tropopause location generated using different tropopause definitions in the storm-perturbed (left panel) and post-storm, non-perturbed (right panel) environments for the supercell case. The colored contours show the concentration of TR5, the boundary layer tracer. The black line shows the tropopause as defined by a constant altitude (z), the blue line shows the tropopause as defined by a constant stability ($d\Theta/dz$), the green line shows the tropopause as defined by a constant PV, and the white line shows tropopause as defined by a constant ozone concentration. The constant values for the various definitions were chosen by selecting the thermal and dynamic tropopause altitude from the initial sounding (both had identical altitudes at t = 0) and calculating the various definitions at that altitude. The constants are as follows: z = 10.875 km, $d\Theta/dz$ = 0.00935 K/m, PV = 2.245x10^{-6} K kg^{-1} m^2 s^{-1}, and ozone (TR1) = 0.5 kg/kg. Here, PV is defined as Ertel's PV, $(\vec{\zeta} + f\hat{k}) \cdot (\rho^{-1} \frac{d\Theta}{d\vec{x}})$. The midlatitude tropopause is often defined by the 2 PVU (potential voticity units) surface, where 1 PVU = 10^{-6} K kg^{-1} m^2 s^{-1}.

The PV surface is discontinuous at both times. PV is useful for analyzing synoptic scale features on the tropopause, but at cloud-scale the PV surface is made noisy by the relative vorticity term. The vertical relative vorticity term dominates the relative PV because it is dotted with the only significant gradient in Θ, the vertical gradient. Figure 3.3 shows the TR5 tracer plume (colored contours) at 6 hours with the relative vertical vorticity (purple line) overlain . The solid lines indicate positive relative vorticity with a magnitude greater than the planetary vorticity; the dashed lines indicate negative relative vorticity with a magnitude greater than the planetary vorticity. Magnitudes on the order of the planetary vorticity add noise to the PV surface, making the PV definition useless for defining the tropopause around the storm anvil.

However, the vertical component of the Θ gradient, the thermodynamic portion of PV, is a much clearer indication of the tropopause location. Perturbed at early times by the strong vertical motion in the storm, the $d\Theta/dz$ surfaces have relaxed by 6 hours to a quasi-planar surface (figure 3.2).

Because the phenomenon we are most interested in is not the lofting of tropospheric air

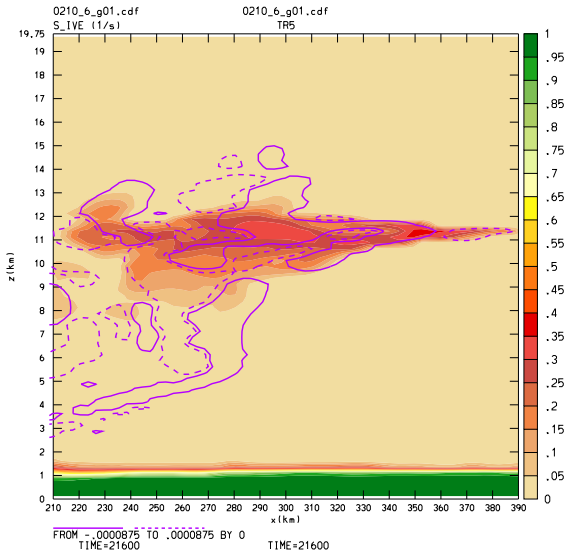

Figure 3.3: TR5 tracer plume (colored contours) at 6 hours in the supercell regime. Purple lines show the relative vertical vorticity at 8.75e-5 s^{-1} (solid lines) and -8.75e-5 s^{-1} (dashed lines).

but the actual mixing of two chemical regimes, namely the boundary layer tracers mixing with stratospheric tracers, the most appropriate tropopause definition for determining irreversible tracer transport into the stratosphere is ozone concentration (Danielsen, 1985), represented by TR1 in this model. It should be noted that ozone is not always a clear indicator of stratospheric air, as high ozone values can also be caused by transport of ozone-polluted boundary layer air (Dickerson (1987), Strom et al. (1999)). It would be helpful to measure other stratospheric tracers, such as N_2O or methane, in future cloud transport campaigns to eliminate the ambiguity.

But, we have simulated a storm in an unpolluted area with zero ozone in the troposphere, so high ozone levels indicate stratospheric air. One can see from figure 3.2 that little mixing has occurred between the two air masses. We argue that air that has been pushed through the stability boundary of the strong $d\Theta/dz$ gradient will remain lofted long enough that the mesoscale mixing processes such as gravity wave breaking can mix the tropospheric and stratospheric chemicals together. Such stratospheric mixing processes

are not included in this mesoscale simulation, but a rough estimate of 3 days for mixing time can be calculated following Haynes (2002). This lack of mesoscale mixing processes in our model stratosphere means that ozone (TR1) as a tropopause definition will underestimate troposphere-to-stratosphere exchange. We therefore use the $d\Theta/dz$ definiton for the tropopause altitude in the results that follow. The $d\Theta/dz$ definition was also user in the total transport plots in the preceding chapter.

Although not show in figure 3.2, a constant Θ surface would be another reasonable choice for the tropopause definition and has the advantage of being uniquely defined in the storm-perturbed environment while the $d\Theta/dz$ surface is not uniquely defined. The $d\Theta/dz$ surface was ultimately chosen as the best tropopause definition, however, because areas of higher stability are less likely to experience deep vertical displacement in the mesoscale and synoptic scale mixing processes discussed above and therefore more likely to remain in the stratosphere.

3.2.1 Relaxation of isentropic surfaces

Much of the energy in the storm-perturbed surfaces is dissipated without mixing tracer into the stratosphere. Figure 3.4 shows the snapshots of a cross-section through a dissipating updraft. The Θ surfaces are strongly perturbed above the strongest updrafts. The strongest updrafts reach 13.75km, almost 3km above the unperturbed tropopause level. The Θ surface at the level of the unperturbed tropopause is likewise perturbed upwards 1 km and downwards 3 km. Energy is dissipated by the gravity waves that propagate vertically away from the originaly perturbed surface. The colored contours show Θ surfaces and the zero line is equal to 388.15 K, the original tropopause surface. Note the gravity waves emanating away from the top of the updraft. Although small-amplitude waves do exist inside the tracer plume, near the updraft core, most energy is contained in the upward propagating gravity waves.

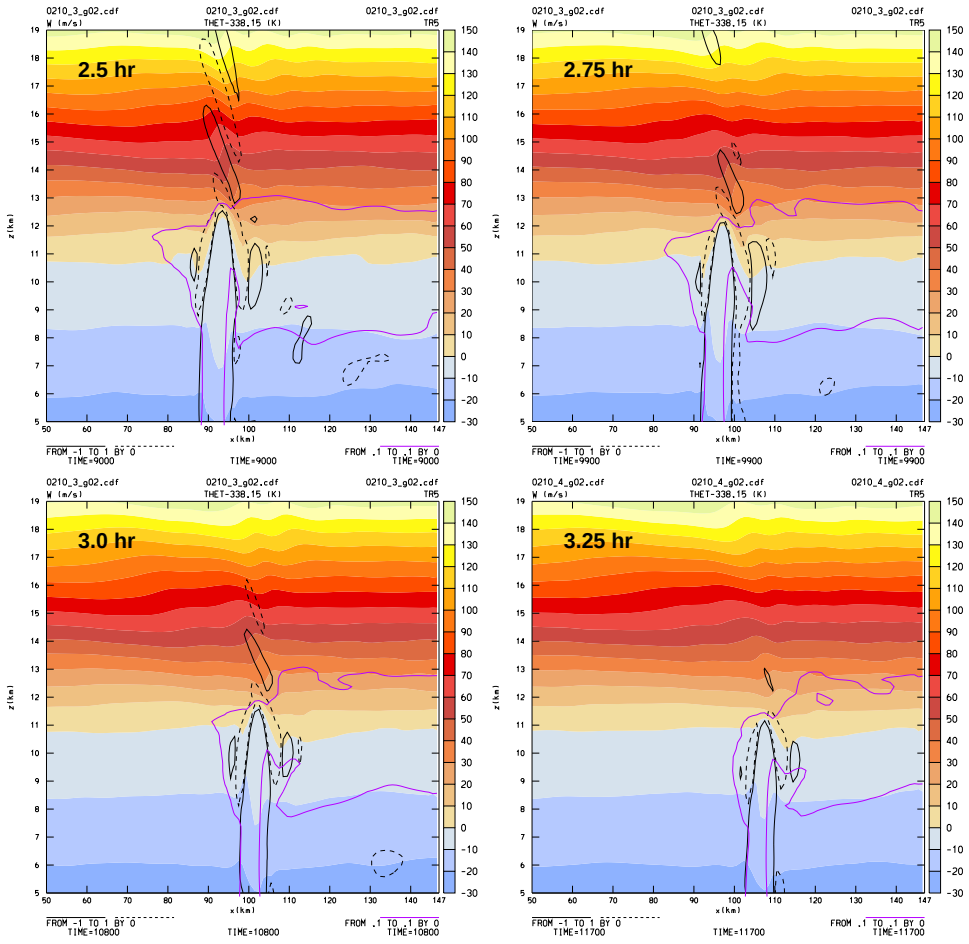

Figure 3.4: Cross section through dissipating updraft at 2.5, 2.75, 3.0 and 3.25 hours. Colored contours are (Θ - 338.15 K). Black lines show vertical velocity at 1 m/s (solid line) and -1 m/s (dashed line). Purple line shows TR5 equal to 0.10 kg/kg.

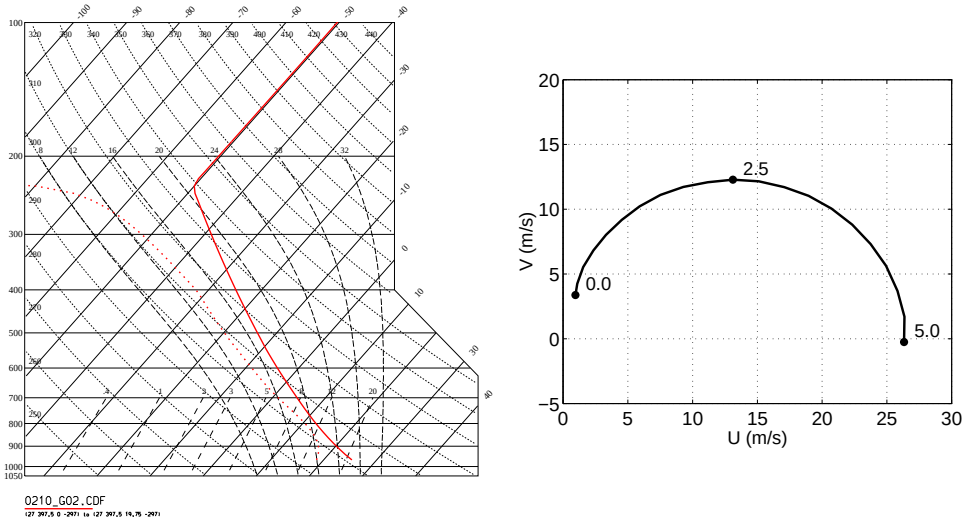

Figure 3.5: Initialization values for the idealized supercell storm. Left panel: Skew-T plot showing temperature (solid line) and dewpoint temperature (dotted line). This profile has a CAPE of 2500 J/kg. Right panel: Hodograph showing the low level wind shear. Numbers at points on line give altitude in km. This case has no wind shear above 5 km.

3.3 Idealized supercell storm

3.3.1 Initialization

The supercell storm was created using idealized thermodynamic and wind profiles (Weisman and Klemp, 1986). Figure 3.5 shows the thermodynamic profile (left panel) and the wind profile (right panel). This storm has CAPE of 2500 J/kg and zero wind shear above 5 km.

The storm type was determined according to the value of the bulk Richardson number (BRN), a ratio of CAPE over low-level wind shear.

$$\mathrm{BRN} = \frac{2\mathrm{B}}{\mathrm{U}^2}$$

$$\mathrm{B} = \mathrm{g} \int \frac{\Theta_\mathrm{p}(\mathrm{z}) - \Theta_\mathrm{e}(\mathrm{z})}{\Theta_\mathrm{e}(\mathrm{z})} \mathrm{dz}$$

where B is the buoyant energy (CAPE), g is the acceleration due to gravity, Θ_p is the potential temperature of the lifted air parcel, Θ_e is the potential temperature of the environment, and U is the density-weighted mean wind in the lowest 6 km minus the surface wind. A

sampling of storms by Weisman and Klemp (1982) showed the BRN range for supercells to be 10 to 50. This supercell has a BRN of 35.

Note that the model stratosphere was initially almost completely dry. The stratospheric water vapor mixing ratio was everywhere less than 1e-6 kg/kg and decreases to zero within 0.5 km of the tropopause. The stratosphere was made dry so that there would be no doubt that any cloud formation in the stratosphere would be due to water transported up from the troposphere. This should provide a conservative estimate of mass transport into the stratosphere because it should lead to increased evaporation of cloud particles transported into the stratosphere and should cause increased cooling and pull a greater amount of lofted tropospheric air down from the stratospheric levels than would occur in a moist stratosphere. This dry stratosphere is used in all model runs.

A latitude of 37° was assumed; f was set to 8.57×10^{-5} for the f-plane approximation. This Coriolis parameter was used for all model runs.

Grid nesting was used in order to reduce the computational expense of the model runs while having a large enough domain to capture the tracer plume advection. The inner grid, which contained all of the deep updrafts, had a horizontal resolution of 1 km and a vertical resolution of 250 m. The outer grid had a horizontal resolution of 3 km and a vertical resolution of 250 m. Figure 3.6 shows a horizontal cross section of the inner and outer domains. Both grids had a depth of 20 km. In order to follow the motion of the storm itself, both domains have a translation speed 11.1 m/s in the x direction and 6.4 m/s in the y direction.

3.3.2 Simulation overview

After 30 minutes into the simulation, one updraft cell is present and reaches a height of 13.75 km with maximum vertical velocity of 41 m/s at 9.5 km. The initial cell has a radius of 5 km which is the approximate radius of the subsequent updrafts in the supercell case. The downdrafts that flank this main cell are much weaker than the updrafts, with a maximum downward velocity of 8 m/s. At midlevels (3-7 km), the main downdraft lies downwind of the updraft, associated with the evaporation of falling hydrometeors. From

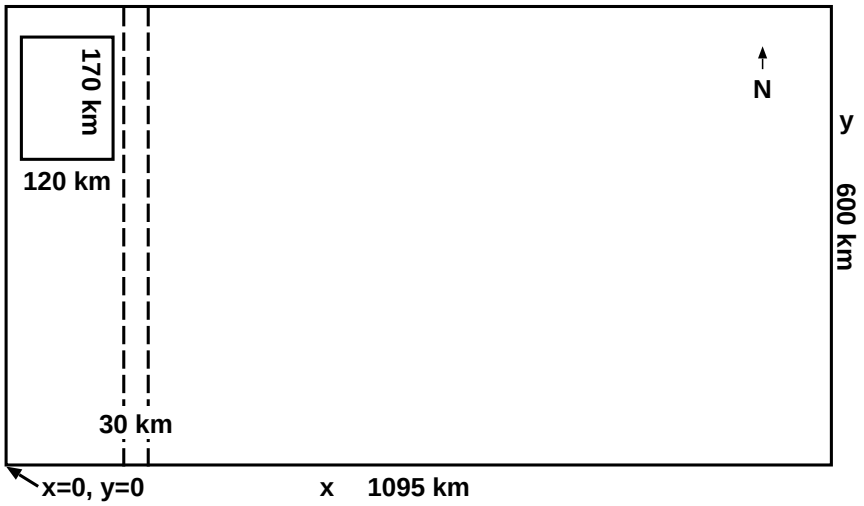

Figure 3.6: Inner and outer grids used for supercell simulation. The transistion zone between the moist boundary layer (west) and the dry boundary layer (east) is shown by the dashed lines.

8-12 km, the downdraft maximum is upwind from the updraft, created by a combination of diabatic cooling due to evaporation caused by the entrainment of dry air into the cloud and subsidence caused by dynamical adjustment to the upward flux of air. Above 12 km the downward air motions are due to gravity waves generated by the overshooting convective tower.

The updraft strength surpasses 50 m/s by 45 minutes and remains this strong until 2 hours into the simulation. This persistent strong vertical velocity is a signature of a supercell storm (Weisman and Klemp, 1986). The eastern edge of the storm reaches the dry region at approximately 1.5 hours and the storm begins to dissipate at this time. At the time the dry air mass is encountered, the vertical velocity at 9.5-10.5 km has reached a storm maximum of 60 m/s. The updraft reaches a maximum height of 14.25 km.

The storm anvil, here defined as a total hydrometeor mixing ratio of greater than or equal to 0.1 g/kg, has a maximum extent of 5000 km^2 at 11.125 km at 2 hours (figure 3.7, solid blue line). The anvil is mostly due to snow at this level because the cloud ice evaporates instantaneously in subsaturated air, while the snow has a longer sublimation time. The

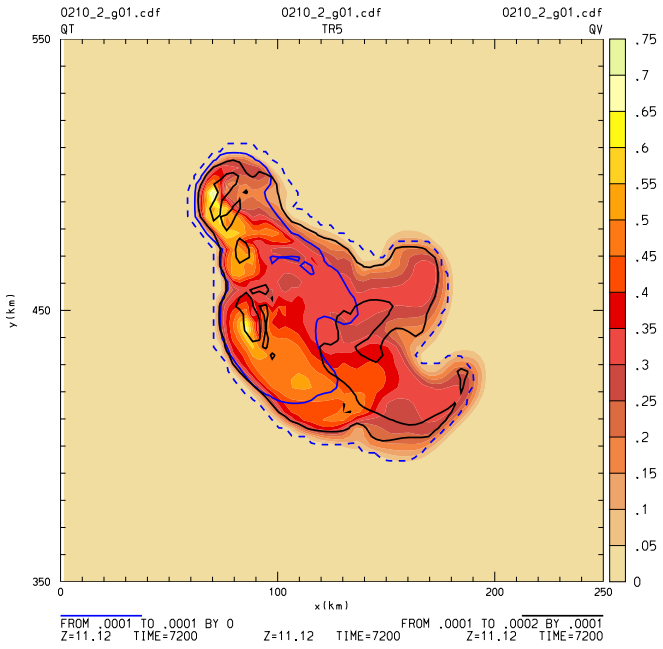

Figure 3.7: Boundary layer tracer (TR5) plume at height of 11.125 km at 2 hours. Contour interval is 0.05 kg/kg. Blue lines show cloud/ice water mixing ratio of 0.1 g/kg (solid) and 10^{-6} g/kg (dashed). Black line show water vapor mixing ratio of 0.1 g/kg.

largest anvil extent due to a single cell is approximately 600 km^2. This maximum in the anvil extent occurs one vertical grid step above the unperturbed tropopause level, nearest to the level of neutral buoyancy.

The boundary layer tracer plume, defined as parcel of air with a TR5 mixing ratio of 0.01 kg/kg or greater, covers a much larger area than the storm anvil at 2 hours (figure 3.7, colored contours). The larger size of the tracer plume is not surprising, as the tracer remains in the advecting air parcels even after the hydrometeors have evaporated. Stenchikov et al. (1996) also found the "chemical anvil" had a larger area than the hydrometeor anvil in their model run.

The extent of cloud ice/water does match the tracer plume, however, if the concentration is chosen low enough. The dashed blue line in figure 3.7 shows the contour of cloud ice/water with a mixing ratio of 1e-6 g/kg, which closely follows the storm anvil. The fact that some

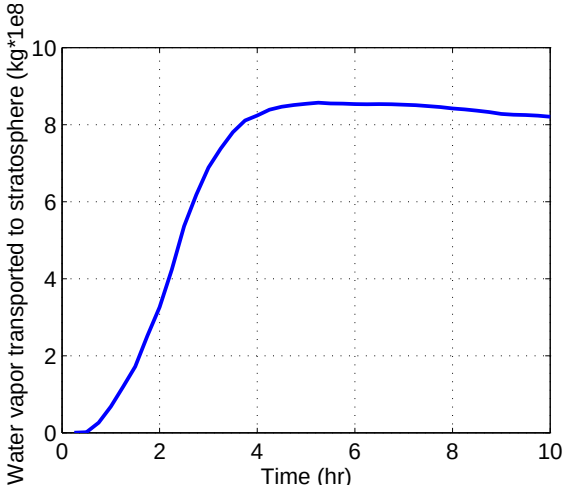

Figure 3.8: Total mass of water vapor transported into the stratosphere by the supercell storm detailed in section 3.3. Calculated by summing the change in water vapor amount above the $d\Theta/dz$ tropopause.

hydrometeors exist throughout the extent of the tracer plume is also not surprising. The hydrometeor anvil could prove useful in the estimation of the tracer plume, but it is unclear at what concentration the storm anvil is still visible and if subvisible, at what concentration the storm anvil is still detectable.

The black line in figure 3.7 shows the water vapor mixing ratio at 0.1 g/kg. As suggested by Wang (2003), water vapor injection into the stratosphere does appear to occur above deep convection. Figure 3.8 shows the total amount of water vapor that has been transported into the stratosphere by the supercell simulation. The microphysical parameterization has been calibrated to correctly simulate cloud formation and precipitation processes in the troposphere, but it is unclear that the parameterization properly describes lower stratospheric water processes. Further water vapor transport results are not addressed in this thesis due to this uncertainity. Nevertheless, the fact that at least some water vapor is being injected at middle latitudes seems certain.

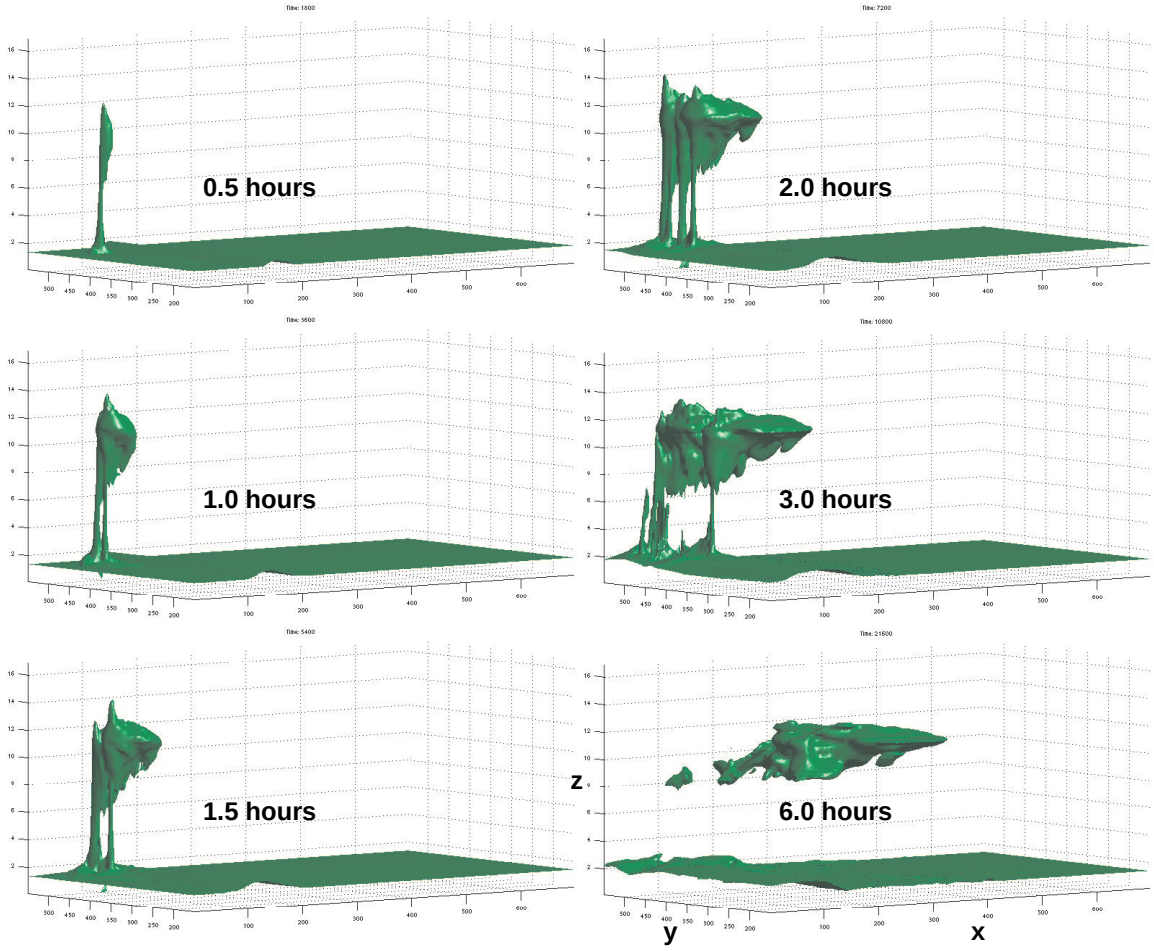

Figure 3.9: Isosurface of TR5 = 0.1 kg/kg at 0.5, 1, 1.5, 2 ,3 and 6 hours into the supercell simulation. The portion of the model domain shown is x = 0 to 700 km, y = 150 to 550 km, and z = 0 to 17 km.

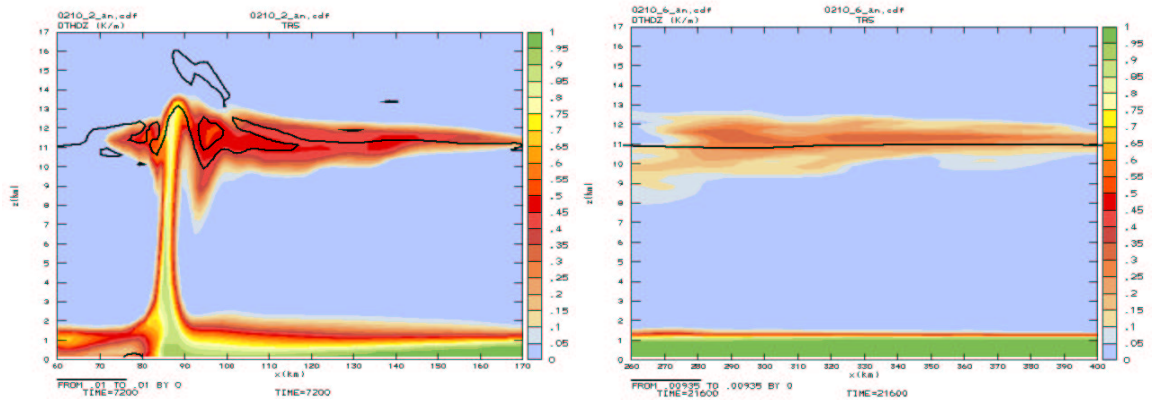

Figure 3.10: Vertical cross-section through supercell anvil at 2 hours (left panel) and 6 hours (right panel). The colored contours show the concentration of tracer TR5. The thick black line shows the location of the $d\Theta/dz = 0.00935$ isosurface.

3.3.3 Results

Figure 3.9 shows snapshots of an isosurface of the boundary layer tracer, TR5, with a concentration of 0.1 kg/kg (i.e., 10% of its initial boundary layer value). The tracer is pulled up in the deep updrafts and is deposited near the level of neutral buoyancy. Although tracer-rich air reaches the highest altitudes in overshooting tops, 14 km, that air descends with little or no deposition taking place in the anvil overshoots.

If the wave motions at cloud top are entirely adiabatic, then the tracers move up and down with the wave. If the motions are partially non-adiabatic, however, then some of the tracer material can be left behind. The lofted air will remain in the stratosphere via one, or both, of the following two processes. One, enough latent heating takes place to make the lofted air buoyantly neutral at its new altitude. Two, the lofted air undergoes dynamical mixing at cloud top which raises the parcel's temperature enough to be buoyantly neutral. These processes will be discussed further in section 3.3.

Figure 3.10 shows vertical slices through the TR5 tracer plume at 2 hours (left panel) and 6 hours (right panel). The color contours of TR5 show concentrations from 0 kg/kg to 1 kg/kg, with an interval of 0.05 kg/kg. The thick black line represents the tropopause

defined using $d\Theta/dz$. At 2 hours, the tropopause is highly deformed, but by 6 hours, the tropopause has become quasi-planar. At 2 hours, the tracer extends above 13 km. By 6 hours, the tracer has become less perturbed and although small concentrations have mixed at higher altitudes, very little tracer exists above 13 km.

Figure 3.11 shows the mass transport versus altitude for each tracer. Panel A shows the total mass at each level summed over the entire domain. Panel A is dominated by large scale transport like diffusion and subsidence and looks very similar to the total mass at the initialization time (0 hours, shown in Panel B). Panel C shows the final total mass minus the initial total mass (Panel A- Panel B) which emphasizes the large scale transports.

In order to isolate the convective transport, we plotted the curves from Panel A, but only show the totals at altitudes outside the large scale transport (Panel D). We found that the domain-wide transport extends approximately 1.5 km outside of each tracer "source" region. For example, the inital region for TR3 is 4.625 km to 7.125 km, and the final mass profile for TR3 is plotted from 3.125 km to 8.625 km. The original boundaries between tracer layers are shown by the gray lines.

It is clear from figure 3.11 that while all the tropospheric tracers have had some mass transported into the stratosphere, the most transport is of TR5 and TR4, with TR5 dominating. Also evident from panel D of figure 3.11 is the significant amount of mass deposited above the level of neutral buoyancy (11.125 km). Air parcels that remain above the LNB have entrained higher Θ air from above (from the stratosphere) to increase the parcels' temperature beyond the temperature that could be reached from latent heating alone. Poulida et al. (1996) used a mixing line argument to show that unlike the traditional view of mixing of tropospheric and stratospheric air happening only in the overshooting top, some mixing must be occurring in the anvil as well.

Figure 3.12 shows contours (solid lines) of the mixing coefficient between the altitude of the LNB and 13.875 km at several output times. The anvil outline is also shown at the LNB (dashed line). While the mixing at the highest levels only occurs in the overshooting top, mixing is going on throughout the anvil and even in some areas outside the anvil. This mixing increases the opportunities for tropospheric air to reach a potential temperature that will allow the air to remain in the troposphere. See appendix B for further details on

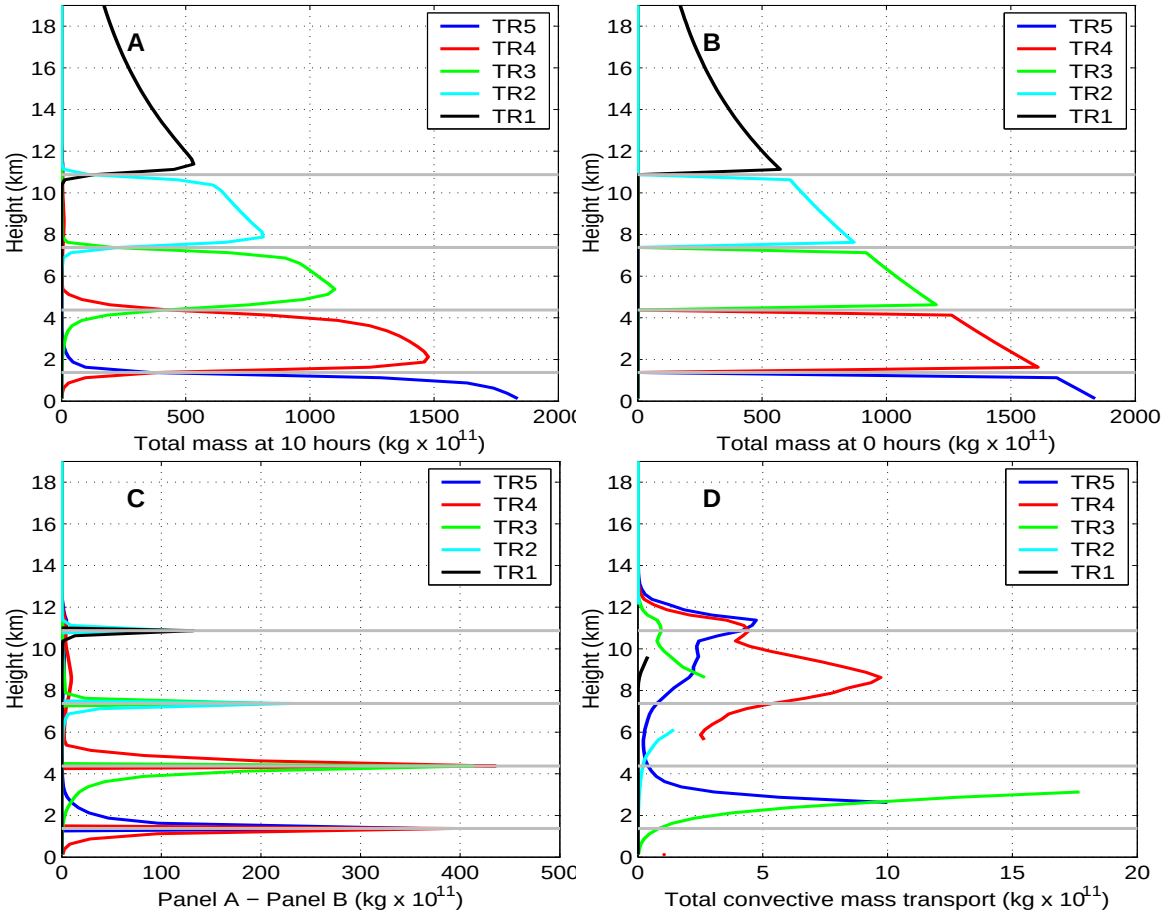

Figure 3.11: Mass transport versus altitude. TR5 is shown in blue; TR4, in red; TR3, in green; TR2, in cyan; and TR1, in black. Panel A: the total mass at 10 hours summed over the entire model domain. Panel B: the total mass at 0 hours summed over the domain. Panel C: the total mass at 10 hours (Panel A) minus the total mass at 0 hours (Panel B). Panel D: the total convective mass transport at 10 hours (see text for details). The gray lines indicate the original locations of the tracer layers.

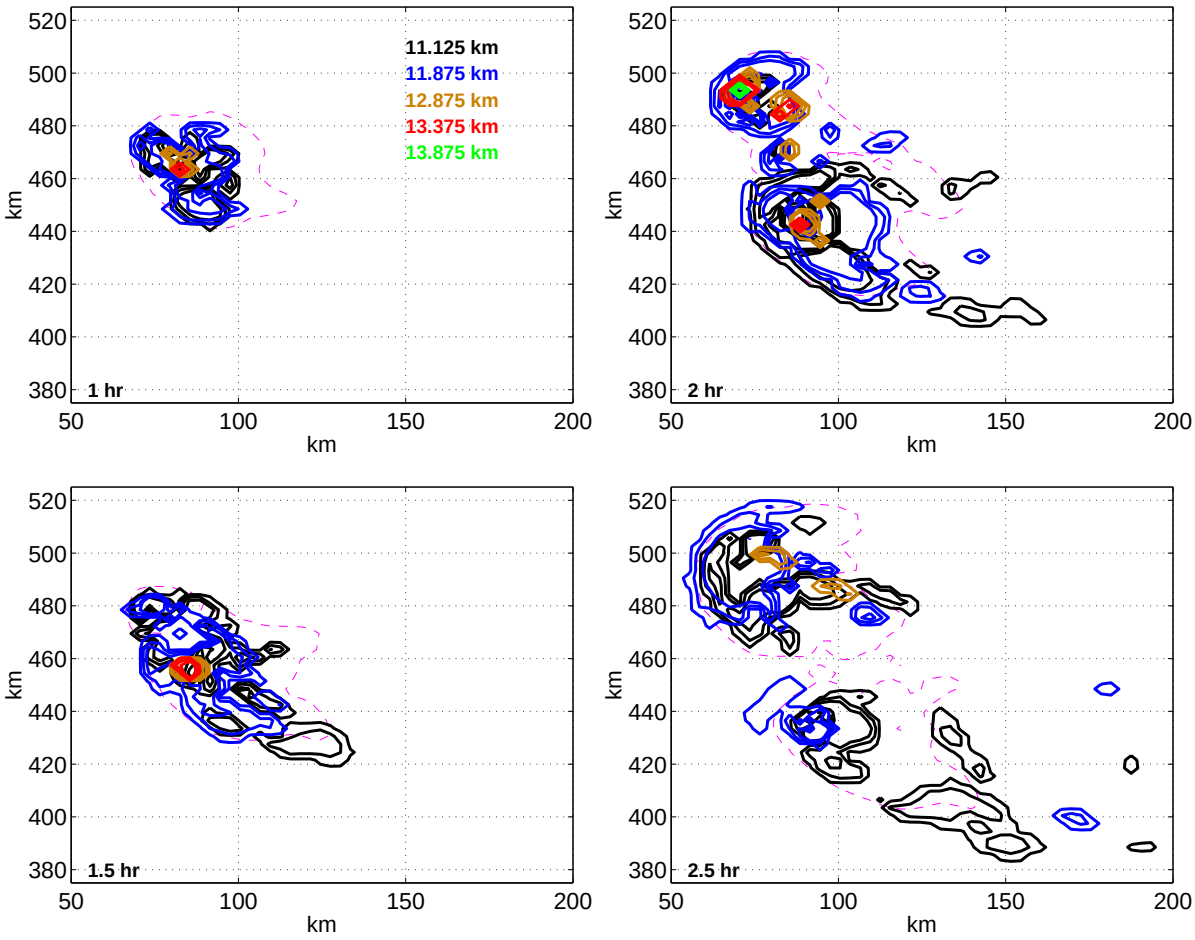

Figure 3.12: Contours of the mixing coefficient (solid lines) in the supercell storm at altitudes at, and above, the level of neutral buoyancy shown at 1, 1.5, 2 and 2.5 hours. Contour shown are 10, 50 and 100. The dashed line shows the cloud outline (liquid water mixing ratio $\geq 1e^{-4}$ kg/kg) at 11.125 km.

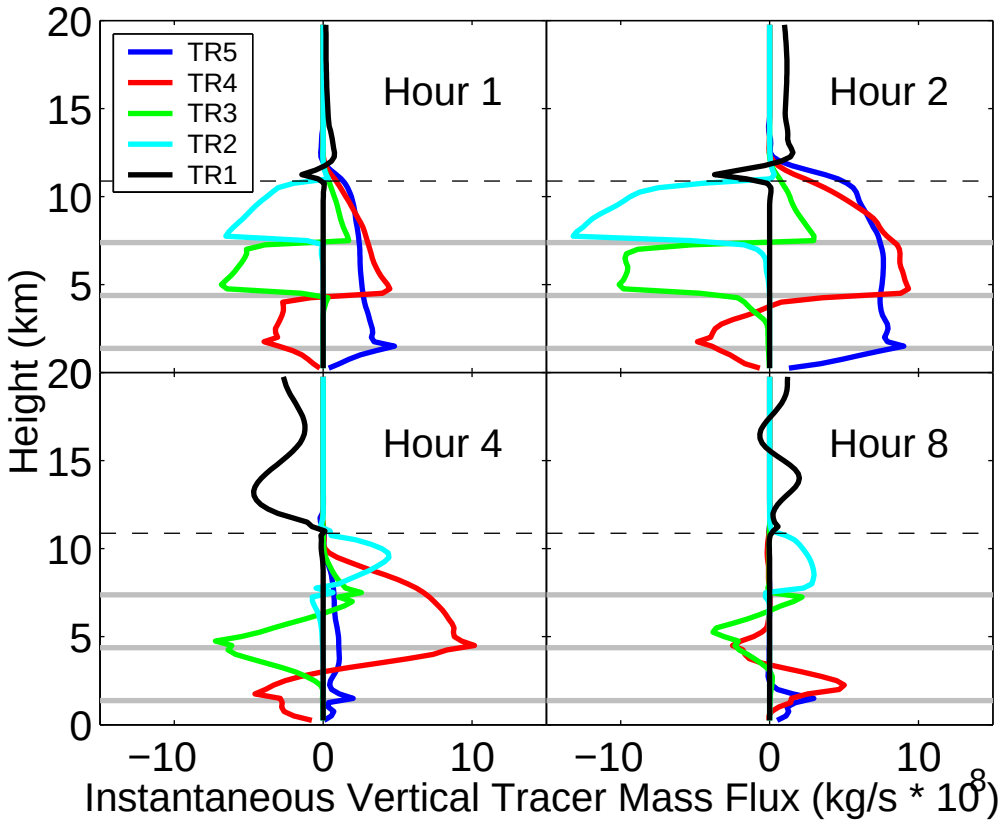

Figure 3.13: Instantaneous vertical tracer mass flux summed over the horizontal model domain at 1, 2, 4 and 8 hours. The dashed line shows the location of the unperturbed tropopause altitude. The gray lines show the initial boundaries between tracer layers.

the mixing coefficient.

Figure 3.13 shows the instantaneous vertical tracer mass flux for all five of the idealized tracers. The stratospheric tracer, TR1, is pushed upwards by the convective turrets at hours 1 and 2, showing a downward flux just above the tropopause where stratospheric air is carried downward in compensating downdrafts surrounding the anvil, and pushed upwards above the anvil. By hour 4, the stratospheric gravity waves have reached the model boundaries and no longer cancel out, giving TR1 mass flux a wavelike structure.

TR2 is dominated by downdrafts in hours 1 and 2. Although a small amount of TR2 is pushed upwards above the anvil, the bulk of TR2 is pushed out of the way and entrained

into subsiding air around the updrafts. At hours 4 and 8, TR2 is advected upwards in remnant updrafts.

TR3 is the simplest to understand. Above the initial tracer layer, TR3 exists primarily in the updrafts, pushed up atop the rising parcels. Within the initial TR3 layer, air is pushed laterally by the updrafts and entrained into the downdrafts.

The same is true for TR4, for hours 1, 2 and 4; TR4 primarily exists in updrafts above the initial layer and primarily in downdrafts in the initial layer and lower. The fact that the tracers have upward flux above their initial layers is as expected; the only process by which material can exist above its source region is through upward fluxes. The upward transport of TR4 is much stronger than TR3. This is either due to more entrainment through mixing into the updrafts within the TR4 layer, or direct input into the updrafts because air parcels originate in the TR4 layer. Figure 3.14 shows a sampling of back trajectories (right panel) from a section of the tracer plume that has a minimum 0.1 kg/kg concentration of TR3, TR4 and TR5 (left panel) at 11.125 km, one model grid step above the unperturbed tropopause and the grid level nearest the level of neutral buoyancy. The back trajectories are shown from above; the color of the trajectory shows the origination altitude, determined from the trajectory itself. The trajectories were calculated back in time until either the initial model time was reached (t = 0) or the parcel left the domain. Most parcels originated in the boundary layer (TR5, 0-1.375 km), although some inflow did occur in the TR4 layer (1.375-4.375 km) and the TR3 layer (4.375-7.375 km). More than twice as many trajectories originated in the TR4 layer as in the TR3 layer.

TR5 shows upward flux in updrafts at all tropospheric levels. Even in the boundary layer, where there are strong downdrafts pushing TR5 downwards, there is insufficient entrainment into the downdrafts to outweigh the strong upward transport. TR5 has highest mass flux of all the tracers into the stratosphere (hours 1 and 2) because TR5 is at the core of the updraft and less is entrained away as the updraft experiences turbulent mixing throughout its depth. Figure 3.15 shows slices through the updrafts at 1.5 hours, at 2.5, 5, 7.5 and 10 km and shows the vertical velocity in colored contours with the TR5 (black lines) and TR4 (purple lines) concentrations overlain. At 2.5 km, the contours show a peak in TR5 that coincides with a hole in the TR4 concentrations. Above the TR4 layer, the contours clearly

B

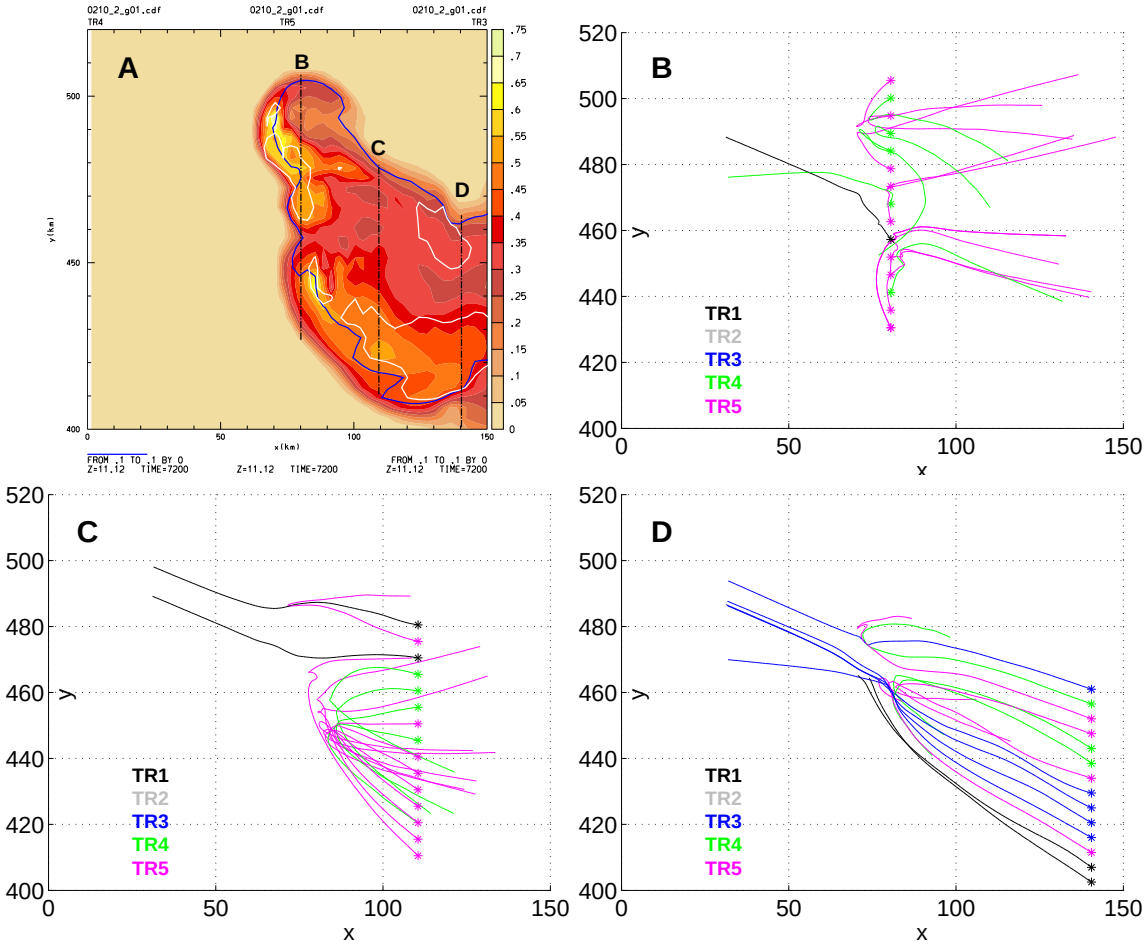

Figure 3.14: Panel A: colored contours show the TR5 tracer plume with contour intervals of 0.05 kg/kg at 11.125 km, 2 hours into the simulation. TR4 = 0.1 kg/kg is shown by the blue line and TR3 = 0.1 kg/kg is shown by the white line. The black dash-dot lines show the starting locations of the back trajectories show in the panels B (left line), C (middle line) and D (right line). Panels B-D: back trajectories computed for parcels starting at starred locations. Color of trajectory indicates origination layer. Black indicates stratosphere (> 10.875 km), gray indicates TR2 layer (7.375 to 10.875 km), blue indicates TR3 layer (4.375 to 7.375 km), green indicates TR4 layer (1.375 to 4.375 km) and magenta indicates TR5 layer (surface to 1.375 km).

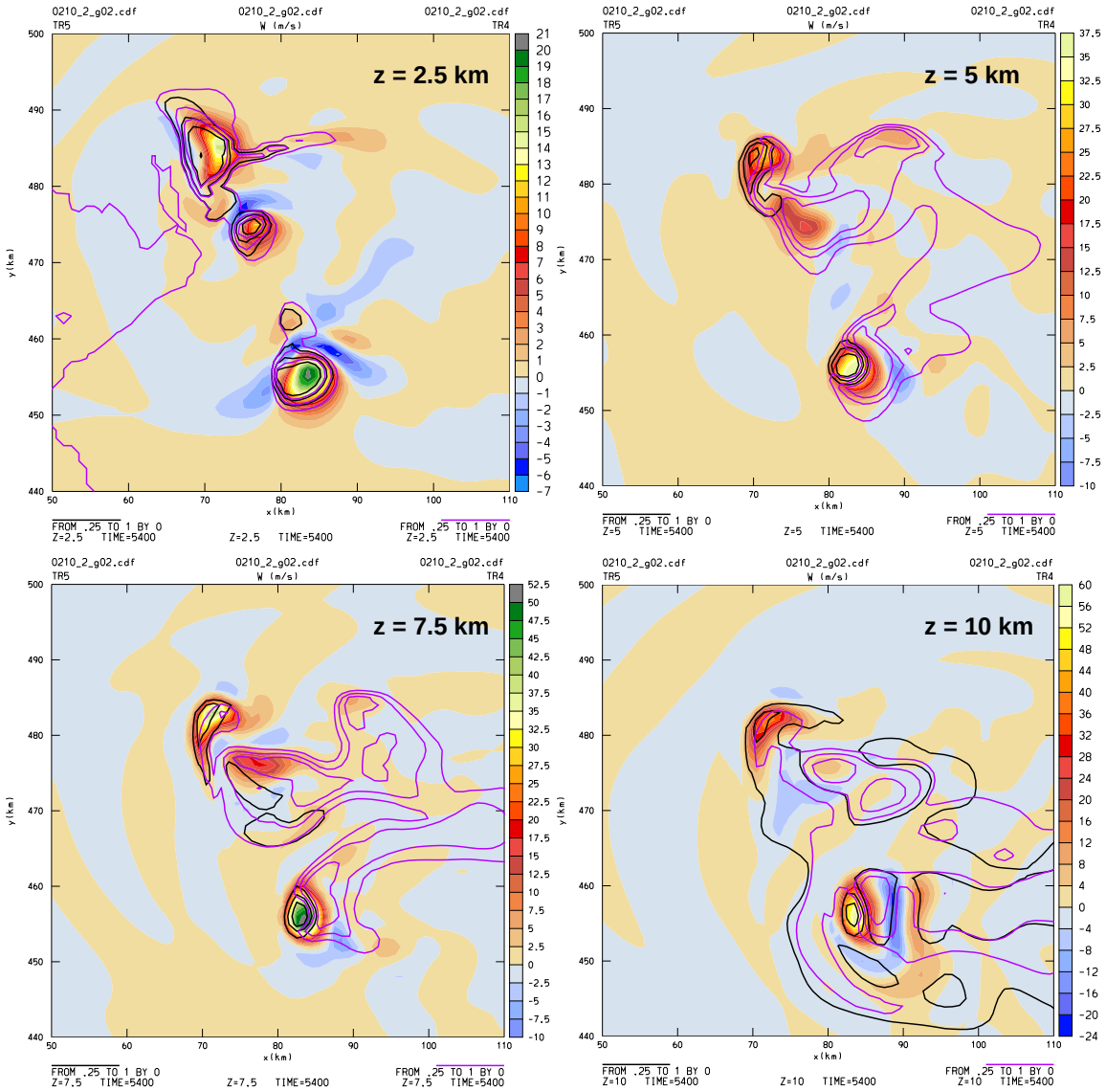

Figure 3.15: Slices through the storm updrafts at 1.5 hours at the altitudes 2.5, 5, 7.5 and 10 km. The colored contours show vertical velocity. The lines overlain show the passive tracer concentrations at 0.25, 0.5, 0.75, and 1.0 kg/kg for TR5 (black) and TR4 (purple). Note the 2.5 km slice is in the TR4 layer, so the contours show a hole in the layer, not a peak.

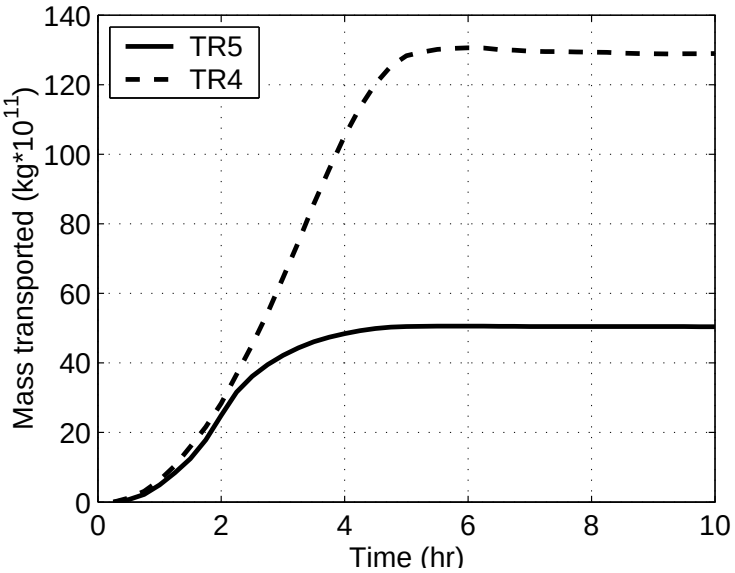

Figure 3.16: Total amount of TR5 (solid line) and TR4 (dashed line) transported above 6 km in the supercell storm.

show that the peak values in TR5 coincide with the strongest updraft location while the peak TR4 concentrations are offset, consistent with the TR4 tracer being pulled up on the flanks of the updraft rather than in the core.

From approximately 4 to 10 km at 4 hours, the larger TR4 transport (shown in figure 3.13) is due to cell remnants that no longer extend down to the surface. The dry air mass efficiently shuts down the updrafts originating from the surface, but cells then continue to transport air from the elevated layer, the TR4 source layer. Also, some cells already had an elevated base and are not strongly affected by the dry air mass. Figure 3.16 shows the total transport above 6 km for both TR5 (solid) line and TR4 (dashed line) as a function of time. Notice that during the initial and mature stages of the storm (approximately 0-2 hours) the amount TR5 transported is nearly equal to the amount of TR4 transported. But during the dissipation phase of the storm (approximately 2-5 hours), after the dry air mass has been encountered and low level inflow shut down, TR4 dominates the transport.

Figure 3.17 shows the total amount of various tracers transported into the stratosphere

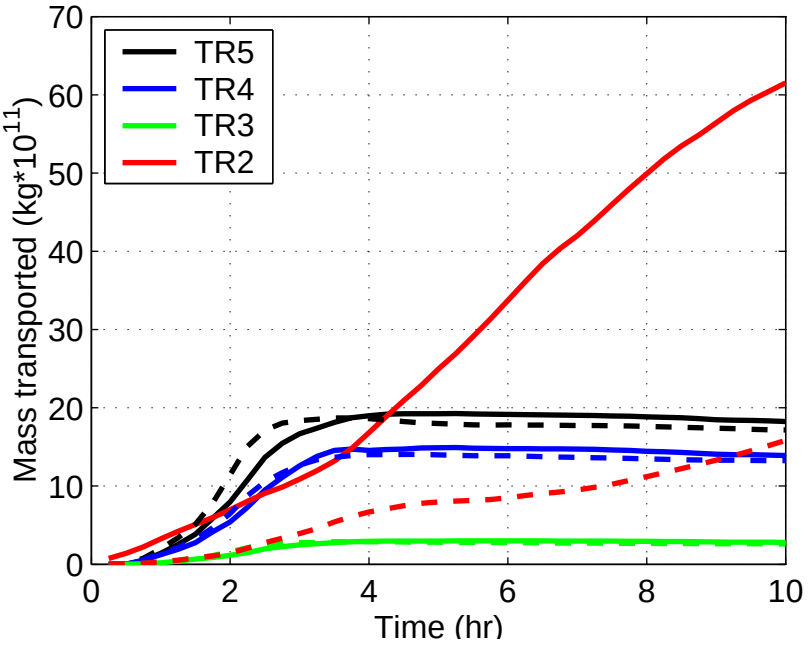

Figure 3.17: Total amount of tracer transported into the stratosphere. Solid lines show total transport using $d\Theta/dz$ as the tropopause definition; dashed lines show total transport above a constant altitude.

in the simulation. Total mass transport was calculated by finding the areas of the model domain that had a $d\Theta/dz$ value greater than or equal to the $d\Theta/dz$ value of the tropopause, including isolated parcles, if appropriate, and summing the mass of the tracers in those areas. The tracer mass was found by multiplying the tracer concentration by the air density at the given altitude. Since some air parcels in the lowest 1 km had high stability values in the cold pool region, the stability stratosphere definition is only applied above 5 km. This constraint of 5 km and above is reasonable because downdrafts at tropopause level were weak and did not push the stability tropopause lower than 9 km. The solid lines show transport using $d\Theta/dz$ as the tropopause definition. Dashed lines show transport calculated by summing all the tracer mass above the altitude of the initial unperturbed tropopause. Note that these totals are instantaneous totals, not cumulative.

For the lowest level tracers, TR5 and TR4, one can see the signature of the air parcels pushed beyond their level of neutral buoyancy from 0-4 hours; the amount of tracer above the initial tropopause altitude exceeds the amount above the stability tropopause. Although parcels have crossed a given height, they have not crossed the tropopause stability boundary.

After approximately 4 hours, the amount above the stability boundary exceeds the amount above the altitude tropopause. This is due to the descent of the stability boundary. Although the stability boundary has returned to quasi-planar, it has not returned to its original height. Figure 3.18 shows the domain-averaged $d\Theta/dz$ profile at 0 hours (solid line) and 10 hours (dashed line). The left panel shows the full profile; the profile at 10 hours has not deviated much from the original profile. Zooming in near the tropopause (right panel), however, shows that the average $d\Theta/dz$ at 10.875 km has increased; likewise the height of the $d\Theta/dz$ tropopause, defined as 0.00935 K/m, has decreased slighty in altitude.

TR2 shows a strong amount of mass transport into the stratosphere, even at the early times. This transport is clearly not due to vertical transport (figure 3.13) and must be the result of turbulent mixing or diffusion. Most of the transport of TR2 into the stratosphere is due to mixing caused by the virtual temperature gradient between the moist and dry air masses at the surface. This gradient causes a weak, but persistent, circulation that creates perturbations in the TR2 gradient and Θ gradient at tropopause height. The vertical extent of these perturbations is small above the tropopause, smaller than the vertical grid spacing

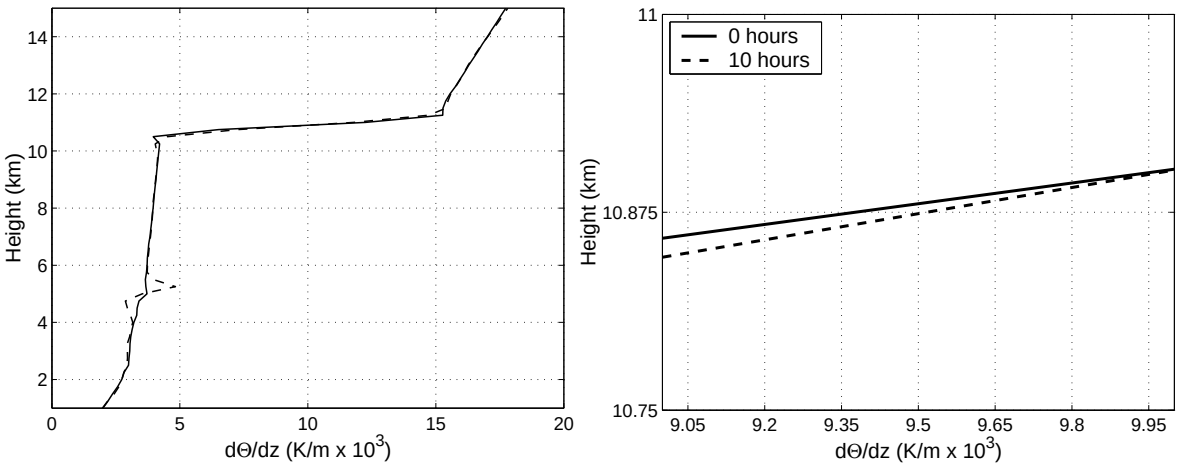

Figure 3.18: Left panel: domain-averaged $d\Theta/dz$ profile at 0 hours (solid line) and 10 hours (dashed line). Right panel: same as left panel, magnified in region of tropopause.

of 250 m, but because the theta perturbations radiate outwards in the domain, the diffusion of TR2 is enhanced domain-wide, causing a large transport. Figure 3.19 compares the transport of TR2 in the supercell storm with transport due to the dry air influx only (no storm). The no storm case actually exceeds the supercell case. Chapter 2 contains further details on transport contamination due to the artificial circulation caused by the dry air boundary.

Figure 3.17 suggests that a flat tropopuase definition is, in fact, a reasonable definition for assessing cross-tropopause transport. Hence, the results from several previous studies remain realistic, e.g. Skamarock et al. (2000) and Stenchikov et al. (1996). Stenchikov et al. (1996) ran their two dimensional squall line simulation to 12 hours and although the convection is still active even at 12 hours, it is reasonable to assume that the anvil edges most distant from the active convection are in relatively unperturbed air. It should be noted, however, that this same study found a decrease in vertical stability at the tropopause over the simulation (decrease in $\frac{d\Theta_e}{dz}$), casting additional uncertainty on the final state of the atmosphere.

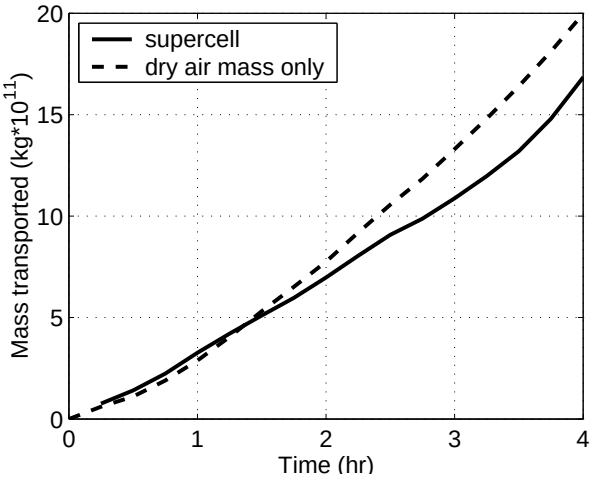

Figure 3.19: Total mass transported into the stratosphere by the supercell storm (solid line) and the simulation with the dry air influx but no storm (dashed line).

3.4 Multicell storm- 11km tropopause

3.4.1 Initialization

The multicell case had the same thermodynamic profile as the supercell case, but half the low-level wind shear (figure 3.20). Smaller wind shear raises the BRN to 115, putting the storm in the multicell regime of BRN greater than 35 (Weisman and Klemp, 1982). Like the supercell case, this wind profile contains zero shear above 5km.

3.4.2 Simulation overview

At 30 minutes, the multicell storm has a maximum vertical velocity of 50 m/s at altitudes of 9.875-10.625 km; the updraft has reached 13.5 km. The updraft strength reaches 50 m/s by 30 minutes but subsequently decreases in magnitude and doesn't surpass 50 m/s again until 1.25 hours. The individual cells in the multicell storm had an average lifetime of 45 minutes. The cells generally had a radius of 3-4 km.

The eastern edge of the storm reaches the dry region at approximately 1.5 hours and the storm begins to dissipate at this time. At the time the storm encounters the dry air mass,

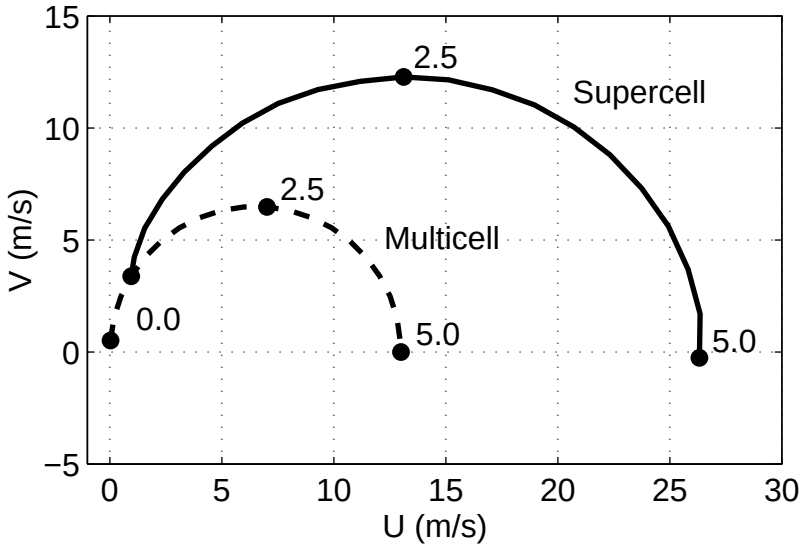

Figure 3.20: Hodographs showing the low level wind shear profiles in the supercell (solid line) and multicell (dashed line) cases. Numbers at points on lines give altitude in km. Neither case has wind shear above 5 km.

the vertical velocity from 10.25 to 10.5 km has reached a storm maximum of 57 m/s. The maximum updraft height is 13.75 km. The storm anvil, here defined as a total hydrometeor mixing ratio of greater than or equal to 0.1 g/kg, has a maximum extent of 3500 km^2 at 10.625 km at 2 hours.

3.4.3 Results

Figure 3.21 shows snapshots of an isosurface of the boundary layer tracer, TR5, with a concentration of 0.1 kg/kg. The storm develops in a manner similar to the supercell (figure 3.9) during the first 1.5 hours. By 2 hours, the less well sustained updrafts are evident and the more fragmented nature of the multicell can been seen, especially at 3 hours. At 6 hours, it is clear that less boundary layer material has reached the tropopause level.

The initial bubble strength and CAPE is identical in both idealized cases, but the multicell storm had higher mass flux at the earliest simulation times (see Figure 2.3, chapter 2). Deep convection more easily organizes in the multicell case because of lower wind shear

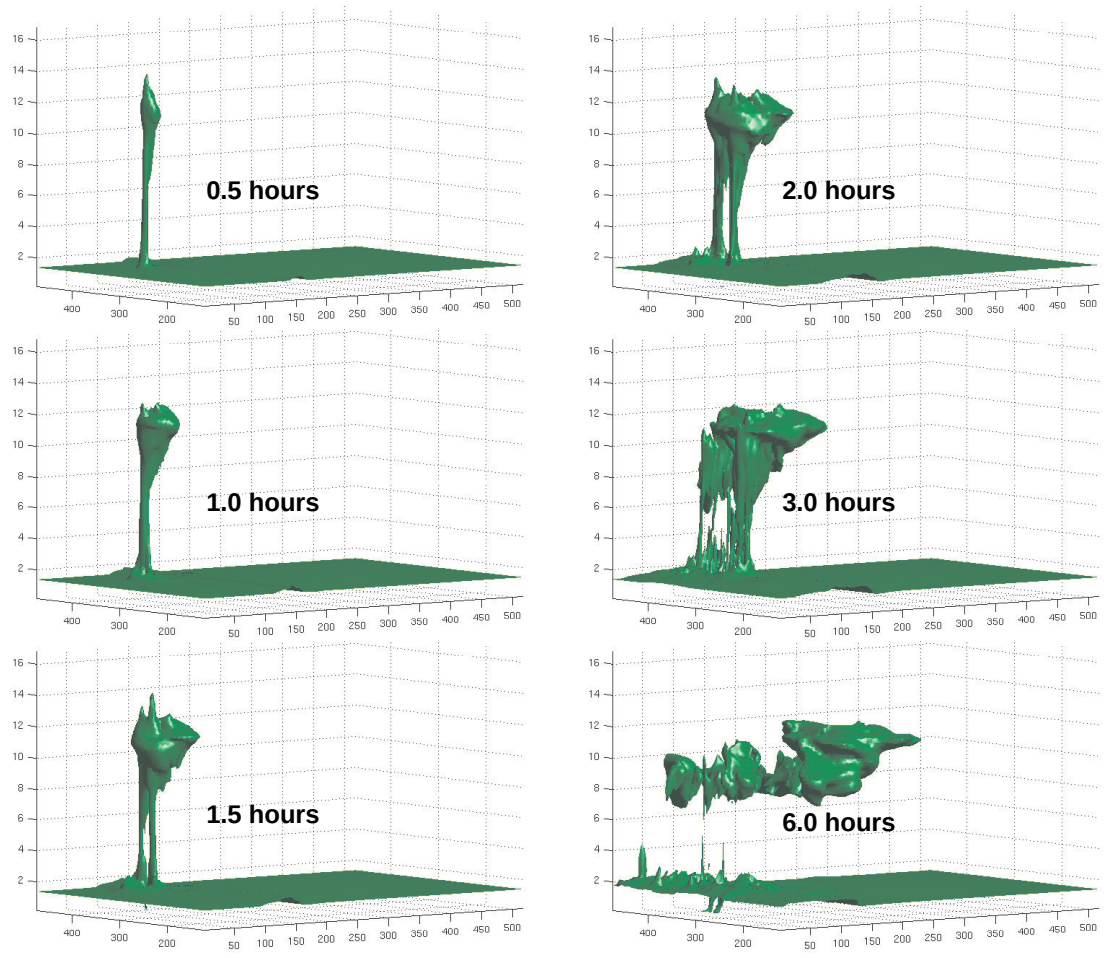

Figure 3.21: Isosurface of TR5 = 0.1 kg/kg at 0.5, 1, 1.5, 2 ,3 and 6 hours into the multicell simulation. The portion of the model domain shown is x = 0 to 520 km, y = 120 to 470 km, and z = 0 to 17 km.

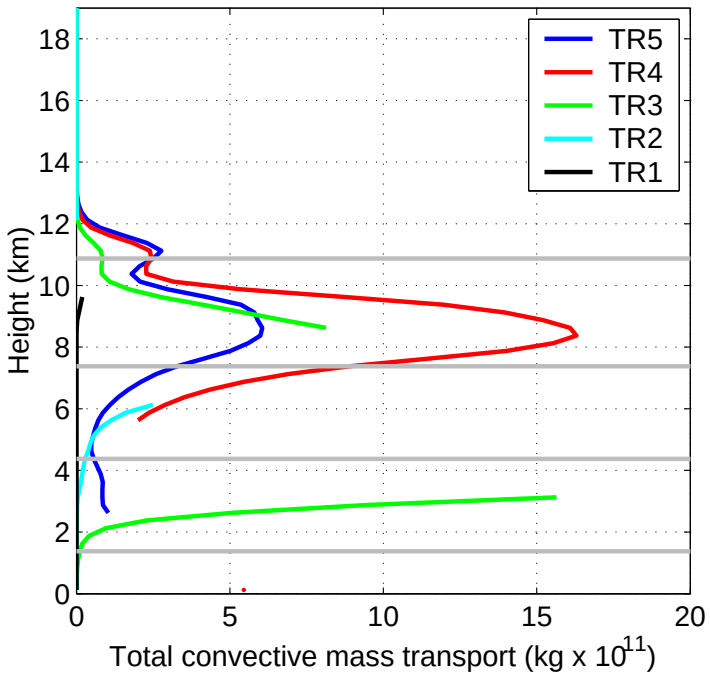

Figure 3.22: Total convective mass transport summed over entire domain at 10 hours into multicell simulation (same as panel D, figure 3.11). TR5 is shown in blue; TR4, in red; TR3, in green; TR2, in cyan; and TR1, in black. The gray lines indicate the original locations of the tracer layers.

magnitudes. After approximately one hour, however, the total mass transported into the stratosphere by the supercell storm exceeds the total mass transported into the stratosphere by the multicell storm. The greater transport by the supercell storm is due to three supercell storm characteristics: higher vertical velocities, longer cell lifetimes, and wider updrafts.

Figure 3.22 shows the total convective transport in the multicell storm. The same plot for the supercell storm (figure 3.11, panel D) shows a similar signature , the major differences being less transport into the stratosphere and more transport into the upper troposphere. TR3, TR4 and TR5 all show a bimodal structure in the upper troposphere/lower stratosphere, with a local minimum at approximately 10 km, below the tropopause location of 10.875 km. This bimodal structure is evident in the supercell storm mixing ratio plot as well, although less pronounced. Taking an average of the $d\Theta/dz$ field at 10 hours shows that

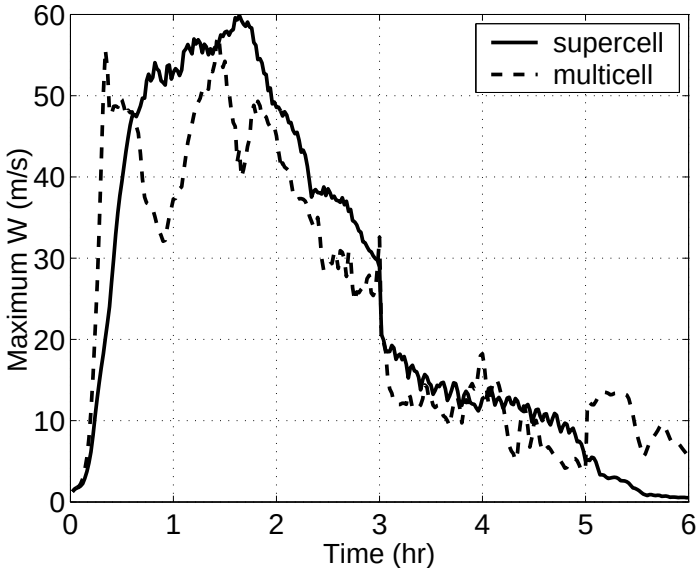

Figure 3.23: Maximum vertical velocity in the entire model domain for the supercell (solid line) and multicell (dashed line) storms.

the minimum in the bimodal structure is at the same height as the increase in $d\Theta/dz$. The maximum at 11.125 km is due to the expected maximum outflow at the LNB. The second maximum at approximately 9.375 km is due to later convection that lacks the energy to push across the stability boundary at the tropopause.

Both simulated storms had maximum updrafts of nearly 60 m/s, but the supercell storm produced very strong vertical velocities throughout the mature stage of the storm while updrafts in the multicell storm only achieved such strength during the initial rapid growth stage (figure 3.23). The oscillating maximum vertical velocity of the multicell regime is the signature of seperate cells growing and dissipating, while in the supercell regime, one supercell dominates for the first 2 hours. The multicell storm cells had an average lifetime of 45 minutes, while the strongest supercell updraft persisted for over 2 hours. The supercell storm (solid line) exceeds 50 m/s for a contiguous 1.25 hours, while the multicell storm (dashed line) exceeds 50 m/s for a total of approximately 20 minutes in two separate episodes.

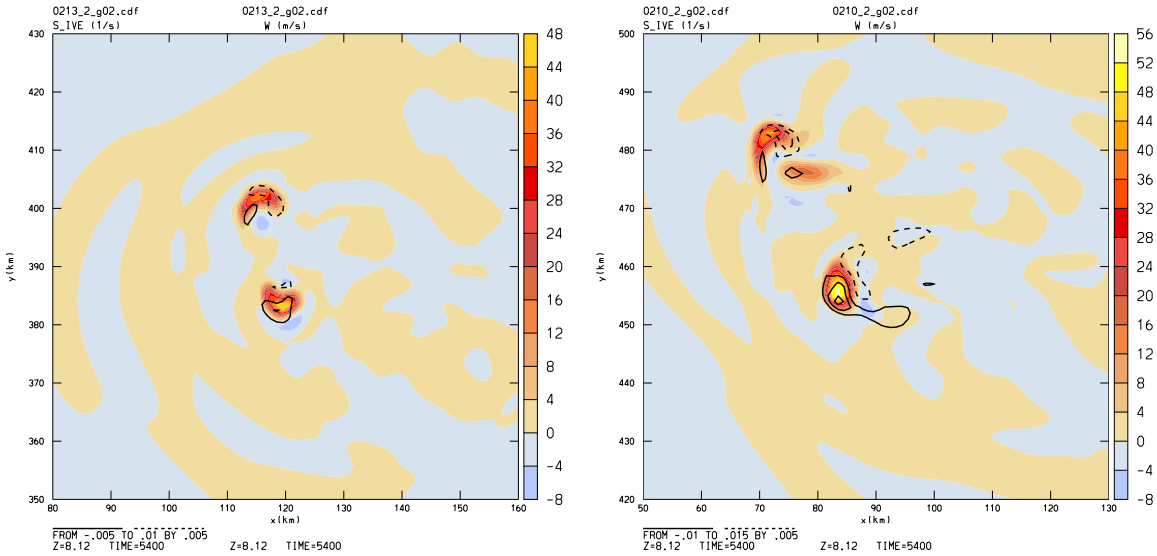

Figure 3.24: Colored contours of vertical velocity for the multicell regime (left panel) and supercell regime (right panel) at 1.5 hours. Black lines show contours of vertical relative vorticity; contour interval is 0.0005 s^{-1}. Negative contours are dashed. Horizontal slice through updrafts at altitude of 8.125 km.

Figure 3.24 shows a snapshot of vertical velocity in both multicell (left panel) and supercell (right panel) regimes. The southernmost cell in the supercell regime is a supercell, with markedly larger diameter and higher updraft strength than the other cells in both the multicell and supercell snapshots. It should be noted that the supercell regime does contain some multicells.

In summary, the above differences in the magnitude of vertical velocities, cell lifetimes and updraft diameters resulted in the supercell storm transporting more mass into the stratosphere than the multicell storm over the storm lifetime (figure 3.25).

Protected core

The higher vertical velocities, longer cell lifetimes and wider updrafts in the supercell would all contribute to less entrainment of boundary layer air in the updraft core, a phenomenon discussed by Hauf et al. (1995), Strom et al. (1999), and Skamarock et al. (2000). Figure

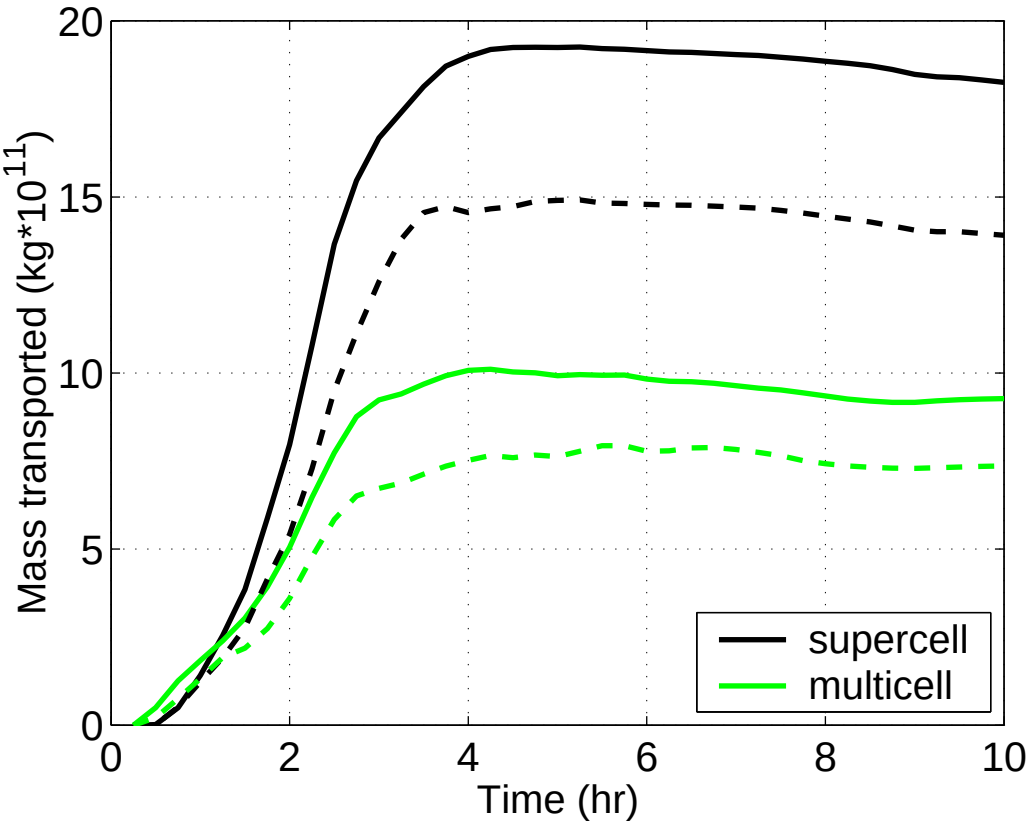

Figure 3.25: Total amount of tracer transported into the stratosphere by the supercell storm (black lines) and by the multicell storm (green lines). Solid lines show the amount of TR5 transported; dashed lines, the amount of TR4.

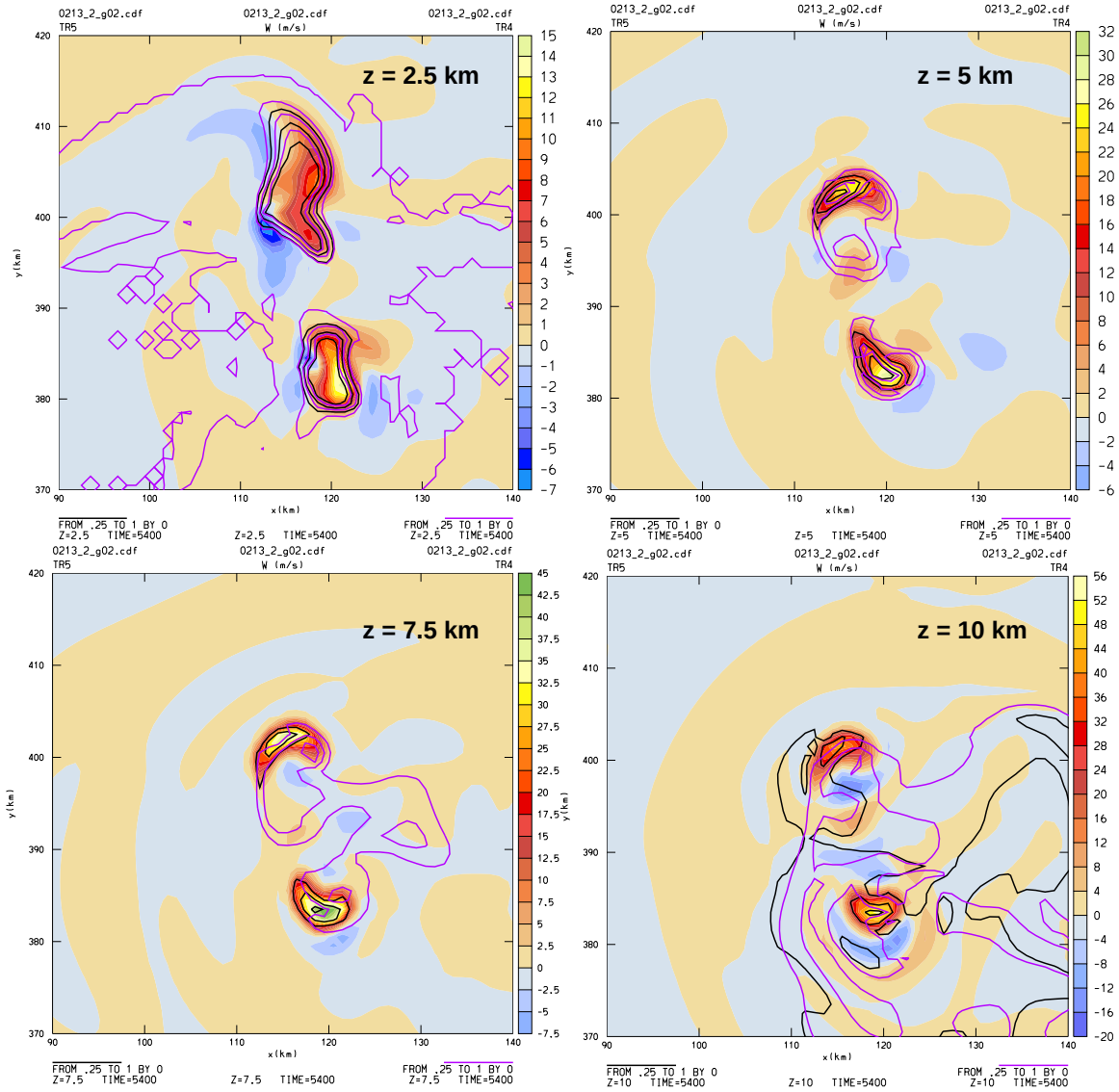

Figure 3.26: Slices through the multicell storm updrafts at 1.5 hours at the altitudes 2.5, 5, 7.5 and 10 km. The colored contours show vertical velocity. The lines overlain show the passive tracer concentrations at 0.25, 0.5, 0.75, and 1.0 kg/kg for TR5 (black) and TR4 (purple). Note the 2.5 km slice is in the TR4 layer, so the purple contours show a hole in the layer, not a peak.

3.26 shows slices through the updrafts in the multicell simulation at 1.5 hours, at 2.5, 5, 7.5 and 10 km and shows the vertical velocity in colored contours with the TR5 (black lines) and TR4 (purple lines) concentrations overlain. As would be expected, the concentrations of TR5 and TR4 are lower at 7.5 km and 10 km than in the supercell storm (figure 3.15).

Some authors (cite) have suggested that the higher rotation in the supercell updrafts also contribute to the lower detrainment. The relative vertical vorticity field is overlain on figure 3.24 (black lines) and shows that the higher vorticity in the supercell does correspond to the location of higher TR5 concentrations in figure 3.26.

3.5 Supercell storm- 13km tropopause / LNB variation

We hypothesized that having a level of neutral buoyancy closer to the tropopause would give the updrafts more energy to penetrate the tropopause thereby producing more cross-tropopause exchange. To investigate this idea, we varied the height of the tropopause (10.875 km and 12.875 km) in the idealized supercell case, while keeping the level of neutral buoyancy (LNB) fixed at approximately 11 km. For ease of discussion, we will refer to the new case, with a tropopause at 12.875 km, as the "high tropopause" case and to the original supercell storm as the "typical" case.

3.5.1 Initialization

Figure 3.27 shows the thermodynamic profile for the typical supercell case first presented and the current case with an elevated tropopause. The environmental temperature profile for the typical case is shown as a solid black line. The environmental temperature profile for the high tropopause case is shown as a dashed red line. Note that the temperature profiles are identical from the surface to 10.875 km, the level of the tropopause in the typical supercell. Therefore, the temperature profile for a parcel lifted from the surface is identical for both cases, shown in figure 3.27 as a black dashed line. The LNB is marked by an arrow for both cases. In the typical supercell case (black arrow), the LNB lies slightly above the tropopause. In the high tropopause supercell case (red arrow), the LNB lies 2 km below the tropopause.

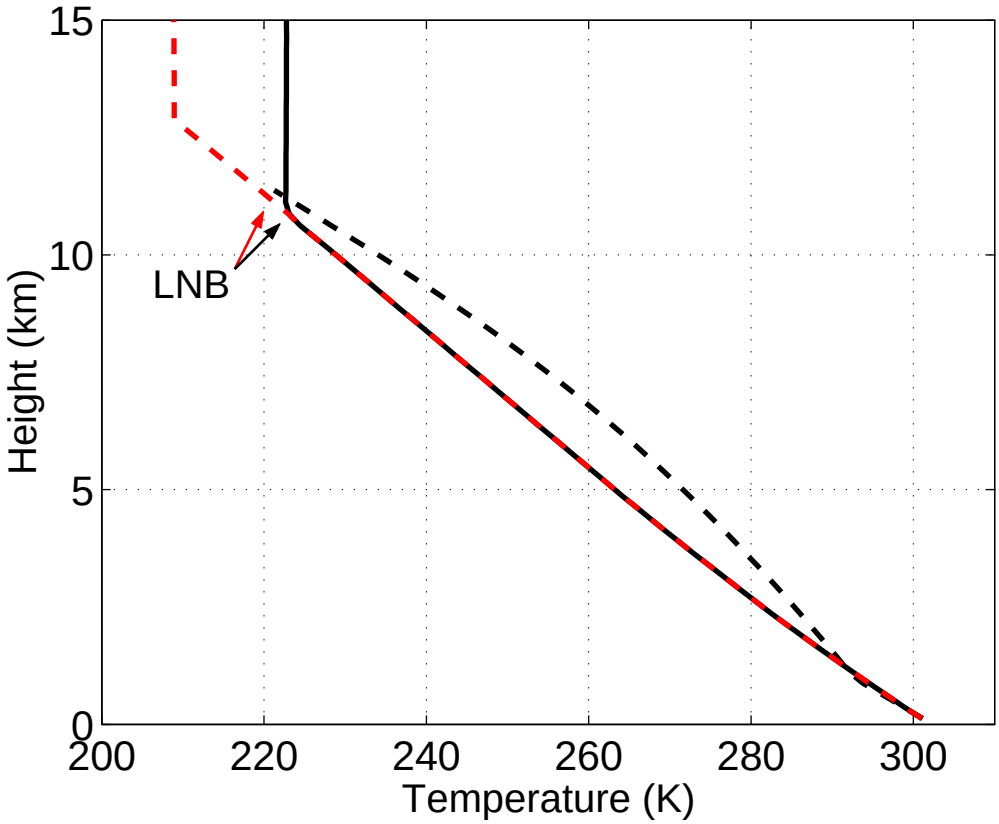

Figure 3.27: Initial temperature profile of the environment in the case with a tropopause at 10.875 km (solid black line) and of the environment in the case with the tropopause at 12.875 km (dash red line). In both cases, the temperature profile for a parcel lifted from the surface is identical (dashed black line). The level of neutral buoyancy is marked for both the high tropopause (red arrow) and typical (black arrow) cases.

Since the tropopause has been shifted upward, the stratospheric tracer TR1 now extends upward from 12.875 km and the TR2 layer has been deepened to include the region 7.375 km to 12.875 km. The tracers TR3, TR4 and TR5 are the same as in the cases already presented. The winds are identical in both supercell cases.

3.5.2 Simulation overview

After 30 minutes into the simulation, one updraft cell is evident and reaches a height of 13.75 km with maximum vertical velocity of 42 m/s at 8.875-9.375 km. The initial cell has a radius of 5 km which is the approximate radius of the subsequent updrafts in the this case. The updraft strength surpasses 50 m/s by 45 minutes and remains this strong until 2 hours into the simulation.

The eastern edge of the storm reaches the dry region at approximately 1.5 hours and the storm begins to dissipate at this time. At the time the storm encounters the dry air mass, the vertical velocity at 10.75-11.5 km has reached a storm maximum of 62 m/s. This maximum vertical velocity is slightly higher than the maximum vertical velocity in the typical case because a parcel is able to accelerate without being inhibited by the tropopause. The maximum updraft height is 15.75 km. The storm anvil, here defined as a total hydrometeor mixing ratio of greater than or equal to 0.1 g/kg, has a maximum extent of 4000 km^2 at 8.875 km at 2 hours.

3.5.3 Results

Figure 3.28 shows snapshots of an isosurface of the boundary layer tracer, TR5, with a concentration of 0.1 kg/kg. It is clear from these snapshots that significant amounts of mixing must be occurring as the material does not remain at LNB of 11 km. Starting at 1.5 hours, two main levels of outflow appear in the snapshots, one near the LNB, the other near the tropopause level of 12.875 km.

The averaged mixing ratio (figure 3.29) shows only a hint of the two outflow levels that appear in the isosurface snapshots. TR5 (blue line) is deposited almost equally throughout the depth from the LNB to the tropopause.

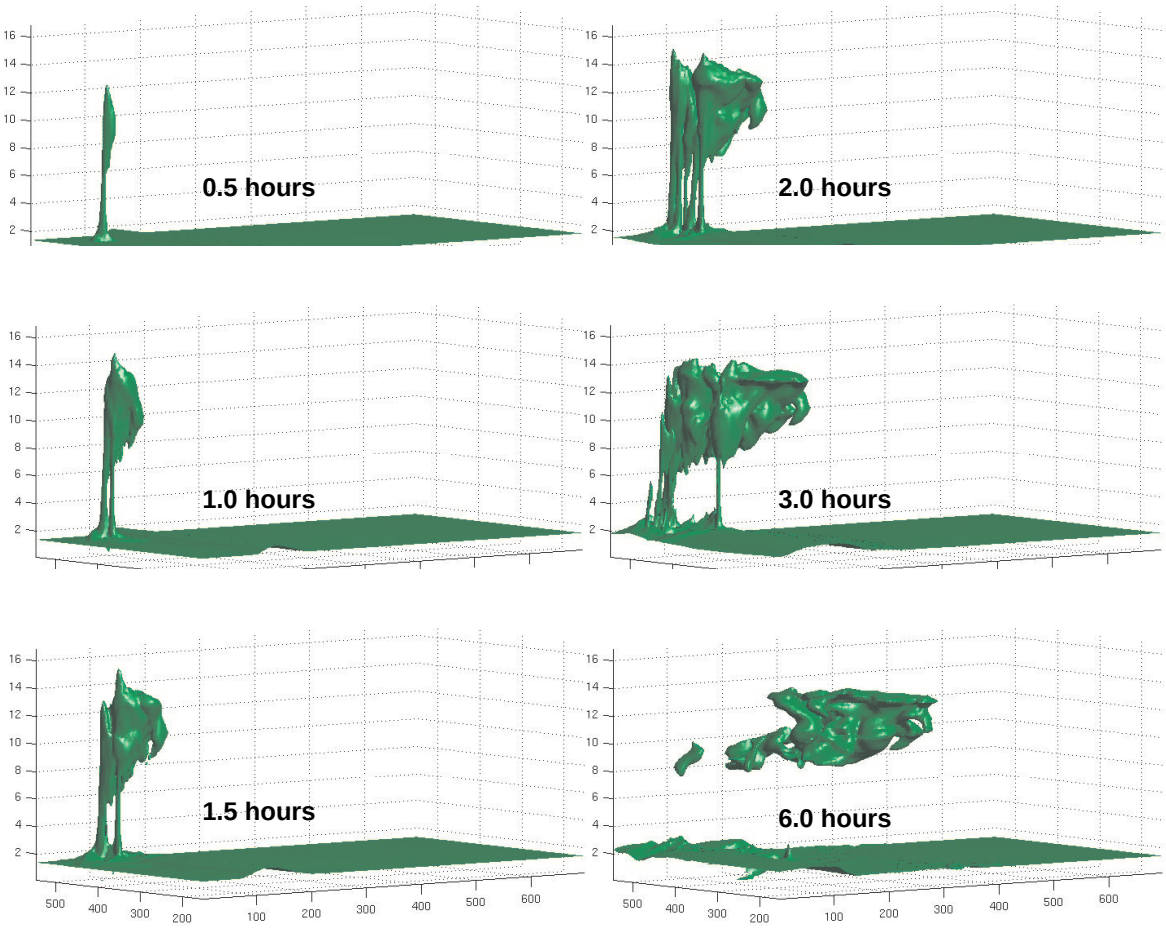

Figure 3.28: Isosurface of TR5 = 0.1 kg/kg at 0.5, 1, 1.5, 2 ,3 and 6 hours into the high tropopause supercell simulation. The portion of the model domain shown is x = 0 to 700 km, y = 150 to 550 km, and z = 0 to 17 km.

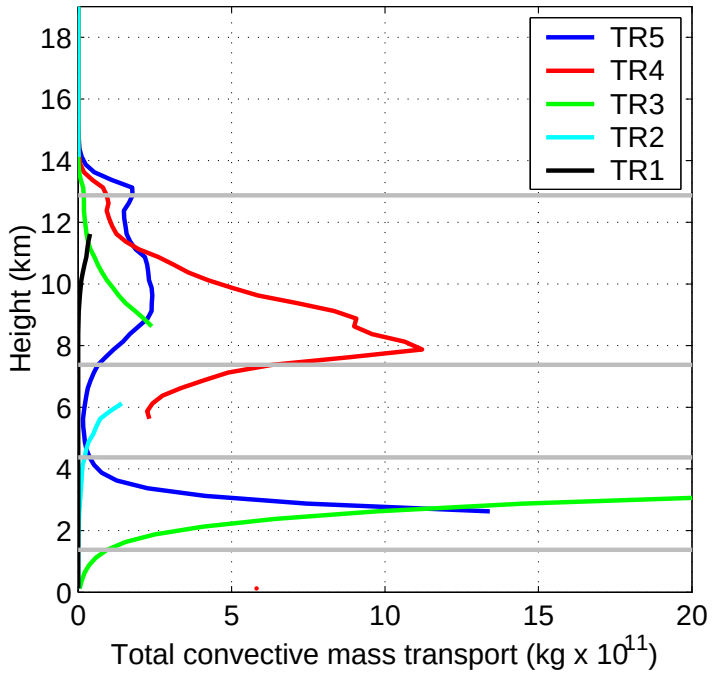

Figure 3.29: Total convective mass transport summed over entire domain at 10 hours into high tropopause supercell simulation (same as panel D, figure 3.11). TR5 is shown in blue; TR4, in red; TR3, in green; TR2, in cyan; and TR1, in black. The gray lines indicate the original locations of the tracer layers.

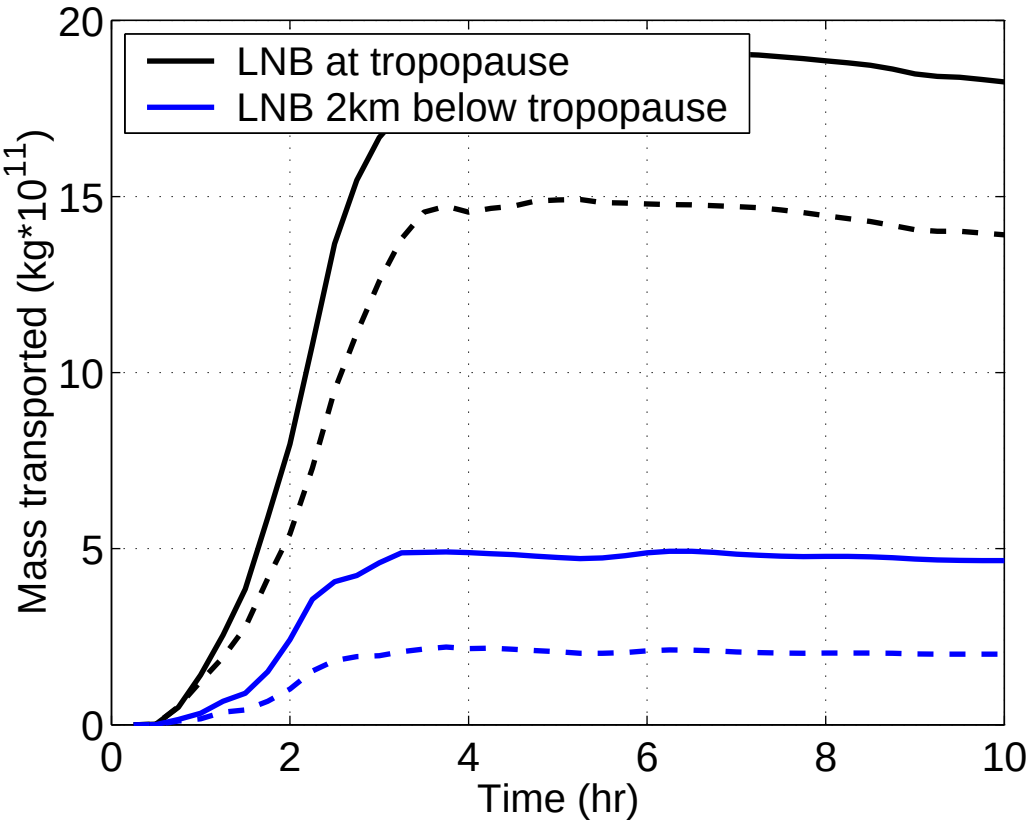

Figure 3.30: Total amount of tracer transported into the stratosphere by the "typical" supercell storm (black lines) and by the "high tropopause" supercell storm (blue lines). Solid lines show the amount of TR5 transported; dashed lines, the amount of TR4.

As expected, there is more transport into the stratosphere in the case with the LNB closest to the tropopause (figure 3.30).

3.6 STEPS storm

We have obtained observational data of an exceptionally deep convective event that occurred on July 5, 2000, at 2300Z, during the Severe Thunderstorm Electrification and Precipitation Study (STEPS) campaign (Miller and Weisman, 2002). Figure 3.31 shows a radar picture of the storm near the western Kansas-Nebraska border. Overshooting cloud tops were observed to reach 18-19km (M. Weisman, personal communication, 2001). With the undisturbed

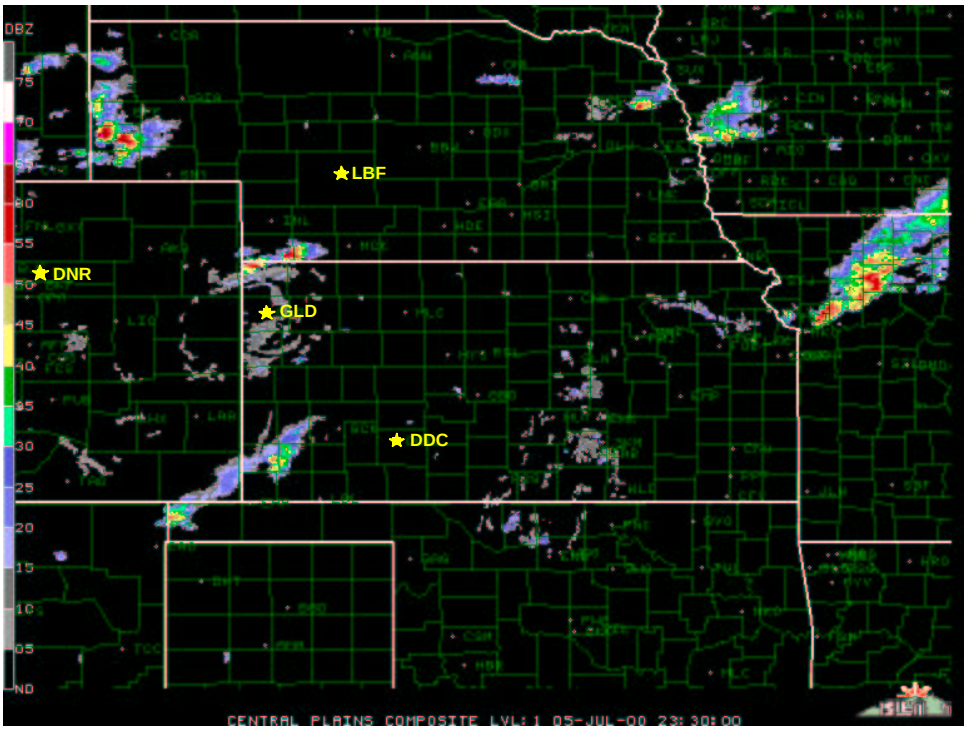

Figure 3.31: Central plains NIDS composite for July 5, 2000 at 23:30Z (from STEPS website, radar image courtesy of NCAR/RAP). Starred locations indicate soundings used to create composite for storm simulation(GLD = Goodland, KS; DNR = Denver, CO; LBF = North Platte, NE; DDC = Dodge City, KS). Storm of interest is located north of GLD, along the Kansas-Nebraska border.

tropopause at about 13.5 km and the level of neutral buoyancy at about 14.5 km, this storm was a good candidate for significant tropospheric to stratospheric transport.

3.6.1 Initialization

The STEPS case was initialized with temperature, wind, and water vapor data that were composited from soundings taken in the vicinity of the storm observations (figure 3.32). The colored lines show soundings from Goodland, KS (GLD), North Platte, NE (LBF), Dodge City, KS (DDC) and Denver, CO (DNR); these stations are labelled on the radar picture (figure 3.31). These soundings were taken at 00Z with the exception of GLD which was a specially requested sounding taken at 2029Z. The black line shows the composite

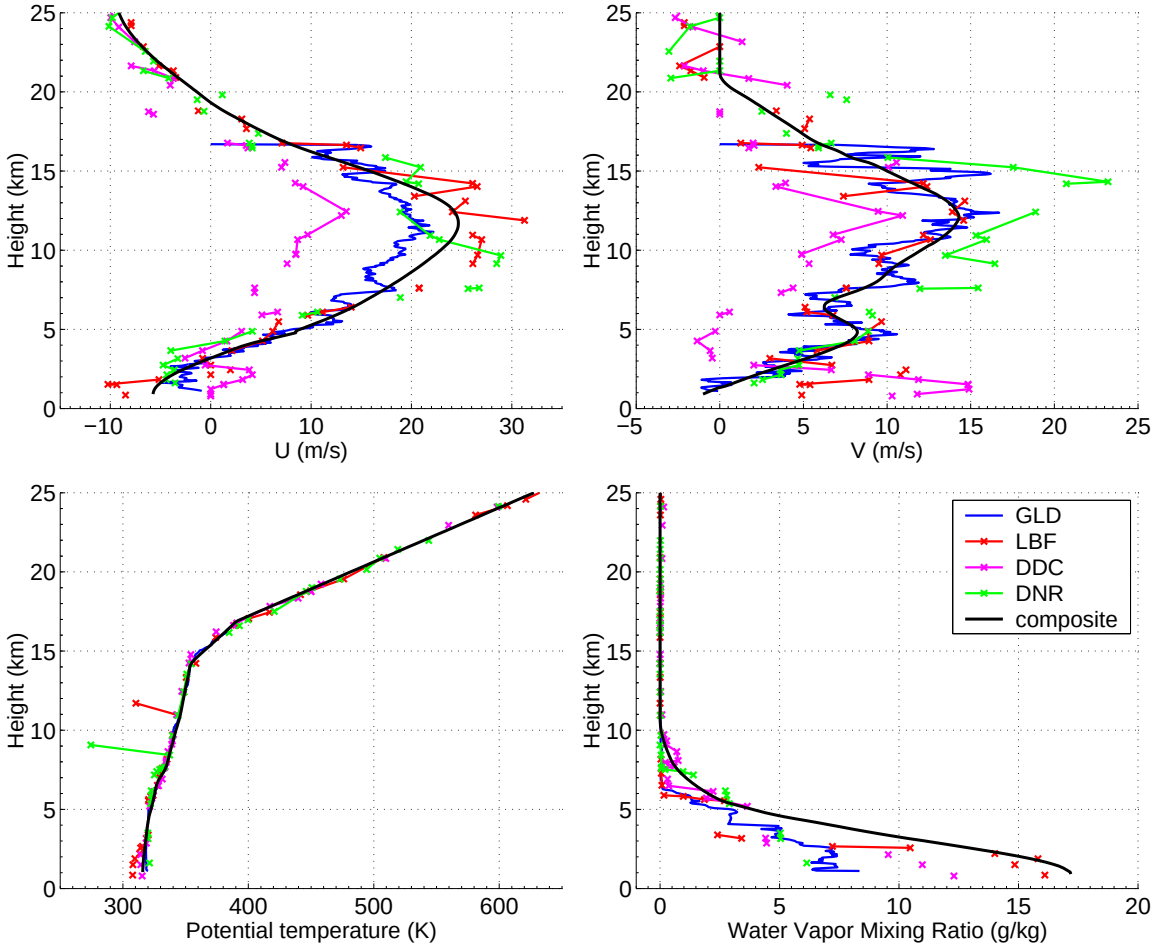

Figure 3.32: Regional soundings and composite sounding used for STEPS simulation. Colored lines from regional stations: blue line is Goodland, KS (GLD), red line is North Platte, NE (LBF), magenta line is Dodge City, KS (DDC) and green line is Denver, CO (DNR). Black line shows the composite sounding used for model initialization.

profile used to initialize the model simulation. GLD and LBF were most relevant for the storm environment, so weighted most heavily in creating the composite. The composite sounding has CAPE of 5034 J/kg and BRN of 128 which puts this case in the multicell regime. The water vapor profile near the surface was skewed toward LBF in order to obtain such high CAPE. This profile is justified because only with such high CAPE is the observed overshooting top altitude of 19 km properly simulated. Note that this case has wind shear through the entire model domain depth.

As in the high tropopause supercell case, the tracer profiles were modified so that both TR2 and TR1 go to zero at the tropopause height, 13.375 km. Because of the extraordinarily high CAPE values, this storm required a deeper and drier layer of low-level air to kill off the storm. The strong virtual temperature gradient between the air masses caused strong mixing at low levels and has artificially increased the transport amount for TR5 and decreased the transport amount for TR4. Model calculations done with the idealized supercell give an estimate for the increase in TR5 of 7% and for the decrease in TR4 of 7%. Looking at TR4 and TR5 only, the deepened dry air influx causes a 0.3×10^{11} kg increase in the total mass transport.

3.6.2 Simulation overview

After 30 minutes into the simulation, one updraft cell is evident and reaches a height of 17 km with maximum vertical velocity of 66 m/s from 11.25-12.5 km. The initial cell has a radius of 6 km, but subsequent updrafts have a radius closer to 5 km. The updraft strength surpasses 50 m/s just after 15 minutes and remains this strong until 2.5 hours into the simulation. The eastern edge of the storm reaches the dry region at approximately 1.5 hours. At the time the storm encounters the dry air mass, the vertical velocity at 13.25-13.75 km has reached a storm maximum of 88 m/s. The maximum updraft height is 19 km.

Figure 3.33 shows cross-sections of reflectivity of both the observed storm (left panel) and the simulated storm (right panel). It is difficult to match the exact cell maturity and orientation when comparing a simulated storm with a snapshot of the observed storm, but

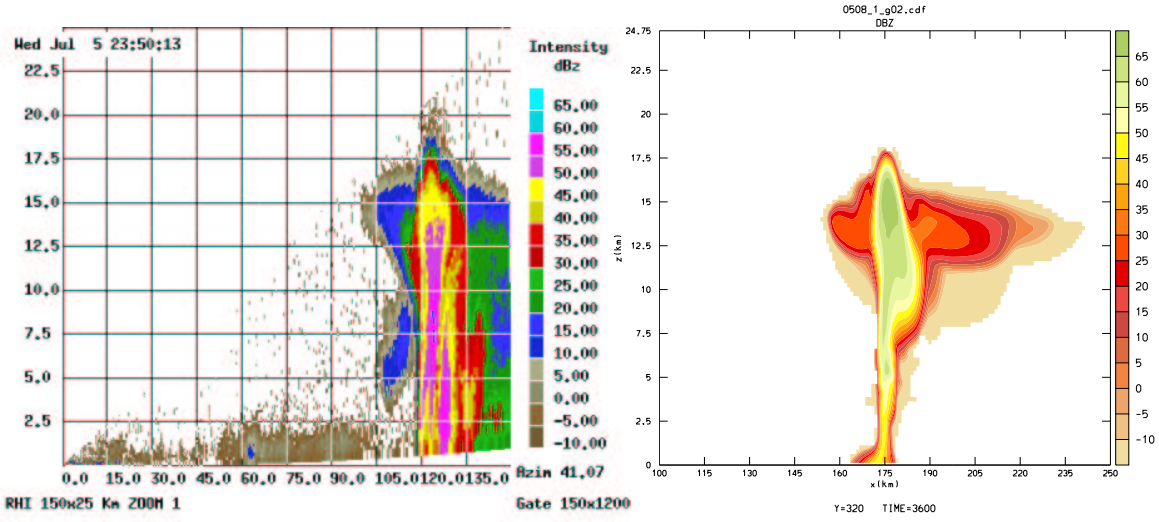

Figure 3.33: Comparison of reflectivity from observed storm (left panel) and simulated storm (right panel). Observed storm reflectivity measured by CHILL radar during STEPS campaign. Simulated storm shown at one hour.

good agreement is shown in the updraft height, updraft width, and forward anvil size. The reflectivity of the observed storm is somewhat lower than simulated, but, again, may be due to differences in the cell maturity.

The storm anvil, defined as a total hydrometeor mixing ratio of greater than or equal to 0.1 g/kg, has a maximum extent of 10000 km^2 at 13.375 km at 2 hours.

3.6.3 Results

As in the previous cases, the total convective transport above the tropopause shows the highest increase in TR5 (figure 3.34). The bimodal structure in outflow seen in the both the typical supercell case and the multicell case is seen again in the STEPS case, with one maximum above the tropopause and another a few grid steps below.

The STEPS storm initially transports more material into the stratosphere than the supercell, but the total mass falls off after approximately 5 hours (figure 3.35). The total mass transported to the stratosphere decreases in the STEPS storm due to waves propagating inward from the lateral boundaries, causing a net deflection of the Θ surfaces downward.

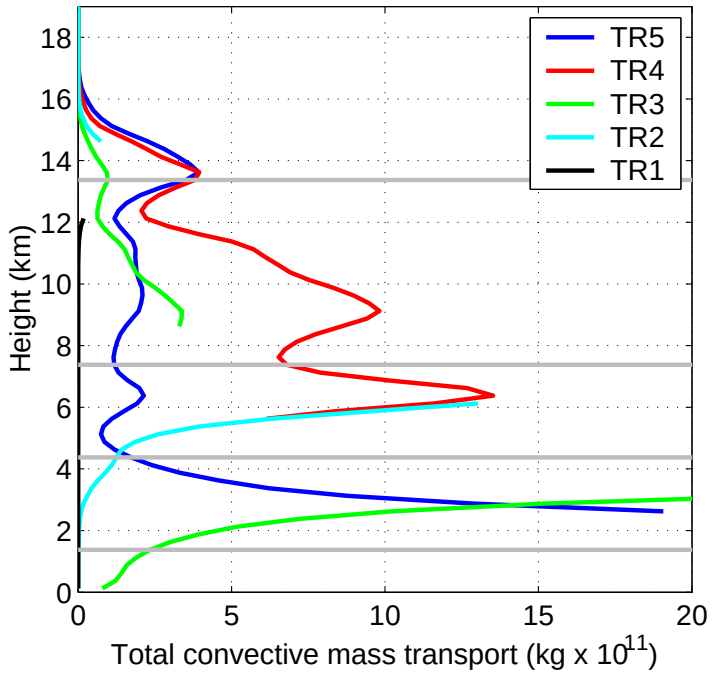

Figure 3.34: Total convective mass transport summed over entire domain at 10 hours into STEPS simulation (same as panel D, figure 3.11). TR5 is shown in blue; TR4, in red; TR3, in green; TR2, in cyan; and TR1, in black. The gray lines indicate the original locations of the tracer layers.

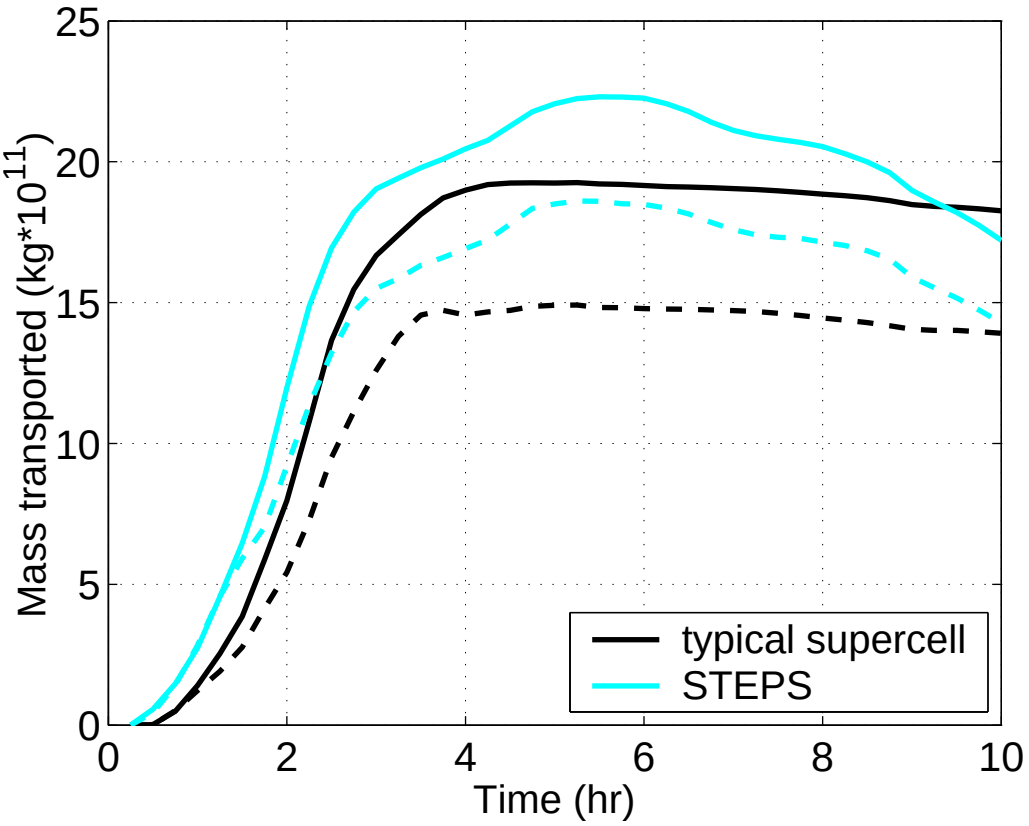

Figure 3.35: Total amount of tracer transported into the stratosphere by the "typical" supercell storm (black lines) and by the STEPS storm (cyan lines). Solid lines show the amount of TR5 transport; dashed lines, the amount of TR4.

As the theta surfaces descend, tracer mass descends as well, resulting in less mass above the tropopause $d\Theta/dz$ threshhold. The STEPS storm is very energetic; the model domain was not sufficiently large to simulate the storm correctly. While the numerical error in the STEPS simulation makes it impossible to use theresults for a quantitative measure of transport in the STEPS case, the simulation still demonstrates that irreversible injection of lower tropospheric air into the stratosphere does occur in observed midlatitude convection.

3.7 Idealized supercell storm with shear from STEPS storm

3.7.1 Initialization

The differences in both CAPE and shear made direct comparison of the STEPS case with the idealized storms difficult. In order to isolate the results of shear on the storm transport, we ran a simulation that had shear identical to the STEPS case, but with a thermodynamic profile identical to the supercell storm with the elevated tropopause. Note that due to the reduced CAPE, we were also able to reduce the problem of contamination due to the deepened dry air mass that occurred in the STEPS case. For ease of discussion, we will call this case with the idealized temperature profile with STEPS shear the "modified STEPS" case.

Figure 3.36 shows hodographs of the low level wind shear for both the idealized supercell storm (left panel) and the modified STEPS storm (right panel). The modified STEPS case has a BRN of 66 which gives this storm a multicell classification. A multicell classification means that in comparing the modified STEPS storm with the high tropopause supercell, we will be comparing not only the effects of shear, but also the storm classification difference. However, the modified STEPS storm seems to have some characteristics of a supercell storm, as will be discussed in the following sections.

The tracer profiles are identical to the high tropopause supercell case.

3.7.2 Simulation overview

After 30 minutes into the simulation, one updraft cell is evident and reaches a height of 13.5 km with maximum vertical velocity of 40 m/s at 9.5 km. The initial cell has a radius of

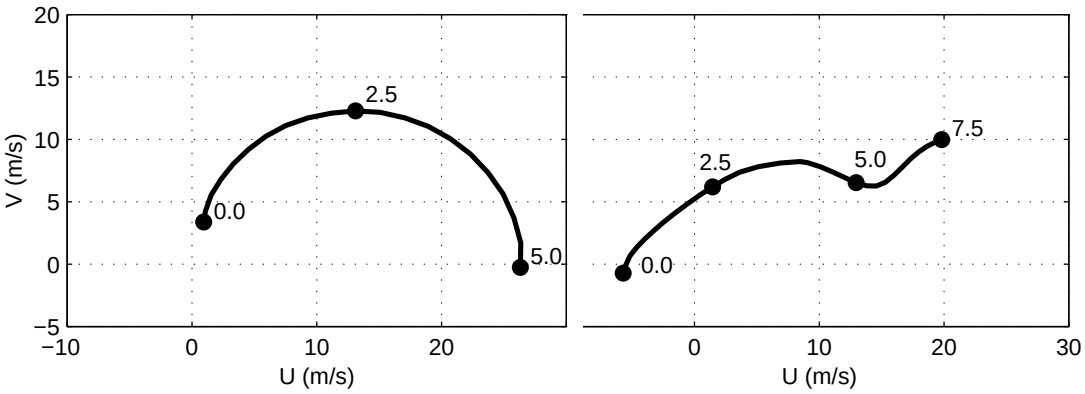

Figure 3.36: Hodographs showing the low level wind shear profiles in the supercell storm (left panel) and the modified STEPS storm (right panel). Numbers at points on lines give altitude in km. The modified STEPS case has shear to 20 km.

5 km, the approximate size of subsequent cells. The updraft strength surpasses 50 m/s at 50 minutes and remains this strong until almost 2.5 hours into the simulation. Just after 2 hours, the vertical velocity at 10.5-11.5 km has reached a storm maximum of 58 m/s. The updraft reaches a maximum height of 15.5 km. The eastern edge of the storm reaches the dry region at approximately 1.5 hours.

Although the modified STEPS case has the same CAPE and dry air influx as the high tropopause supercell case, the modified STEPS case takes longer to dissipate. The modified STEPS storm has an eastward translation rate that is less than half that of the high tropopause supercell storm and therefore takes longer to fully propagate into the dry air zone. This slower propagation allows sections of the modified STEPS storm longer access to the higher CAPE environment. The results show the modified STEPS storm has higher transport into the stratosphere than the high tropopause supercell storm at times before reaching the dry air, however, so this difference in dissipation speed does not strongly distort the findings.

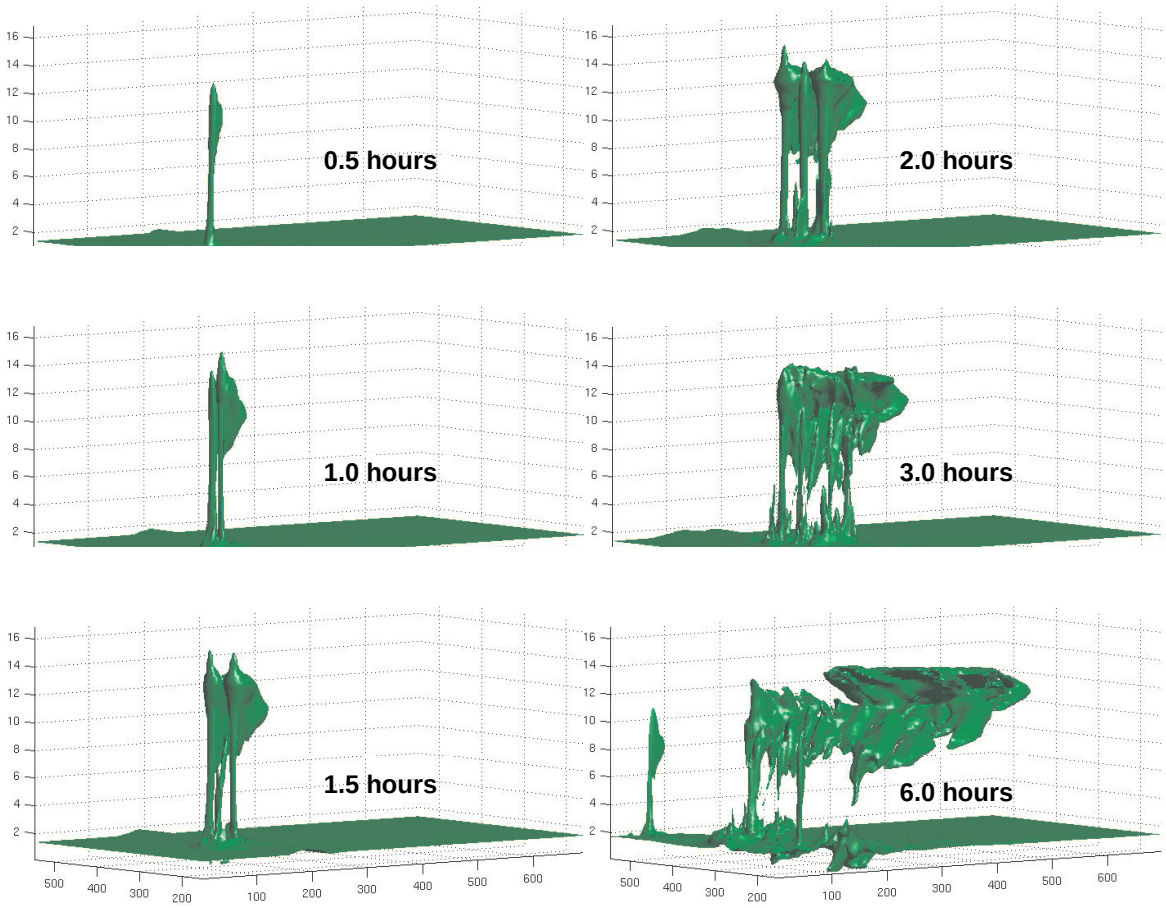

Figure 3.37: Isosurface of TR5 = 0.1 kg/kg at 0.5, 1, 1.5, 2 ,3 and 6 hours into the modified STEPS simulation. The portion of the model domain shown is x = 0 to 700 km, y = 150 to 550 km, and z = 0 to 17 km.

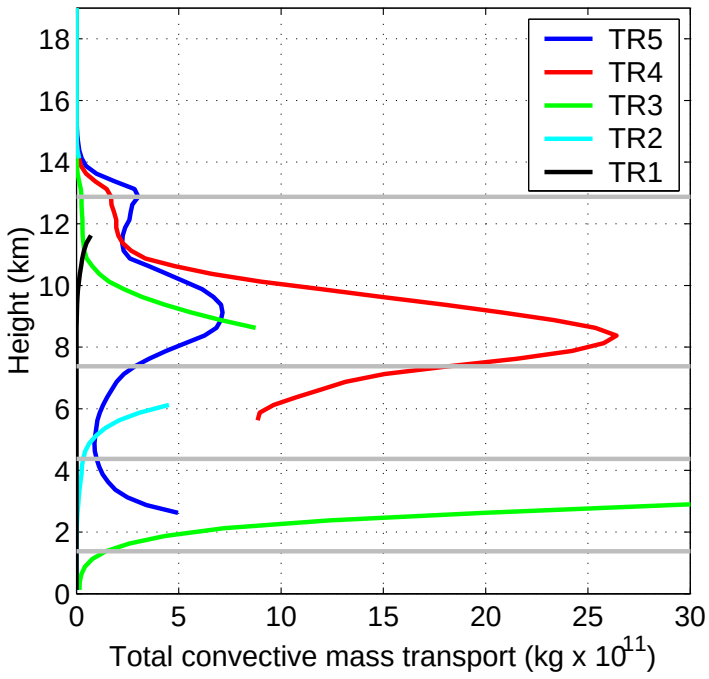

Figure 3.38: Total convective mass transport summed over entire domain at 10 hours into modified STEPS simulation (same as panel D, figure 3.11). TR5 is shown in blue; TR4, in red; TR3, in green; TR2, in cyan; and TR1, in black. The gray lines indicate the original locations of the tracer layers. Note that this figure has a different x-axis than previous convective mass transport plots.

3.7.3 Results

Figure 3.37 shows snapshots of an isosurface of the boundary layer tracer, TR5, with a concentration of 0.1 kg/kg. The storm has well-sustained updrafts, similar to those seen in the high tropopause supercell (figure 3.28). The isosurface plots also show the longevity of this case; cells transporting boundary layer air are evident even at 6 hours into the simulation.

The plot of total convective mass transport at 10 hours (figure 3.38) is similar to the same plot of the high tropopause supercell case (figure 3.29), although the modified STEPS case more clearly shows the dual output levels in TR5 of just below the LNB and just below the tropopause. The modified STEPS case also transports more mass to the stratosphere

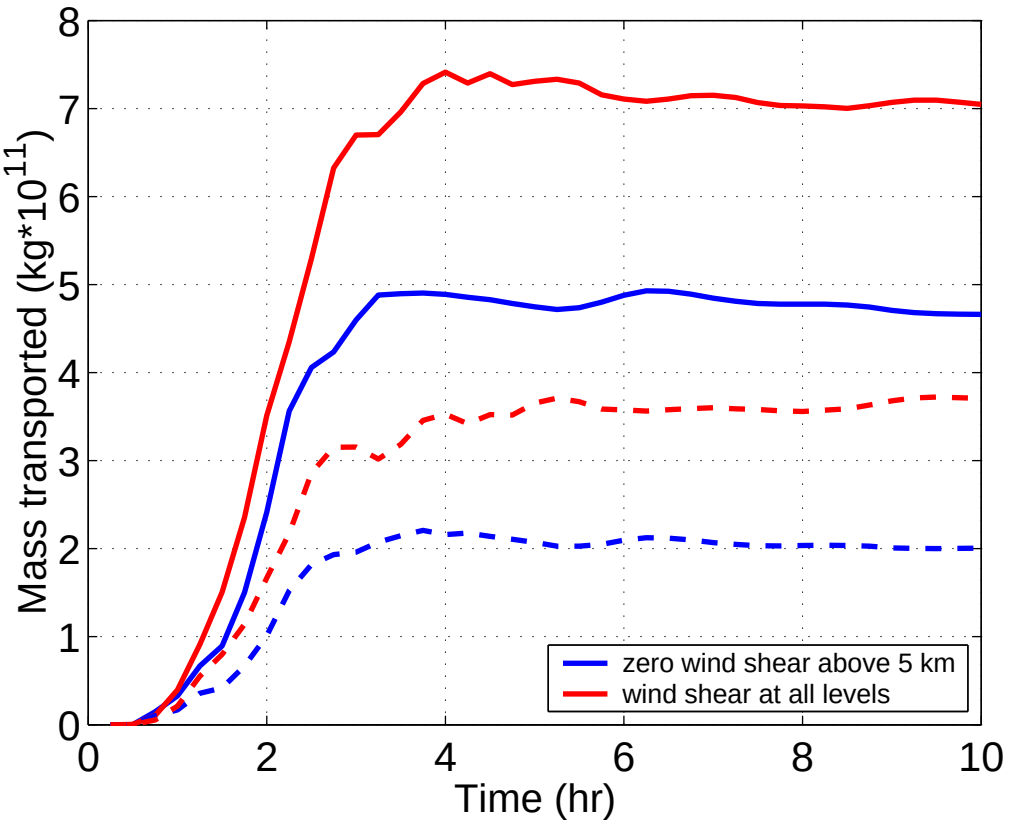

Figure 3.39: Total amount of tracer transported into the stratosphere by the high tropopause supercell storm (blue lines) and by the modified STEPS storm (red lines). Solid lines show the amount of TR5 transported; dashed lines, the amount of TR4.

(figure 3.39). This increase in transport is most likely due to increased mixing in the lower stratosphere.

The back trajectories (figure 3.40) show that mixing is a much more important process in the deposition of tracer above the tropopause than in the previous lower tropopause cases. Figure 3.40 shows a sampling of back trajectories (right panel) from a section of the tracer plume that has a minimum 0.1 kg/kg concentration of TR3, TR4 and TR5 (left panel) at 13.125 km, one model grid step above the unperturbed tropopause. The back trajectories are shown from above; the color of the trajectory shows the origination altitude. In comparison with the back trajectory analysis of the supercell storm (figure

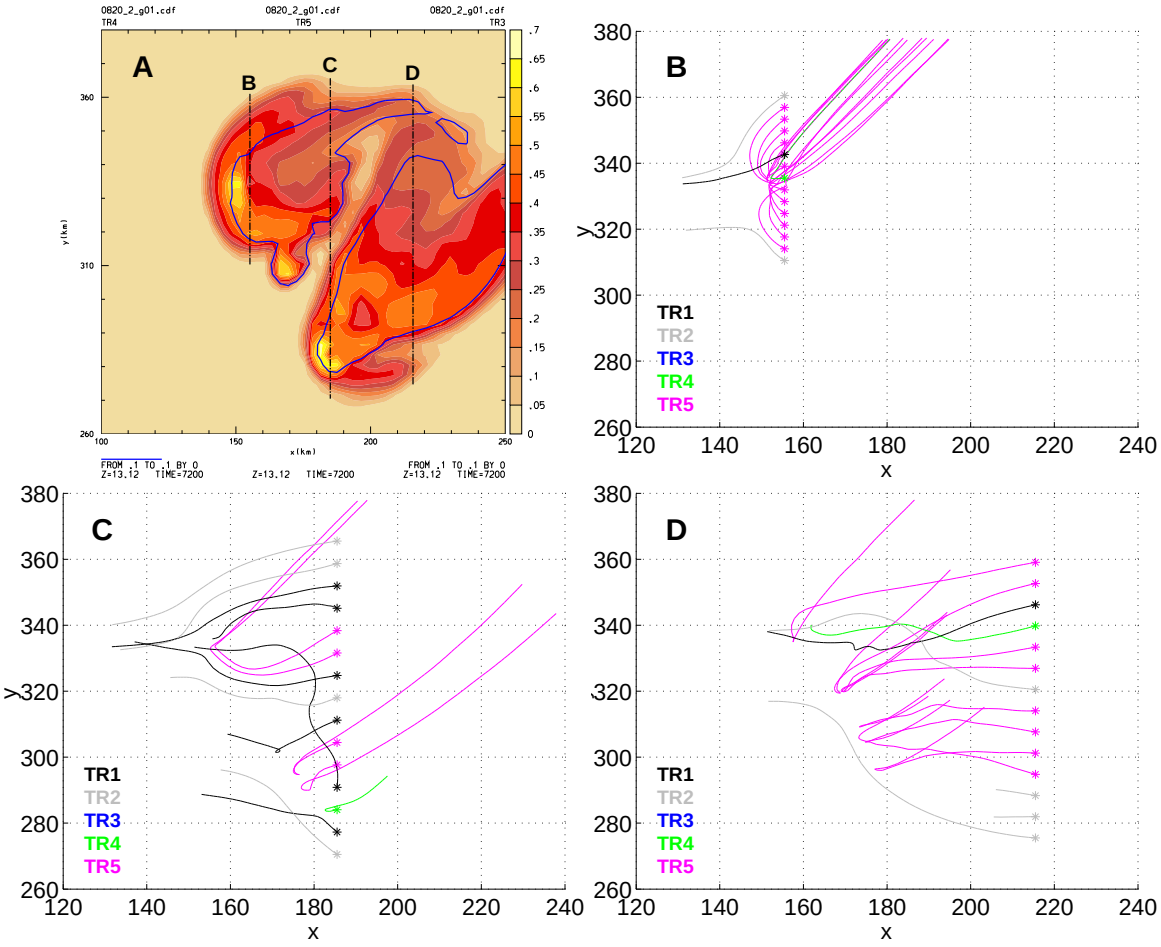

Figure 3.40: Panel A: colored contours show the TR5 tracer plume with contour intervals of 0.05 kg/kg at 13.125 km, 2 hours into the simulation. TR4 = 0.1 kg/kg is shown by the blue line and TR3 = 0.1 kg/kg is shown by the white line. The black dash-dot lines show the starting locations of the back trajectories show in the panels B (left line), C (middle line) and D (right line). Panels B-D: back trajectories computed for parcels starting at starred locations. Color of trajectory indicates origination layer. Black indicates stratosphere (> 10.875 km), gray indicates TR2 layer (7.375 to 10.875 km), blue indicates TR3 layer (4.375 to 7.375 km), green indicates TR4 layer (1.375 to 4.375 km) and magenta indicates TR5 layer (surface to 1.375 km).

3.14), many more parcels above the tropopause in the modified STEPS case originated in the stratosphere or in the TR2 layer. Any lower tropospheric tracers that exist in these parcels were introduced through mixing, most likely in the region of the overshooting tops.

The higher mixing due to the introduction of upper level shear can also be shown by looking at the amount of tracer that is transported to heights above the LNB. Lofted parcels will only settle at altitudes above the LNB if they have been mixed with warmer parcels. Figure 3.41 shows the percentage of the TR5 mass that has been transported above 6 km that has also been transported above the LNB (gray columns). This percentage is highest for the modified STEPS storm (supercell with upper level shear) because of the increased mixing due to the addition of upper level shear.

Figure 3.42 shows slices through the updrafts at 1 hour, at 2.5, 5, 7.5, 10, 12.5 and 15 km and shows the vertical velocity in colored contours with the TR5 (black lines) and TR4 (purple lines) concentrations overlain. The concentrations of TR5 in the updrafts are comparable to the concentrations of TR5 in the updrafts of the typical supercell (figure 3.15), and even higher than the typical supercell at 10 km, a not unlikely finding because in the typical case the barrier of the tropopause is a factor at 10 km, while in the modified STEPS case the tropopause is much higher. It does seem, however, that shear in the upper tropopause does not cause significant detrainment of the updraft cells.

Upper level wind shear

Wang and Prinn (1998) used a 2-D model to investigate the effects of wind shear variation on mass transport in tropical maritime convection. Their study concentrated on wind variation above the tropopause to mimic the various phases of the QBO. They found that the pattern of wind shear in the vicinity of the tropopause plays a significant role in controlling the development of deep convective clouds. Moderate shear across the tropopause favors transport. The U and V wind profiles for the modified STEPS storm simulation (figure 3.43) have profiles like the "moderate" shear profile discussed in Wang and Prinn (1998). Strong shear enhanced turbulent mixing, but inhibited the vertical development of convective turrets, thereby reducing overall transport.

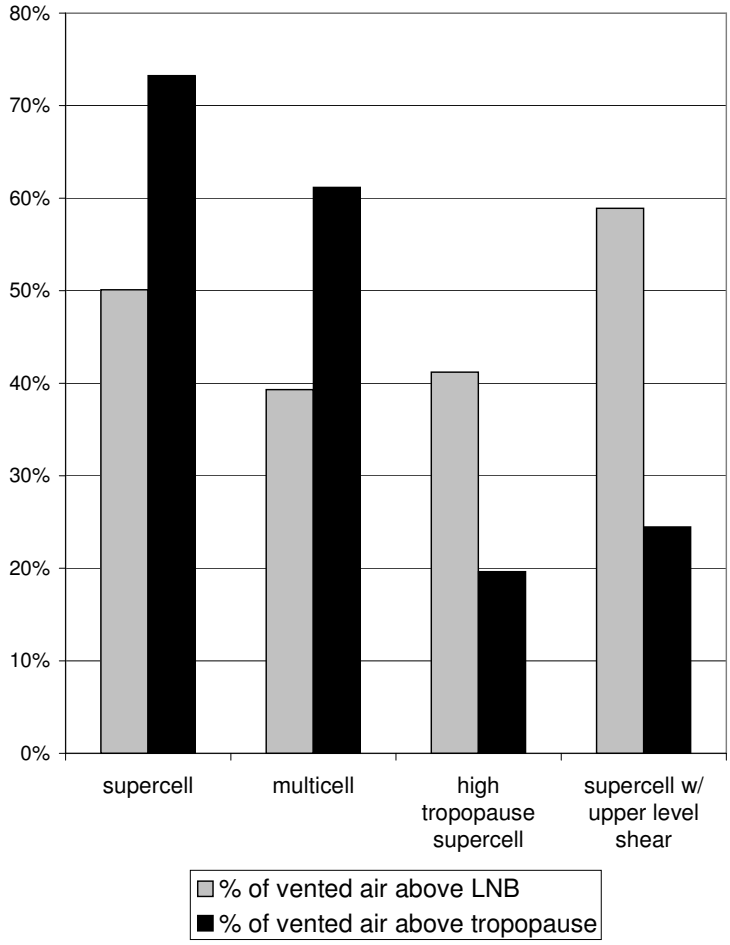

Figure 3.41: Percentage of the TR5 mass that has been transported above 6 km that has also been transported above the LNB (gray columns) and above the tropopause (black columns) for each of the idealized storms.

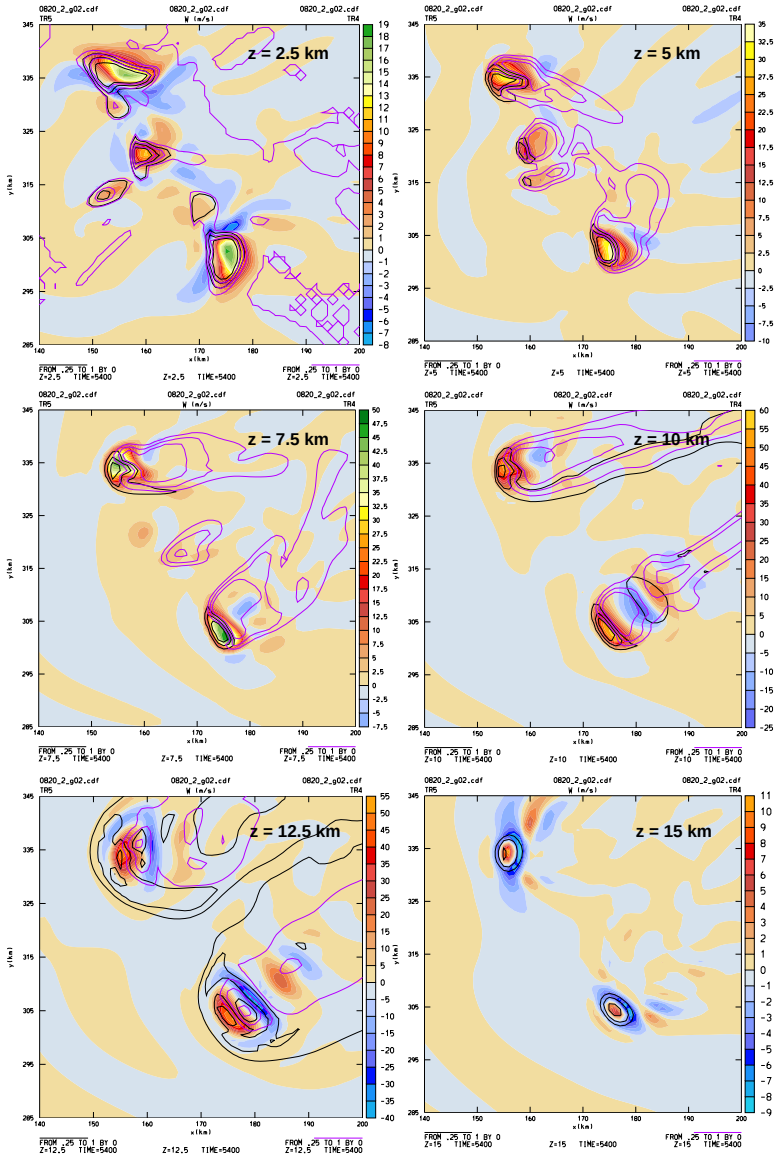

Figure 3.42: Slices through the storm updrafts at 1 hour at the altitudes 2.5, 5, 7.5, 10, 12.5 and 15 km. The colored contours show vertical velocity. The lines overlain show the passive tracer concentrations at 0.25, 0.5, 0.75, and 1.0 kg/kg for TR5 (black) and TR4 (purple). Note the 2.5 km slice is in the TR4 layer, so the contours show a hole in the layer, not a peak.

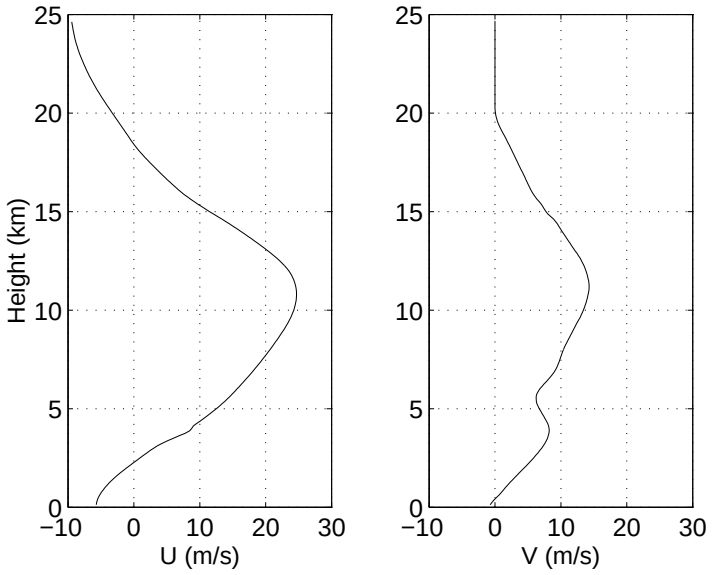

Figure 3.43: Wind shear profiles for the modified STEPS storm.

Wang and Prinn (1998) also observed that the vertical transport of boundary layer tracer to the middle and upper troposphere occurred in the early stages of the cloud development, while transport from the upper troposphere to the lower stratsophere happened in later stages. They found this later transport to be primarily horizontal with only small vertical components. Our results are quite different, with strong vertical motion injecting boundary layer air directly into the stratosphere. This difference is due to the large differences between CAPE profiles in the midlatitudes and tropics. This difference in CAPE is very important and limits direct application of our work to the tropical tracer transport problem.

Chapter 4

SUMMARY AND CONCLUSIONS

4.1 Overall objectives

Various studies both observational (e.g. Poulida et al. (1996) and Strom et al. (1999)) and modeling studies (e.g. Stenchikov et al. (1996) and Wang (2003)) have suggested that midlatitude convection may be a mechanism by which lower tropospheric gases can be injected into the lowermost stratosphere. This study is the first to use three-dimensional modeling to look at not only the amount injected above a dynamic tropopause, as opposed to a flat surface, but also the long term evolution of the injected air parcels. By running five different storm cases, this study has also begun the investigation into what parameters most affect the magnitude of convective transport.

4.2 Simulation summary

4.2.1 Transport into the stratosphere

Several factors affecting the transport of tracers into the stratosphere by midlatitude convection were tested in this study. The total transport of boundary layer and lower tropospheric tracers into the stratosphere in the five cases is summarized in figure 4.1. Our study included four idealized storms (typical supercell, high tropopause supercell, multicell, modified STEPS) and one observed storm (STEPS).

Weisman and Klemp (1986) were able to capture the variability of midlatitude storm strength and types by varying only the thermodynamic structure and low level wind shear. These idealized profiles of wind and temperature have been used successfully by subsequent authors and were therefore chosen as a basis for our idealized cases. The typical supercell storm (Weisman and Klemp (1986), Case B) served as our control storm.

By using the same thermodynamic profile and modifying the wind shear profile (Weis-

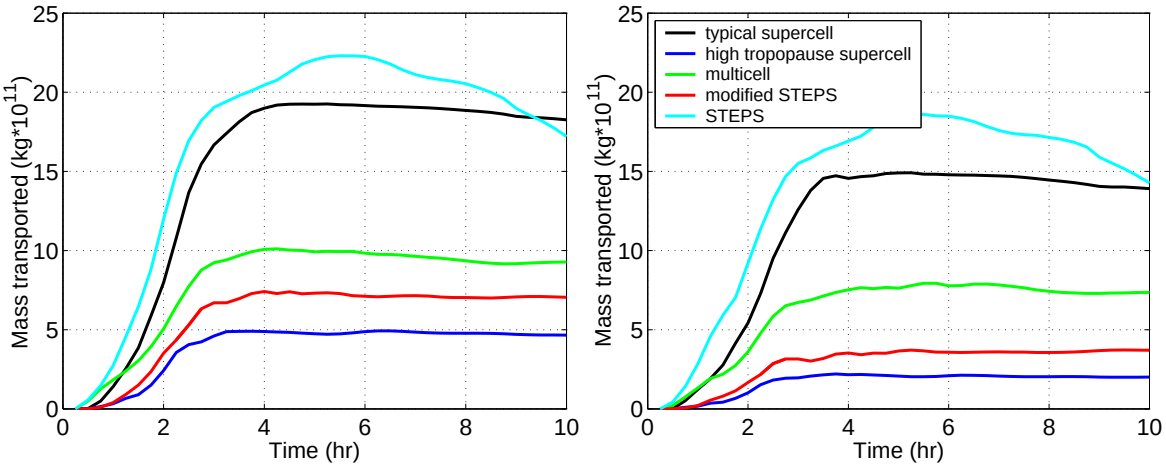

Figure 4.1: Total amount of TR5 (left panel) and TR4 (right panel) transported into the stratosphere for each of the five simulations.

man and Klemp (1986), Case A), we simulated a typical multicell to compare the effect of storm classification on tracer transport. The typical supercell storm (black lines) transports more than the typical multicell storm (green lines) because supercell updrafts have higher sustained vertical velocities, larger diameters and longer lifetimes than the multicell updrafts.

In order to examine a less idealized case, we simulated a storm observed during the STEPS campaign (light blue lines). As described in the preceding chapter, the simulated storm compared well with observed parameters such as maximum vertical velocity and reflectivity. The STEPS storm confirms that the strong cross-tropopause transport seen in the typical supercell case is not outside the bounds of reality.

This study found that the level of neutral buoyancy (LNB) in relation to the tropopause is very important in determining cross-tropopause transport. A storm with a LNB above the tropopause deposits more material in the stratosphere than a storm with a LNB below the tropopause. Interestingly, even with a LNB 2 km below the tropopause, as in the high tropopause supercell case (dark blue lines), some cross-tropopause transport does take place.

	typical supercell	multicell	STEPS	high tropopause supercell	modified STEPS
TR5 (0-1 km)	18.3	9.3	17.2	4.7	7.0
TR4 (1-4 km)	13.9	7.4	14.3	2.0	3.7
TR3 (4-7 km)	2.8	2.2	3.6	0.4	0.5

Table 4.1: Total transport of tropospheric tracers into the stratosphere at 10 hours into the simulations. All totals given in 10^{11} kg.

The preceding idealized cases (typical supercell, multicell and high tropopause supercell storms) were run with zero wind shear above 5 km. In order to investigate the effects of upper level wind shear, the vertical wind shear profile from the STEPS storm was combined with the thermodynamic profile from the high tropopause supercell. This new case, labelled the modified STEPS case (red lines), transported more mass to the stratosphere than the case with no shear (dark blue lines). This increase in transport was due to the increased turbulent mixing in the stratosphere. Unfortunately, in the study of the variation of upper level wind shear, the variation was of an already low transport case. In retrospect, a storm case created by removing the upper level shear from the STEPS storm might provide more dramatic results.

The cases presented in this study cover only a sampling of the parameter variations that can affect the transport of gases in thunderstorms. These cases give a clear overview of many of the most important factors, but much work is still needed to better describe the parameter space.

4.2.2 Displacement of stratospheric air

Very little stratospheric air was transported into the troposphere in these simulations. Previous authors have reported a larger downward motion of the stratospheric air at anvil edge (e.g. Stenchikov et al. (1996)). These observations appear to exclusively correspond to squall lines. It is reasonable to expect a larger downward deflection of stratospheric air

associated with mass compensation in a two-dimensional structure like a squall line where stratospheric air displaced by the anvil is mostly constrained to two dimensions instead of a shield anvil where air can descend in all directions.

4.3 Chemical transport

The idealized model of passive transport used in this study can be applied to several chemicals to give an estimate of maximum concentration increases in the upper troposphere and lower stratosphere. Two frequently measured chemicals with a boundary layer source and a lifetime long enough that they can be considered passive in convective transport are carbon monoxide (CO) and radon. It is true that neither chemical is confined solely to the lower troposphere in typical soundings, but the concentration of both strongly drop off above the boundary layer and have therefore been used as a proxies for boundary layer tranport in the past (e.g. Skamarock et al. (2000), Mahowald et al. (1997)).

Typical boundary layer concentrations for midlatitude continental stations are 135 ppbv for CO (Skamarock et al., 2000) and 150 pCi/m^3 for radon (Liu et al., 1984), where 1 curie (Ci) is equal to 37 billion disintegrations per second. Using these concentrations in place of the TR5 concentration of 1 kg/kg would have produced a stratosphere transport in the typical supercell storm of 2.4×10^5 kg for CO and 270 Ci for radon (250 Ci when adjusted for radioactive decay over 10 hours). Stenchikov et al. (1996) estimated an injection of 0.05 Tg CO/yr from MCC's as compared with the approximate CO production in the stratosphere of 100 Tg/yr. To reach the 0.05 Tg CO/yr level would take 200 typical supercell storms. To reach the level of 100 Tg/yr would take 2×10^5 typical supercell storms! This suggests that convective transport is not a significant source of CO in the stratosphere.

But convection may still play a significant role in the transport of other trace gases. For many chemically reactive trace gases, the atmospheric lifetimes are of the order of hours to weeks, making convection an important source of transport and crucial in defining the global distributions and chemical effects of these tracers. Halogen compounds, significant players in stratospheric ozone destruction, are examples of important trace gas. One specific example is trichloroethene (C_2HCl_3) which has a lifetime of approximately 5 days (Ko et al.,

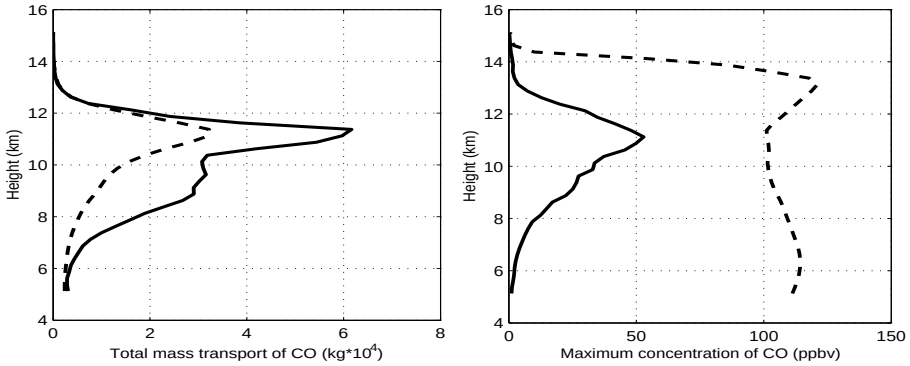

Figure 4.2: Estimated transport of CO at 2 hours (dashed line) and 10 hours (solid line) in the typical supercell storm. Left panel: total mass of CO deposited at each level. Right panel: maximum concentration of CO at each level.

2003). Trichloroethene has an industrial source which suggests that the local boundary layer concentrations could be high leading to a significant source of chlorine injection.

As mentioned by Stenchikov et al. (1996), transport (and impact) estimates are highly uncertain due to the lack of a stratosphere-penetrating storm climatology. There has been some discussion about creating such a climatology using the International Satellite Cloud Climatology Project data , but nothing is available at this time. While soundings are only a snapshot of a region and not necessarily a good predictor of LNB or even of storm activity (Rasmussen and Blanchard, 1998), an observed anvil cloud is a record of the actual region of mass divergence.

Validating model results with available observations is a problem. In-situ measurements are sparse, both temporally and spatially. A problem with many of the existing field campaigns is that while high altitude measurements of various tracers were made, the location of the perturbed tropopause is unclear; so that it is not possible to estimate the irreversible transport into the stratosphere. And, in many cases, boundary layer observations are not available.

Figure 4.2 shows the mass transport (left panel) and maximum concentration (right panel) in the upper troposphere/lower stratosphere for CO after 10 hours of simulation time for the typical supercell storm. Authors such as Hauf et al. (1995), Poulida et al. (1996)

and Strom et al. (1999) have observed anvil concentrations over 100 ppbv in observational studies. Notice that the level of maximum concentration descends about 2 km after the convection has died out, demonstrating the usefulness of a study like this that can look at the long term evolution of the tracer profile over the entire lifetime of the storm.

4.3.1 Transport parameterizations

Many parameterizations of transport in global chemical transport models are based on simple storm parameters like peak vertical velocity or total precipitation. Clearly, peak vertical velocity is an inappropriate measure as the peak vertical velocities in the supercell and multicell storms are nearly identical, but the persistence of the peak vertical velocities vary greatly.

As an example of a simple indicator of transport magnitude, the cumulative surface precipitation was plotted for each case (figure 4.3). The total precipitation for the STEPS storm and both the high and typical supercell storms were very similar, but the storms had very different stratospheric transport amounts, making surface precipitation a poor indicator of cross-tropopause transport.

Precipitation appears to be more useful as an indicator of boundary layer venting. Figure 4.4 shows the total amount of TR5 transported above 6 km (left panel) and the ratio of total TR5 transported to the cumulative precipitation (right panel) for each storm simulated. The ratio is approximately 2000 for all storms, especially during the most active stage of 1 to 2 hours. The storm dissipation varies amoung cases after the dry air mass is encountered, so the ratio is less fixed after 2 hours. Notice also that the ratio is not plotted until 30 minutes into simulation time; some cases did not produce significant precipitation until this time.

The report on a recent meeting concerning convective chemical transport (Yano et al., 2003) stated that "a standard method for parameterizing the convective transport processes in current global models is based on the mass-flux formulation, in which these transport processes are represented by an ensemble of vertical mass fluxes at subgrid scales." This meeting recognized the need for more accurate mass fluxes, based on high-resolution data from observations or modeling. Studies such as contained in this work can provide such

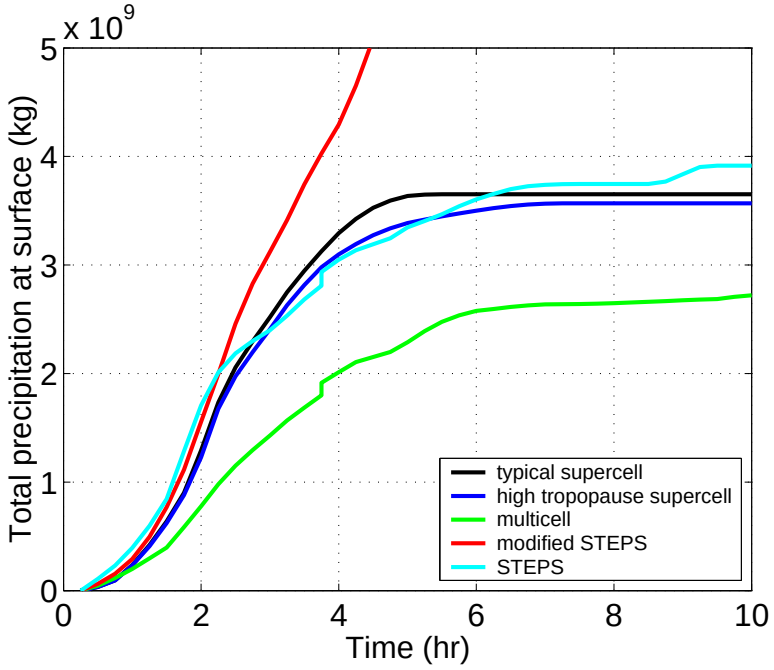

Figure 4.3: Cumulative surface precipitation for each studied case. Precipitation was calculated by summing mixing ratios of rain, snow and hail.

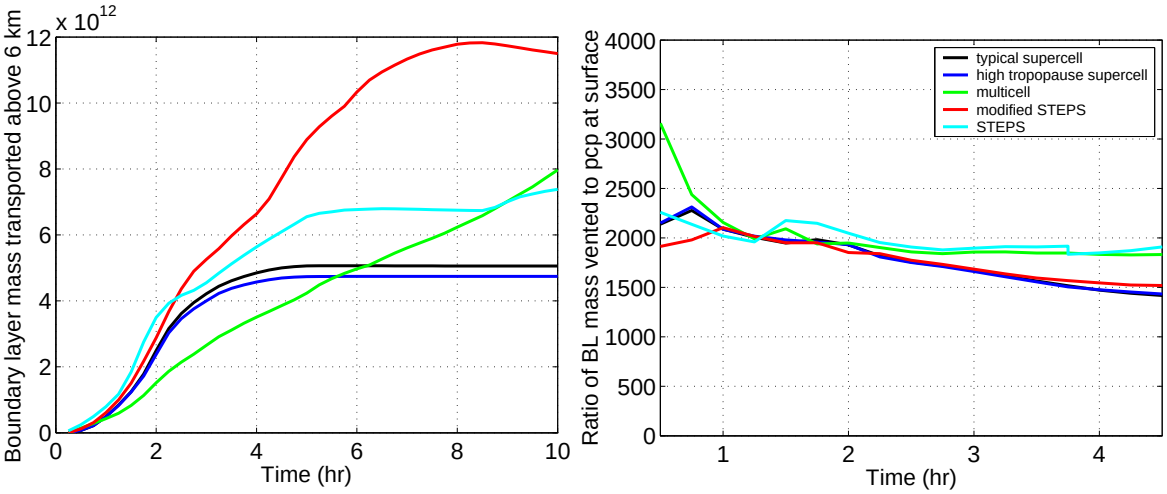

Figure 4.4: Left panel: total amount of boundary layer tracer (TR5) transported above 6 km. Right panel: ratio of boundary layer tracer mass above 6 km to the cumulative surface precipitation (figure 4.3).

high resolution data. Properly capturing convective processes in global models is difficult since productive updrafts are well below the resolved scale. Jacob et al. (1997) found in an intercomparison of different global transport models that the upper-tropospheric variability of boundary layer tracers was not captured. Our study suggests that mass flux profiles may have a simple, possibly linear, relationship with storm strength (CAPE) in the absence of a stability boundary. But further study must be done in order to properly modify mass flux profiles to reflect the more complicated relationship between the level of neutral buoyancy and tropopause location.

BIBLIOGRAPHY

Braun, S. A. and R. A. H. Jr, 1994: The transition zone and secondary maximum of radar reflectivity behind a midlatitude squall line: results retrieved from doppler radar data. *JAS*.

Clark, T. L. and W. R. Peltier, 1977: On the evolution and stability of finite-amplitude mountain waves. *JAS*.

Danielsen, E. F., 1985: Ozone transport. in *Ozone in the free atmosphere*. Van Nostrand Reinhold Company.

Dickerson, R. R., 1987: Thunderstorms: an important mechanism in the transport of air pollutants. *Science*.

Durran, D. R., 1999: *Numerical methods for wave equations in geophysical fluid dynamics*. Springer-Verlag New York, Inc.

Durran, D. R. and J. B. Klemp, 1983: A compressible model for the simulation of moist mountain waves. *Monthly Weather Review*.

Fischer, H., M. de Reus, M. Traub, J. Williams, J. Lelieveld, J. de Gouw, C. Warneke, H. Schlager, A. Minikin, R. Scheele and P. Siegmund, 2003: Deep convective injection of boundary layer air into the lowermost stratosphere at midlatitudes. *Atmospheric Chemistry and Physics*.

Hauf, T., P. Schulte, R. Alheit and H. Schlager, 1995: Rapid vertical transport by an isolated midlatitude thunderstorm. *Journal of Geophysical Research*.

Haynes, P. H., 2002: *Encyclopedia of Atmospheric Sciences*. Chap. Turbulence and Mixing. Elsevier Science Ltd.

Hintsa, E. J., K. A. Boering, E. M. Weinstock, J. G. Anderson, B. L. Gary, L. Pfister, B. C. Daube, S. C. Wofsy, M. Lowewenstein, J. R. Podolske, J. J. Margitan and T. P. Bui, 1998: Troposphere-to-stratosphere transport in the lowermost stratosphere from measurements of H_2O, CO_2, N_2O and O_3. *Geophysical Research Letters*.

Holton, J. R., P. H. Haynes, M. E. McIntyre, A. R. Douglass, R. B. Rood and L. Pfister, 1995: Stratospheric-tropospheric exchange. *Reviews of Geophysics*.

Jacob, D. J., M. J. Prather, P. J. Rasch, R.-L. Shia and ..., 1997: Evaluation and intercomparison of global atmospheric transport models using rn-222 and other short-lived tracers. *JGR*.

Ko, M. K. W., G. Poulet (Lead Authors), D. R. Blake, O. Boucher, J. H. Burkholder, M. Chin, R. A. Cox, C. George, H.-F. Graf, J. R. Holton, D. J. Jacob, K. S. Law, M. G. Lawrence, P. M. Midgley, P. W. Seakins, D. E. Shallcross, S. E. Strahan, D. J. Wuebbles and Y. Yokouchi, 2003: *Scientific Assessment of Ozone Depletion: 2002*. Chap. 2, p. 498pp. Global Ozone Research and Monitoring Project- Report No. 47, World Meteorological Organization, Geneva, Geneva, 1 ozone depletion.

LeVeque, R. J., 1996: High-resolution conservative algorithms for advection in incompressible flow. *SIAM Journal on Numerical Analysis*.

Liu, S. C., J. R. McAfee and R. J. Cicerone, 1984: Radon 222 and tropospheric vertical transport. *JGR*.

Lu, R., C. Lin, R. Turco and A. Arakawa, 2000: Cumulus transport of chemical tracers 1) cloud-resolving model simulations. *JGR*.

Mahowald, N. M., P. J. Rasch, B. E. Eaton, S. Whittlestone and R. G. Prinn, 1997: Transport of 222radon to the remote troposphere using match and assimilated winds from ecmwf and ncep. *JGR*.

Miller, L. J. and M. L. Weisman, 2002: Comparison of radar-observed and wrf-modeled structures of two steps storms. in *21st Conference on Severe Local Storms*.

Ovarlez, J., P. van Velthoven and H. Schlager, 1999: Water vapor measurements from the troposphere to the lowermost stratosphere: some signatures of troposphere to stratosphere exchange. *Journal of Geophysical Research*.

Park, S. K. and K. K. Droegemeier, 2000: Sensitivity analysis of a 3D convective storm: Implications for varational data assimilation and forecast error. *Monthly Weather Review*.

Piani, C., D. Durran and M. Alexander, 2000: A numerical study of three-dimensional gravity waves triggered by deep tropical convection and their role in the dynamics of the QBO. *Journal of the Atmospheric Sciences*.

Poulida, O., R. R. Dickerson and A. Heymsfield, 1996: Stratosphere-troposphere exhange in a midlatitude mesoscale convective complex 1. Observations. *Journal of Geophysical Research*.

Rasmussen, E. N. and D. O. Blanchard, 1998: A baseline climatology of sounding-derived supercell and tornado forecast parameters. *Weather and Forecasting*.

Scala, J. R., M. Garstang, W.-K. Tao, K. E. Pickering, A. M. Thompson, J. Simpson, V. W. J. H. Kirchhoff, E. V. Browell, G. W. Sachse, A. L. Torres, G. L. Gregory, R. A. Rasmussen and M. A. K. Khalil, 1990: Cloud draft structure and trace gas transport. *JGR*.

Sigmond, M., J. Meloen and P. C. Siegmund, 2000: Stratosphere-troposphere exchange in an extratropical cyclone, calculated with a lagrangian method. *Ann. Geophysicae*.

Skamarock, W. C., J. G. Powers, M. Barth, J. E. Dye, T. Matejka, D. Bartels, K. Baumann, J. Stith, D. D. Parrish and G. Hubler, 2000: Numerical simulations of the July 10 Stratospheric-Tropopsheric Experieemnt: Radiation, Aerosols, and Ozone/Deep Convection Experiment convective system: Kinematics and transport. *Journal of Geophysical Research*.

Stenchikov, G., R. Dickerson, K. Pickering, W. Ellis, B. Doddridge, S. Kondragunta, O. Poulida, J. Scala and W. Tao, 1996: Stratosphere-troposphere exchange in a mid-

latitude mesoscale convective complex 2. Numerical simlulations. *Journal of Geophysical Research*.

Strom, J., H. Fischer, J. Lelieveld and F. Schroder, 1999: In situ measurements of microphysical properties and tracer gases in two cumulonimbus anvils over western Europe. *Journal of Geophysical Research*.

Tao, W.-K. and J. Simpson, 1993: Goddard Cumulus Ensemble Model. Part I: Model description. *TAO*.

Wang, C. and J. Chang, 1993: A three-dimensional numberical model of cloud dynamics, microphysics , and chemistry. 3: Redistribution of pollutants. *Journal of Geophysical Research*.

Wang, C. and R. Prinn, 1998: Impact of the horizontal wind profile on the convective transport of chemical species. *Journal of Geophysical Research*.

Wang, P. K., 2003: Moisture plumes above thunderstorm anvils and their contributions to cross-tropopause transport of water vapor in midlatitudes. *Journal of Geophysical Research*.

Weisman, M. L. and J. Klemp, 1982: The dependence of numerically simulated convective storms on vertical wind shear and buoyancy. *Monthly Weather Review*.

Weisman, M. L. and J. Klemp, 1986: *Characteristics of isolated convective systems*. Chap. 15.

Wicker, L. J. and R. B. Wilhelmson, 1995: Simulation and analysis of tornado development and decay within a three-dimensional supercell thunderstorm. *Journal of the Atmospheric Sciences*.

Yano, J.-I., L. J. Donner, Y. Yin, M. G. Lawrence, C. Mari and A. Stohl, 2003: Multidisciplinary discussion of convective chemical transport. *EOS*.

Appendix A

PARAMETERIZATION OF ICE MICROPHYSICS

The following equations were taken from Tao and Simpson (1993).

$$\frac{dq_v}{dt} = D_{q_v} + (c - e_c - e_r) + (d - s)$$

$$\overline{\rho}\frac{dq_c}{dt} = \overline{\rho}(c - e_c) - T_{q_c} + D_{q_c}$$

$$\overline{\rho}\frac{dq_r}{dt} = \frac{\partial \overline{\rho} V_r q_r}{\partial z} + \overline{\rho}(-e_r + m - f) - T_{q_r} + D_{q_r}$$

$$\overline{\rho}\frac{dq_i}{dt} = \overline{\rho}(d_i - s_i) - T_{q_i} + D_{q_i}$$

$$\overline{\rho}\frac{dq_s}{dt} = \frac{\partial \overline{\rho} V_s q_s}{\partial z} + \overline{\rho}(d_s - s_s - m_s + f_s) - T_{q_s} + D_{q_s}$$

$$\overline{\rho}\frac{dq_h}{dt} = \frac{\partial \overline{\rho} V_h q_h}{\partial z} + \overline{\rho}(d_h - s_h - m_h + f_h) - T_{q_h} + D_{q_h}$$

where q_v, q_c, q_r, q_i, q_s and q_h represent the mixing ratios of water vapor, cloud water, rain, cloud ice, snow and hail, respectively. Variables c, e_c, e_r, f, m, d and s stand for the rates of condensation, evaporation of cloud droplets, evaporation of raindrops, melting of snow and hail, deposition of ice particles and sublimation of ice particles, respectively, and $m = m_s + m_h$, and $f = f_s + f_g$. D is the subgrid-scale diffusion term. V_r, V_s and V_h are the fall speeds of rain, snow and hail, respectively.

$$\frac{d}{dt} = u\frac{\partial}{\partial x} + v\frac{\partial}{\partial y} + w\frac{\partial}{\partial z}$$

The terms $T_{q_c}, T_{q_r}, T_{q_i}, T_{q_s}$ and T_{q_h} are microphysical transfer rates between hydrometeor

species, and their sum is zero. They are defined as:

$$T_{q_c} = -(P_{sacw} + P_{raut} + P_{racw} + P_{sfw} + D_{gacw} + Q_{sacw} + Q_{gacw}) - P_{ihom} + P_{imlt} - P_{idw}$$

$$T_{q_i} = -(P_{saut} + P_{saci} + P_{raci} + P_{sfi} + D_{gaci} + W_{gaci}) + P_{ihom} - P_{imlt} + P_{idw}$$

$$T_{q_r} = Q_{sacw} + P_{raut} + P_{racw} + Q_{gacw} - (P_{iacr} + D_{gacr} + W_{gacr} + P_{sacr} + P_{gfr})$$

$$T_{q_s} = P_{saut} + P_{saci} + P_{sacw} + P_{sfw} + P_{sfi} + \delta_3 P_{raci} + \delta_3 P_{iacr} + \delta_2 P_{sacr}$$
$$- [P_{gacs} + D_{gacs} + W_{gacs} + P_{gaut} + (1 - \delta_2) P_{racs}]$$

$$T_{q_g} = (1 - \delta_3) P_{raci} + D_{gaci} + W_{gaci} + D_{gacw} + (1 - \delta_3) P_{iacr} + P_{gacs}$$

where

$$W_{gacr} = P_{wet} - D_{gacw} - W_{gaci} - W_{gacs}$$

For T $> 273.16\ ^o$K

$$P_{saut} = P_{saci} = P_{sacw} = P_{raci} = P_{iacr} = P_{sfi} = P_{sfw} = D_{gacs} = W_{gacs}$$
$$= D_{gacw} = D_{gacr} = P_{gwet} = P_{racs} = P_{sacr} = P_{gfr} = P_{gaut} = P_{imlt} = 0$$

For T $< 273.16\ ^o$K

$$Q_{sacw} = Q_{gacw} = P_{gacs} = P_{idw} = P_{ihom} = 0$$

δ_2 is defined as 1 for a grid box which has q_r and $q_s < 1$ x 10^{-4} kg/kg, and otherwise is defined as zero. δ_3 is defined as 1 for a grid box which has $q_r < 1$ x 10^{-4} kg/kg, and otherwise is defined as zero. D_{gaci}, D_{gacr} and D_{gacs} (W_{gaci}, W_{gacr} and W_{gacs}) are production rates for dry (wet) growth of hail. The above microphysical processes are defined in Tables A.1 and A.2.

Symbol	Meaning
P_{depit}	Depositional growth of cloud ice.
P_{int}	Initiation of cloud ice.
P_{imlt}	Melting of cloud ice to form cloud water.
P_{idw}	Depositional growth of cloud ice at the expense of cloud water.
P_{ihom}	Homogeneous freezing of cloud water to form cloud ice.
P_{iacr}	Accretion of rain by cloud ice; producing snow or hail depending on the amount of rain.
P_{raci}	Accretion of cloud ice by rain; producing snow or hail depending on the amount of rain.
P_{raut}	Autoconversion of cloud water to form rain.
P_{racw}	Accretion of cloud water by rain.
$P_{revp}(e_r)$	Evaporation of rain.
P_{racs}	Accretion of snow by rain; producing hail if rain or snow exceeds threshold and T $<$ 273.16 or rain if T $>$ 273.16.
$P(Q)_{sacw}$	Accretion of cloud water by snow; producing snow (P_{sacw}) if T $<$ 273.16 or rain (Q_{sacw}) if T $>$ 273.16.
P_{sacr}	Accretion of rain by snow; producing hail if rain or snow exceeds threshold; if now, produces snow.
P_{saci}	Accretion of cloud ice by snow.
P_{saut}	Autoconversion (aggregation) of cloud ice to form snow.
P_{sfw}	Bergeron process (deposition and riming) - transfer of cloud water to form snow.
P_{sfi}	Bergeron process embryos (cloud ice) used to calculate transfer rate of cloud water to snow (P_{sfw}).

Table A.1: Explanation of microphysical variables (part 1).

$P_{sdep}(d_s)$	Deposition growth of snow.
$P_{ssub}(S_s)$	Sublimation of snow.
$P_{smlt}(m_s)$	Melting of snow to from rain, T > 273.16.
P_{wacs}	Accretion of snow by cloud water to form rain, T > 273.16.
P_{gaut}	Autoconversion (aggregation) of snow to form graupel.
$P_{gfr}(f_g)$	Probabilistic freezing (Bigg) of rain to form hail.
$D(Q)_{gacw}$	Accretion of cloud water by hail.
$D(W)_{gaci}$	Accretion of cloud ice by hail.
$D(W)_{gacr}$	Accretion of rain by hail.
$P_{gsub}(s_h)$	Sublimation of hail.
$P_{gmlt}(m_h)$	Melting of hail to form rain, T > 273.16. (In this regime, Q_{gacw} is assumed to be shed as rain).
P_{gwet}	Wet growth of hail; may involve W_{gacs} and W_{gaci} and must include D_{gacw} or W_{gacr}, or both. The amount of W_{gacw} which is not able to freeze is shed to rain.

Table A.2: Explanation of microphysical variables (part 2).

Appendix B

PARAMETERIZATION OF SUBGRID-SCALE MIXING

The following equations are based on the equations found in Durran and Klemp (1983) and Clark and Peltier (1977). As stated in chapter 2, the subgrid-scale mixing is introduced into the basic velocity equations through the terms D_u, D_v and D_w

$$\begin{aligned} D_u =& \frac{\partial}{\partial x}\left(K_M\left(\frac{4}{3}\frac{\partial u}{\partial x}-\frac{2}{3}\frac{\partial v}{\partial y}-\frac{2}{3}\frac{\partial w}{\partial z}\right)\right) \\ &+\frac{\partial}{\partial y}\left(K_M\left(\frac{\partial u}{\partial y}+\frac{\partial v}{\partial x}\right)\right)+\frac{\partial}{\partial z}\left(K_M\left(\frac{\partial u}{\partial z}+\frac{\partial w}{\partial x}\right)\right) \end{aligned}$$

$$\begin{aligned} D_v =& \frac{\partial}{\partial y}\left(K_M\left(-\frac{2}{3}\frac{\partial u}{\partial x}+\frac{4}{3}\frac{\partial v}{\partial y}-\frac{2}{3}\frac{\partial w}{\partial z}\right)\right) \\ &+\frac{\partial}{\partial x}\left(K_M\left(\frac{\partial u}{\partial y}+\frac{\partial v}{\partial x}\right)\right)+\frac{\partial}{\partial z}\left(K_M\left(\frac{\partial v}{\partial z}+\frac{\partial w}{\partial y}\right)\right) \end{aligned}$$

$$\begin{aligned} D_w =& \frac{\partial}{\partial z}\left(K_M\left(-\frac{2}{3}\frac{\partial u}{\partial x}-\frac{2}{3}\frac{\partial v}{\partial y}+\frac{4}{3}\frac{\partial w}{\partial z}\right)\right) \\ &+\frac{\partial}{\partial x}\left(K_M\left(\frac{\partial u}{\partial z}+\frac{\partial w}{\partial x}\right)\right)+\frac{\partial}{\partial y}\left(K_M\left(\frac{\partial v}{\partial z}+\frac{\partial w}{\partial y}\right)\right) \end{aligned}$$

where

$$K_M = k^2\Delta x\Delta z|Def| \times [\max(1-\frac{K_H}{K_M}\mathrm{Ri},0)]^{1/2},$$

$$\mathrm{Ri} = \begin{cases} \frac{N^2}{(Def)^2}, \text{ for } q_v < q_{vs} \\ \frac{N_m^2}{(Def)^2}, \text{ for } q_v = q_{vs} \end{cases}$$

$$\begin{aligned} (Def)^2 = \frac{1}{2}\Bigg[&\left(\frac{4}{3}\frac{\partial u}{\partial x}-\frac{2}{3}\frac{\partial v}{\partial y}-\frac{2}{3}\frac{\partial w}{\partial z}\right)^2+\left(-\frac{2}{3}\frac{\partial u}{\partial x}+\frac{4}{3}\frac{\partial v}{\partial y}-\frac{2}{3}\frac{\partial w}{\partial z}\right)^2+\left(-\frac{2}{3}\frac{\partial u}{\partial x}-\frac{2}{3}\frac{\partial v}{\partial y}+\frac{4}{3}\frac{\partial w}{\partial z}\right)^2\Bigg] \\ &+\left(\frac{\partial u}{\partial y}+\frac{\partial v}{\partial x}\right)^2+\left(\frac{\partial u}{\partial z}+\frac{\partial w}{\partial x}\right)^2+\left(\frac{\partial v}{\partial z}+\frac{\partial w}{\partial y}\right)^2 \end{aligned}$$

Here Ri is the Richardson number, and

$$N_m^2 = g(1 + \frac{Lq_{vs}}{RT})(1 + \frac{\epsilon L^2 q_{vs}}{c_p R T^2})^{-1}(\frac{d \ln \Theta}{dz} + \frac{L}{c_p T}\frac{dq_{vs}}{dz}) - g(\frac{d(q_v + q_c)}{dz}),$$

and $\epsilon = 0.622$. The expression for the moist buoyancy frequency N_m has been shown to be a satisfactory approximation to the exact expression. The subgrid scale mixing terms in the scalar equations are of the form

$$D_\chi = \frac{\partial}{\partial x}\left(K_H \frac{\partial \chi}{\partial x}\right) + \frac{\partial}{\partial y}\left(K_H \frac{\partial \chi}{\partial y}\right) + \frac{\partial}{\partial z}\left(K_H \frac{\partial \chi}{\partial z}\right)$$

where χ = potential temperature, the water category mixing ratios, and the tracer mixing ratios. In the model $k = 0.21$ and $K_H/K_M = 1$. This ratio of K_H/K_M allows turbulent mixing to begin when Ri drops below 1.

VITA

Gretchen Mullendore grew up in the farmlands of northeastern Ohio and had the good fortune of experiencing many thunderstorms in the woods of her childhood home. But after seventeen years in small town America, she was ready for the big city and went off to Pasadena, California for college. After one year of college, Ms. Mullendore and the Caltech administration agreed she needed a "break", so Gretchen went to work at a local porfolio management company as a network administrator. Three years of office politics encouraged Gretchen to give up the big salary and go back to school. Seeking adventure, Gretchen ventured behind the "Orange Curtain" and discovered where the rich and beautiful (and Republican) live while attending Orange Coast Community College in Costa Mesa, California. After to learning to row sweep and learning a bit about earthquakes, Gretchen transferred up north to continue earthquake work at the University of California, Santa Barbara. Gretchen received her degree in Geophysics from UCSB in 1998. Deciding that the she was too impatient to wait around for the earth to move, Gretchen went back to studying storms, starting work on her Ph.D. in Atmospheric Sciences at the University of Washington in summer 1998.